Hydraulic Compliance Control of the Quadruped Robot HyQ

Thiago Boaventura Cunha

University of Genoa, Italy
and
Istituto Italiano di Tecnologia (IIT)

A thesis submitted for the degree of

Doctor of Philosophy (Ph.D.)

March, 2013

Thesis Supervisors:

Dr. Jonas Buchli

Professor

Agile & Dexterous Robotics Lab

Swiss Federal Institute of Technology Zurich (ETH Zurich)

Dr. Claudio Semini

HyQ Group Leader

Department of Advanced Robotics

Istituto Italiano di Tecnologia (IIT)

Dr. Darwin G. Caldwell

Director

Department of Advanced Robotics

Istituto Italiano di Tecnologia (IIT)

Abstract

A legged robot is forced to deal with environmental contacts every time it takes a step. To properly handle these interactions, it is desirable to be able to set the foot compliance, that is, the relation between the motion and forces generated at the contact point.

The compliance of a robotic system can be passively or actively achieved. A passively-compliant robot makes use of physical components such as springs and dampers to obtain a desired dynamical behavior for the robot. On the other hand, an actively-compliant robot is able to reach programmable impedance characteristics through software, with no need of additional compliant components. Therefore, for the price of extra energy consumption, active compliance is able to considerably increase the robot's versatility.

HyQ is a quadruped robotic platform built for performing both precise and slow motions as well as highly-dynamic maneuvers. To obtain this flexibility in accomplishing such different tasks, HyQ is provided with suitable mechanical properties, and adequate controllers.

This thesis demonstrates that the hydraulic actuation employed in HyQ is able to provide both robustness to high impact forces as well as the power requirements in terms of velocity, torque, and bandwidth. These characteristics are essential for properly controlling the robot compliance.

Based on the understanding of the hydraulic force dynamics, a high-performance model-based torque controller is presented as the basis for implementing a reliable compliance controller. This thesis presents the design and implementation of several force and compliance controllers that are currently being used in the HyQ robot.

A discussion about the influence of physical characteristics of the load in the system performance, such as inertia and friction, provides a good insight about the limitations and advantages of different actuation systems when performing force control. It is shown, through a new force modeling framework, that the load characteristics can strongly affect the closed-loop force dynamics. These discussions can also assist robot designers to improve the force and compliance capabilities of their robots.

This work also discusses the important topic regarding the stability of an actively-compliant robot while contacting passive terrains. In this case, to ensure stability, the actively-compliant leg must also behave passively. It is shown that many aspects influence the leg passivity, such as sampling frequency, filtering, and also the torque closed-loop bandwidth.

An experimental comparison between active and passive compliance serves as the basis to identify advantages and drawbacks of both approaches. Furthermore, experiments with the HyQ robot demonstrate that with a high-performance torque controller it is possible to successfully employ active compliance for performing highly-dynamic tasks, such as hopping, trotting, and jumping.

Aos meus pais, pelo grande exemplo que são.

E em especial à minha mãe, a qual me ensinou que não é só a educação
que muda o mundo, mas também a nossa vontade de passar essa
educação adiante.

Acknowledgements

Firstly, I would like to express my gratitude and appreciation to my parents. Their unwavering support and guidance throughout my life has enabled me to be here, finishing a Ph.D. course in robotics.

I would like to take this opportunity to sincerely thank my supervisors Prof. Jonas Buchli and Dr. Claudio Semini for all the support, time, patience, teaching, and friendliness during the whole period that we shared together. I appreciate a lot all their effort and contribution for making me capable to defend this Ph.D. thesis.

I would like to express my gratitude also to Prof. Darwin G. Caldwell for all the support from the Advanced Robotics Department and for believing in the potential of the HyQ project and team. I would like to thank a lot also Dr. Emanuele Guglielmino for having given me the opportunity to do my master thesis at IIT in 2009.

I would like to specially thank my Ph.D. colleagues Marco Frigerio, Michele Focchi, Shuang Peng, and Hamza Khan. Marco, thank you for all the patience in teaching me geek software stuff and for the many hours spent together in debugging and fixing compilation errors. Michele, thank you for the help with my various doubts in control and electric issues and all the great discussion we had. Shuang, thank you for the valuable discussions on hydraulics and for your laughs that used to cheer up the entire HyQ work group. Hamza, a special thank *just for you*!

I would like to express also my thanks to my other friends of the HyQ group. Dear Jake Goldshmith, thank you for your friendship, pleasant company, and help with mechanical issues. Ioannis Havoutis, Stephane Bazeille, and Jesus Ortiz thanks for the nice conversations and advices.

Contents

CONTENTS

List of Figures

List of Tables

Glossary

Δv General representation for linearized variables

V General representation for constants (uppercase letter)

v General representation for variables (lowercase letter)

CoG   Center of gravity

HyL   *Hy*draulic *L*eg test bench

HyQ   *Hy*draulic *Q*uadruped robot

$\boldsymbol{V}$ General representation for matrices (uppercase bold letter)

$\boldsymbol{v}$ General representation for vectors (lowercase bold letter)

CoP   Center of pressure

DOF   Degree of freedom

HAA   Hip abduction/adduction joint

HAA   Knee flexion/extension joint

HFE   Hip flexion/extension joint

PD   Proportional-derivative controller

PI   Proportional-integral controller

PID   Proportional-integral-derivative controller

MIMO   Multiple-input-multiple-output

SISO   Single-input-single-output

ZMP   Zero moment point

Chapter 1

Introduction

This thesis shows how to make a robot versatile, robust, and safe through the control of its compliance, which can be defined as the relation between the motion and the forces created by the robot at the contact points. All the requirements, structure, limitations and advantages behind the high-performance compliance control of the *Hy*draulic *Q*uadruped robot *HyQ* are presented in here in a simple and logic manner.

The first and most important step to control HyQ's compliance is the development of high-performance force control at the robot joints. This controller permits to explicitly adjust both the interaction forces generated at the robot's end-effector as well as the torques applied to its joints. Furthermore, the implementation of this precise force controller gives HyQ the attractive possibility to consider its joints as high-fidelity torque sources. This abstraction is very convenient to implement many other high-level controllers. Also, since many robots can well be modeled as multi-rigid-body-systems, their dynamics have naturally torques as inputs. Therefore, the implementation of tasks such as trots, jumps, including robot balance, and orientation become much more intuitive and easy with a low-level torque control loop.

The development of an inner torque control loop permitted to straightforwardly implement the main goal of this work, which consists in the design of HyQ's compliance controller. This controller aims to calculate the torques needed for behaving according to a desired dynamic behavior. This behavior is defined by a certain impedance setting, which can be described in either joint or task space.

The main motivations for the development of such controllers are given in the next section. Then, the HyQ robotic platform is presented. Next, a description of the main advantages that hydraulic actuators can bring to highly-dynamic robotic applications are given. This chapter finishes with a list of the main contributions of this work and an overview of the thesis organization.

1.1   Motivation

More and more robots have to interact with the environment around them, with humans, tools or other objects. Physical contacts are inherent to robotics applications such as assembly, service duties, and legged locomotion. To properly handle these physical contacts, it is essential to be able to control the interaction forces, or more generically speaking, to control the robot's compliance.

The control of the robot's compliance permits to obtain a vast range of desired dynamic behaviors. It can involve the use of virtual components, such as springs and dampers, that are virtually "attached" to the robot structure. These virtual components can have complex characteristics (e.g. nonlinear stiffness and damping) and can be situated anywhere in the robot, no matter how difficult it would be to physically realize and place them, which is a great advantage over a passively-compliant robot.

Another benefit of actively controlling the compliance is that it enables to change the component's characteristics, such as stiffness and damping, on-the-fly while performing a certain task. For instance, theories about leg stiffness variations for terrains with different surface properties and also about reasons for gait selection in running quadrupeds can be experimentally validated with a robot that can control its leg compliance.

A proper choice in the structure of the compliance controller brings out additional benefits to the robot overall control. In case a nested torque controller is present in the compliance control architecture, as depicted in Fig. 1.1, it is possible to exploit advanced model-based controllers to improve the robot performance. For instance, a rigid body inverse dynamics feed forward control permits to keep a compliant behavior without having to give up on the tracking of position trajectories. This
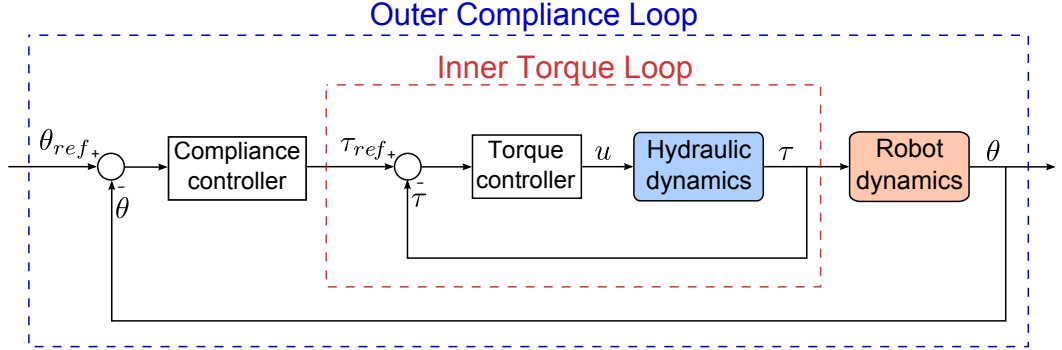
Figure 1.1: Control architecture used for the HyQ compliance controller. An outer loop controls the robot compliance by feeding back the robot joint positions, and then generates the torques required for behaving according to desired stiffness and damping characteristics. These reference torques are sent to an inner torque loop, which feeds back the torque at the robot joints to track the reference torques as precisely as possible. The torque controller output u corresponds to an analog signal that commands the HyQ hydraulic actuators. The actuators produce the torques τ that are applied to the robot joints to finally obtain the compliance characteristics set by the user.

feature is not only desirable but mandatory for legged robots that aim to walk on rough terrain.

All these points suggest that controlling the compliance is crucial for a legged robot. Compliance control is indeed a *must* for those robots that aim to be versatile, safe, and truly useful for humankind. The investigation of the compliance control is a necessary and essential step towards the robotics evolution.

1.2 HyQ Hardware Overview

HyQ, shown in Fig. 1.2a, is a fully torque-controlled robot designed and built at the Advanced Robotics Department of the Istituto Italiano di Tecnolgia. It is a quadruped robot designed for research in the field of highly-dynamic locomotion (e.g. jumping and running) and rough terrain walking [Semini, 2010].

Each of HyQ's legs has three active degrees of freedom (DOF): the hip abduction/adduction (HAA) joint, the hip flexion/extension (HFE) joint, and the knee flexion/extension joint (KFE), as depicted in Fig. 1.2b.

The HFE and KFE joints are actuated by high-speed servovalves connected to hydraulic asymmetric cylinders. These joints provide high speed and torque for

(a) HyQ robot   (b) HyQ joint names
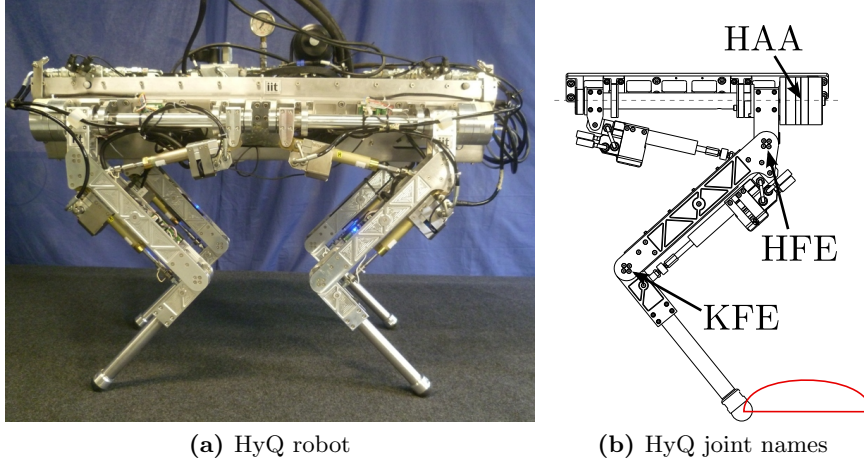
Figure 1.2: (a) HyQ: a hydraulically-actuated quadruped robot. The HyQ leg drawing in (b) defines the joint names: the hip abduction/adduction (HAA), the hip flexion/extension (HFE), and the knee flexion/extension (KFE). The red line depicts a half-ellipse foot trajectory that is used for the HyQ trotting.

motions in the robot sagittal plane. More details about the hydraulic components and characteristics are given in Chapter 3.

The HAA joints, on the other hand, are driven by high-torque DC brushless electric motors in combination with a harmonic gear with reduction ratio of 1 : 100. Electric actuation was chosen for these joints because the impact forces and required speed in the coronal plane of the robot are not as high as in the sagittal plane. Also, the use of electric motors instead of hydraulic actuators help to make the robot more energy efficient. However, recent experiments with fast lateral motions have shown that this actuation type is neither robust nor fast enough for HyQ. Thus, new hydraulic rotary actuators are being tested to replace them.

Presently, HyQ can be powered in two different modalities:

- *Off-board pump*: in this modality, the reservoir, pump, and the electric motor that drives the pump are located outside of the robot. The pressurized oil is transmitted to the robot through long hoses. The total power available is about 11 kW. This modality is used for more dynamic motions, such as jumps, where it is convenient to have the robot lighter.

- *On-board pump*: in this modality, the whole hydraulic power unit (reservoir, pump, and electric motor) is located inside the robot. The maximum power

of the system is 8.7 kW, being able to supply up to 26 L/min at 200 bar. The robot, however, is still tethered to an external electric cable for powering the on-board pump. For making the system more efficient, a variable displacement pump was used (see Section 3.2).

(a) Off-board pump, by Hydrapac   **(b)** On-board pump
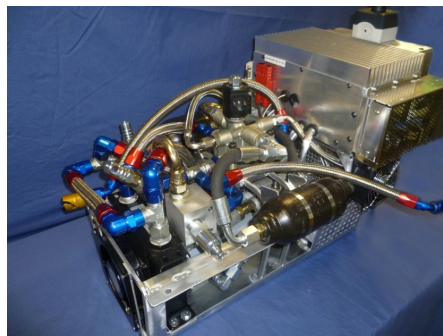
Figure 1.3: HyQ pump modalities: (a) a mobile off-board pump is employed when the robot needs to be lighter to perform more dynamical maneuvers; and (b) an on-board pump unit, which weighs in total almost 40 kg, is able to provide up to 8.7 kW of hydraulic power to the robot.

An alternative in the use of the *on-board* pump modality is the employment of batteries. The use of batteries will increase the robot's mobility since in this scenario the robot will be completely free to move and will not be tethered to anything. This topic is in the *Future Work* list in Section 8.1.

A third modality, where the on-board pump will be driven by a combustion engine, is also an important part in the HyQ *Future Work*. In this case, although internal combustion engines have a low energy efficiency, the much higher energy density of fossil fuels would increase significantly the robot autonomy. For more details regarding the pump efficiency and types, see Section 3.2.

The torso and legs of HyQ are constructed from an aerospace-grade aluminum alloy. In this version of the robot, no springs are present anywhere on the robot. Table 1.1 summarizes the most important characteristics of the HyQ robot platform. A more detailed presentation of the robot design and components is found in [Semini et al., 2011b] and [Semini, 2010]. Aspects related to the control of HyQ's legs are further discussed in detail in Chapter 5 and Chapter 6.

Table 1.1: Main hardware characteristics of the HyQ robot

Property	Value
Dimensions	1.0m x 0.5m x 0.98m (LxWxH)
Weight (off-board pump)	75kg
Weight (on-board pump)	100kg
Active DOF	12
Joint range of motion	120° (for each joint)
Hydraulic actuation	servovalves + asymmetric cylinders
Electric actuation	DC brushless motors + harmonic gear
Max. torque [electric]	140Nm (after gear reduction)
Max. torque [hydraulic]	145Nm (peak torque at 16MPa)
Position sensing	absolute and relative encoders at joints
Force sensing	load cell at the cylinder rod
Body orientation sensing	inertial measurement unit (IMU)
On-board computing unit	PC104 stack with Pentium CPU board

1.2.1   HyL: the one-leg setup

The HyQ robot is a very complex platform, with many DOFs. To implement and test the controllers presented in this thesis in an easy way, a one-leg setup, named HyL (*Hy*draulic *L*eg), was used. The use of HyL permitted to investigate the controller properties in a simpler setup before implementing them in the whole HyQ robot. The transition of the code developed for HyL to HyQ is straightforward since both systems use the same simulation and real time control software (called SL [Schaal, 2006]).

In HyL, one leg that is identical to the ones used in HyQ is fixed to a vertical slider. This constrained the leg to move only in the vertical direction. Therefore, the balance of the leg is not an issue, and the focus can be put into the force, position, and compliance control of the leg joints. The HAA joint is not used in this setup and its relative DOF is mechanically blocked. HyL uses then only two of the three leg joints: the *HFE* and *KFE*.

The setup is also equipped with a pulley and encoder system that is able to measure the leg position on the slider. In addition, a force plate can be used to

measure the ground reaction forces created by the leg.

1.3 Hydraulics & Robotics

Hydraulics has many properties that make it an ideal choice for highly-dynamic articulated robot applications. Firstly, even though electric drives had a great development in the last decades, hydraulic drives still have higher power-to-weight ratio than electric ones [Hollerbach et al., 1992; Seok et al., 2012]. They are also stiffer, resulting in the possibility to have higher closed-loop gains, greater accuracy, and better frequency response [Clark, 1969].

Furthermore, hydraulic actuators are mechanically very simple and allow for robust design against impacts and overload. This is very important in dynamic applications where high peak forces on the robot structure can not only not be avoided but are even part of the requirements. On the other hand, electric motors usually operate at high velocities, and to be able to provide high power levels also at low velocities they often make use of gearboxes with high reduction ratios. These gearboxes are often not robust against high impacts forces and also introduce nonlinear friction, making this kind of arrangement in most of the times not very suitable for highly-dynamic robots.

Hydraulics can use a variety of different fluids other than oil depending on the application requirements (e.g. water). In addition, the hydraulic fluid can serve also as lubricant and coolant of the actuators.

As further shown, hydraulic actuation also guarantees high enough actuator bandwidth to achieve very satisfactory torque control in the spectrum of interest for dynamic locomotion of medium to large scale robots (i.e. a few kg and heavier). This high-performance hydraulic torque control is the basis for implementing an effective compliant behavior through a naturally very stiff actuation system.

Hydraulic actuators have the misleading reputation of being dirty, messy, and thus unsuitable for robotics [Hurst, 2011; Robinson and Pratt, 2000]. This is, in part, a myth. And HyQ is a very good example that hydraulics can be very clean.

Hydraulics uses a fluid, usually oil, to transmit power to the actuators. All the components in a hydraulic circuit, such as valves, hoses, and cylinders have oil flowing inside them. Thus, during installation and maintenance, since the hydraulic

circuit is open, a small amount of oil leaks out. However, luckily these procedures are not performed often. During normal operation, if the hydraulic connectors are correctly assembled no external leakage is present. In the HyQ robot, apart from exceptional maintenances, not a single drop of oil has leaked. In addition, HyQ uses quick release couplings that permit to open part of the hydraulic circuits easily and with no leak. As a result, both HyQ and its laboratory are very clean.

1.4 Contributions

The main contributions of this thesis for the robotics research community as well as for the progress of the HyQ project are listed in this section:

- **Development of the low-level torque control, which is the basis for implementing several high-level controllers:** the implementation of high-level controllers which deal, for instance, with the robot's balance, locomotion, and vision rely on the application of torques at the robot joints. The first and essential step of this thesis consisted in the development of a high-performance model-based torque controller. The creation of a *torque-controlled* robot widely opened the range of possibilities for other people to collaborate to the HyQ project.

- **Influence of torque bandwidth on the Z-width:** the Z-width is a well-known concept, especially in the field of haptics. It determines what is the range of virtual impedances and damping that can be passively rendered. Many aspects influence the Z-width, such as sampling time, controller frequency, and filtering. However, in a compliance controller that uses a cascade control approach, as depicted in Fig. 1.1, the influence of the inner torque controller in the Z-width has not been discussed in the literature. Therefore, this thesis contributes to the state of the art by demonstrating that the closed-loop bandwidth of the inner torque controller can significantly influence the Z-width of a robotic manipulator.

- **Definition of a procedure for designing a compliance controller:** based on the stability and passivity analyses, a procedure for designing a compliance controller was defined. It uses the concept of Z-width to establish a

trade-off between performance and stability which helps to design the inner torque loop in a cascade compliance controller.

- *Summary of important theoretical and practical aspects on hydraulic control applied to robotics:* this work provides all the details learned with more than four years of experience with the hydraulic actuation of the HyQ robot. It shows that with a proper choice of components, the control of hydraulic actuators is very simple and easy to tune. A hydraulic model is presented in a simple manner, where an alternative parametrization circumvents problems related to the lack of information on the datasheet of components such as servovalves.

- *Generalization of a velocity feedback framework:* the well-known concept of the natural feedback of the load velocity into the hydraulic force dynamics is generalized. A general 1-DOF framework, using basic physical principles, shows that there exists an intrinsic velocity feedback in the generalized force dynamics, independently of the actuation technology. This is a new and very useful contribution that permits to improve the force/torque control capabilities of many robots. This phenomena is illustrated using three different actuation systems. This analogy helps also to clarify important common aspects regarding torque/force control.

- *Experimental comparison between passive and active compliance:* the performance of the HyQ actively-compliant leg, which uses virtual springs and dampers, is confronted with an identical but passively-compliant version of the leg, where a real spring was attached to it. This experimental comparison between two identical systems using different compliance approaches is a new and interesting contribution to the research community to assess the limits and benefits of each compliance approach.

1.5 Thesis outline

The thesis is organized in logical and sequential chapters as follows:

1. INTRODUCTION

- Chapter 2 first introduces the state of the art in legged robots, summarizing the main developments seen in this field in the last decades and how the new generation of legged robots are controlled. Then, the main works in force, torque, and compliance control are presented as well as the main advancements in these areas.

- Chapter 3 outlines the most relevant aspects of hydraulics in robotics, such as fluid properties, hydraulic circuit components, and nonlinear and linear modeling.

- Chapter 4 presents a new framework for the load velocity feedback phenomena in the force control dynamics. It consists of the definition of physical concepts such as transmission stiffness which permit to rewrite the traditional actuator force model in a more intuitive form for force control. The main aspects behind this physical phenomena are presented for the two actuator types of HyQ: hydraulic and electric.

- Chapter 5 uses the concepts presented in the previous chapters for designing model-based force controllers for the hydraulic actuators used in HyQ. It is an essential chapter for understanding the overall high-performance low-level control used in HyQ. This chapter also breaks out the paradigm that hydraulic actuators are difficult to control. Three different control approaches, in an increasing level of complexity, are proposed: a simple feedback PID controller; a feedback PID controller together with a feed forward command for compensating for the velocity feedback phenomena; and a nonlinear input-output feedback linearization controller.

- Chapter 6 is, together with Chapter 5, the core of the thesis. It consists in the design of a set of different controllers that are able to adjust the robot compliance. Some of them control the compliance at joint level, such as the feedback PD controller with a feed forward command from the rigid body inverse dynamics, and others at the task space, such as virtual model control and impedance control. To ensure the stability of such controllers under contact situations with the environment, the passivity of the compliance controller and its nested force loop is also investigated.

- Chapter 7 summarizes results and relevant discussions. It shows some applications, results, and capabilities of the compliance control of the HyQ robot. Some important topics that can influence the performance of the force control, such as link inertia and friction, are discussed. The importance of the closed-loop torque bandwidth in the performance of the compliance control is also presented.

- Chapter 8 addresses the main conclusion of this thesis. It also suggests a list with some of the further works to be carried out.

1. INTRODUCTION

Chapter 2

Related work

The body of research in compliance control and related areas is very vast. Since it is not possible to give exhaustive reference to all the work done, at least some of the most important contributions and concepts related to this thesis are discussed.

Firstly, part of the extensive research in legged robotics is presented. This review is adapted from Boaventura et al. [2012b]. Next, a short review about force and torque control is shown. Some of the difficulties found by the pioneers in force control in the 50's are discussed, as well as how their successors managed to improve the poor performance and stability issues that prevented for many years the implementation of compliance controllers in highly-dynamic applications.

2.1 Legged robots

An important line of research in dynamic legged locomotion was initiated in the 1980's by Raibert and collaborators [Raibert, 1986]. They showed impressive dynamic gaits and maneuvers on one (Fig. 2.1a), two and four-legged robots. However, due to a relatively small workspace of the prismatic legs and the absence of terrain sensing, the versatility of these machines was limited.

Raibert's research recently culminated in the presentation of *BigDog* [Raibert et al., 2008] and *PETMAN* [BostonDynamics, 2011]. While *BigDog*, Fig. 2.2a, is clearly a very impressive machine and raises the bar of what is achievable, a lot of research questions remain unanswered. Details of neither the design of *BigDog*, nor its control aspects are available to the research community at large.

(a) Raibert's one-leg hopper

(b) Asimo, by Honda

(c) Petman, by Boston Dynamics
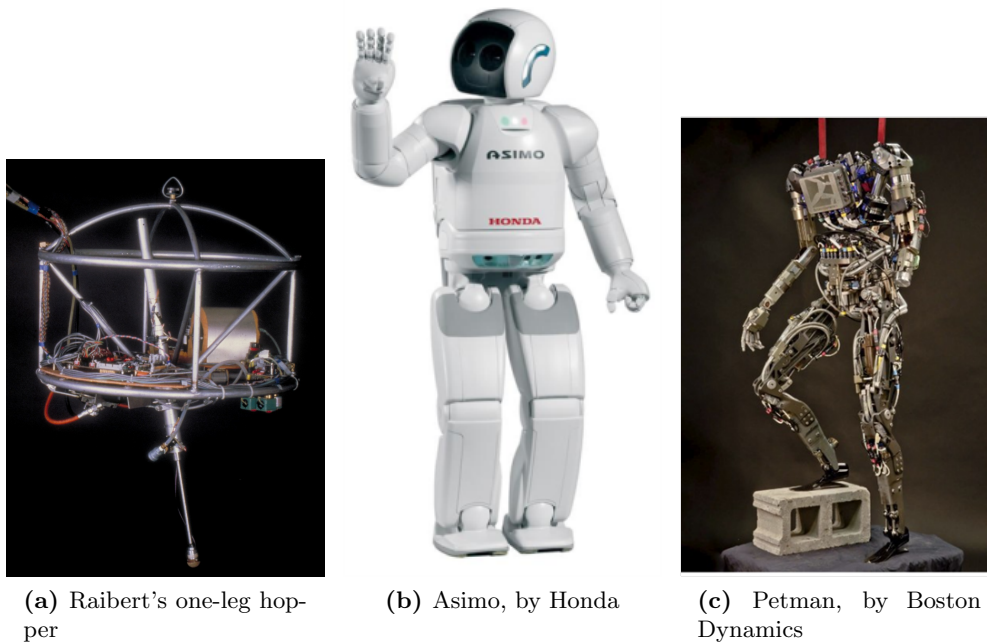
Figure 2.1: One and two legged robots from different generations.

(a) BigDog

(b) LittleDog
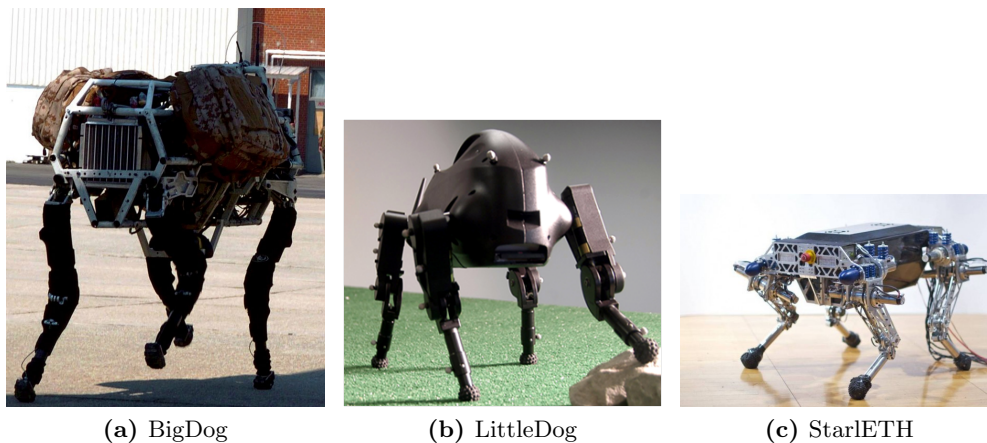
(c) StarlETH

Figure 2.2: Some of the most developed quadruped robots built so far. In (a) and littledog.png, some of the Boston Dynamics' most succesful robots; in (c) the StarlETH robot, developed at ETH.

The control of today's legged robots falls largely into two categories: (a) support polygon based, statically, or quasi-statically stable walking, where the CoG or CoP is kept in the support polygon at all times (e.g. ZMP [Vukobratovic and Borovac, 2004]); (b) limit cycle walking, where the gait is not stable at any given moment, but shows a cyclic stability [McGeer, 1990; Westervelt et al., 2007].

The ZMP criterion is a sufficient but not necessary stability criterion for legged locomotion. It leads to overly conservative and quasi-static locomotion, using kinematic plans that are then typically tracked with high-gain position control and therefore require detailed terrain knowledge. ZMP walking is mostly demonstrated on flat or quasi flat ground, for instance with the indoor environment biped robot ASIMO by Honda [Hirai et al., 1998], and does not easily generalize to non-flat conditions [Sentis et al., 2010]. A compliance controller, as the one presented in this thesis, permits to easily implement more sophisticated and robust locomotion approaches.

Recently, locomotion through challenging terrain was the focus of the *Learning Locomotion* project [Kalakrishnan et al., 2011]. The aim of this project was on control and planning aspects. The platform *LittleDog* (Fig. 2.2b), however, was a high-geared robot built mainly for static locomotion and therefore suggestions for control of dynamic locomotion could not easily be validated.

Inspired by Raibert's work of the 1980's, several other quadruped robots were constructed and successfully demonstrated dynamic locomotion with limit cycle stability. For example, *Scout II* [Poulakakis et al., 2005] and *Rush* [Zhang and Kimura, 2009] performed bounding, *KOLT* [Estremera and Waldron, 2008] and a modified version of *Scout II* [Hawker and Buehler, 2000] showed trotting. *Airhopper* [Tanaka and Hirose, 2008] achieved an explosive vertical jump out of a squat posture. *StarlETH* showed several low-dynamic locomotion capabilities such as trotting, walking, and steam walking [Hutter et al., 2012].

While most machines employ either limit cycle walking/running or support-polygon based control (e.g. ZMP), a versatile machine should be able to cover the whole spectrum from completely static locomotion (such as climbing and walking on ice) to highly dynamic locomotion (such as trotting and bounding). In addition, it should be able to exert explosive jumps to move through terrain with high obstacles, steps or ditches. To the best of the author's knowledge, no versatile quadruped

machine other than *BigDog* has yet demonstrated such a wide range of statically and dynamically stable locomotion.

2.2   Torque control

Since the very early days of the development of articulated robots, torque control was of fundamental interest [Whitney, 1987, 1985]. Being able to apply precise joint torques to a given robot structure has many advantages.

Torque control allows various forms of impedance control, control of contact forces, rigid body dynamics model-based control, and many other forms of model-based control which have torques as control output. Next, some of these widespread torque-based control methods are described.

The work presented by [Hogan, 1985b,c] is considered the foundation of *impedance control* for articulated manipulators. It highlights that two physical systems *must* physically complement each other during dynamic interactions. That is, along any degree of freedom, if one system is an impedance, the other must be an admittance and vice versa. Thus, to ensure physical compatibility with the environment, which is generally considered an admittance, the manipulator should assume the behavior of an impedance. Essentially, the impedance control framework specifies the force produced, usually at Cartesian space, in response to a motion imposed by the environment. To produce the desired mass-damper-spring dynamic behavior, the impedance controller generates torques to be applied to the joints.

There are several other forms of controlling the manipulator compliance. For instance, [Kazerooni et al., 1986a,b] presents a method for designing compliance controllers of constrained manipulators in the presence of bounded model uncertainties. The authors show that, in general, the closed-loop impedance of a system cannot be shaped arbitrarily over an arbitrarily wide frequency range. The multivariable Nyquist criteria is used to examine trade-offs in stability and robustness against tracking of desired target impedances over bounded frequency ranges. In [Albu-Schäffer and Hirzinger, 2002] a new controller structure, which consists of an impedance controller enhanced by local stiffness control, is proposed. This structure computes the control effort using two different loops: a slower Cartesian loop and a

faster joint loop. The proposed controller presented a better performance than classical impedance and stiffness control, but lower geometric accuracy when compared to admittance control.

In [Khatib, 1987], the concept of *operational space control* is presented. The author proposes a control approach shifting the focus of control from the single joints of the robot to the actual *task*, typically at the end–effectors. In this framework, the control of both the position and the contact forces at the end–effector also relies on the manipulation of the joint torques.

More recently, the very intuitive *virtual model control* [Pratt et al., 2001] was presented for legged locomotion. In this framework, virtual components that have physical counterparts, such as mechanical springs and dampers, are placed at convenient locations within the robot or between the robot and the environment. Once the placement is done, the interactions between these components and the robot is defined by the respective Jacobian matrix, which generates the desired torques or forces at the actuators.

Other controllers use the robot's rigid body model to control the robot compliance. A possible solution to improve the robustness of legged locomotion is presented in [Buchli et al., 2009] through the use of a model-based rigid body inverse dynamics control. This control permits to reduce the position feedback gains with no significant losses in tracking performance. These lower position gains make the robot more compliant and consequently more robust in unknown and possibly rough terrains. To overcome the intrinsic complexity related to floating-base robots such as under-actuation, dynamically changing contact states, and contact forces that may not be known, an orthogonal decomposition is proposed in [Mistry et al., 2010] to calculate the floating base rigid body inverse dynamics.

Force feedback and force control becomes mandatory to achieve a robust and versatile behavior of a robotic system in poorly structured environments as well as safe and dependable operation in the presence of humans [Villani and De Schutter, 2008]. Furthermore, torque control also allows the development of versatile articulated robots that can be used in a wide variety of applications, e.g. disaster recovery, construction, service robots, etc [Boaventura et al., 2012b].

Research on robot torque/force control began in the 1950's with remote manipulators, but stability issues emerged immediately [Whitney, 1985]. For position-

controlled systems, stiff mechanical interfaces between the actuator and its load raise the system bandwidth without compromising stability [Cannon and Schmitz, 1984]. For force-controlled systems, however, this stiff transmission is the main reason for stability problems. Also time delays, caused by actuator bandwidth limitation and numerical computations, had a strong influence in the closed-loop system stability [Whitney, 1985].

A way to overcome such issues has been found in reducing the transmission stiffness, and consequently the overall system bandwidth. Initially, it was done by using flexible sensors, and more recently by introducing springs in series with the actuator [Pratt and Williamson, 1995]. Besides reducing the transmission stiffness and making the force dynamics less reactive, the spring in series elastic actuators (SEAs) has also four other important functions: (a) to protect the actuator (or gearbox) from damage due to impact forces, (b) to store energy, (c) to be backdrivable and possibly safer during human-robot interaction, for instance, and (d) to measure the load force through the spring deflection.

The design of SEAs requires a trade-off between robustness and task performance. To choose the most appropriate spring stiffness is not a trivial task and it can seriously limit the robot versatility. In order to avoid this trade-off, several variable stiffness actuators (VSAs) have been recently proposed. In [Grebenstein et al., 2011], two variable stiffness mechanisms are applied to the DLR arm system: in the called 'floating spring joints' a small motor changes the stiffness, while for the forearm and wrist actuation nonlinear elastic elements are used in a bidirectional antagonistic manner to vary the joint stiffness. A new variable stiffness actuator (CompAct-VSA) is presented in [Tsagarakis et al., 2011]. The principle of operation of CompAct-VSA is based on a lever arm mechanism with a continuously regulated pivot point. The proposed concept allows for the development of an actuation unit with a wide range of stiffness and a fast stiffness regulation response. A more complete review about compliant actuator designs can be found in [Ham et al., 2009].

Although VSA is a promising solution for compliant robots, aspects such as weight, volume, mechanical complexity, robustness, and velocity saturation still limit its use in highly-dynamic robots. Furthermore, since low joint stiffness reduces the robot controllability and also position tracking capabilities, commonly VSAs operate

in a high stiffness configuration. In these cases, the safety hallmark of passive compliance is essentially lost.

However, adding compliance in the hardware also introduces some drawbacks. A compliant element in series with the structure reduces the overall controllability and achievable bandwidth [Hurst et al., 2004]. These two aspects can also have severe implications on safety. On the other hand, advanced control approaches, such as model-based control, can be successfully applied in the low-level force control to reach a good tracking performance without having to give up on the closed-loop bandwidth. Since the force is always transmitted from the actuator to the load through a transmission with finite stiffness (e.g. gearbox, hydraulic oil, spring), there exist an intrinsic physical phenomena, where the load velocity is fed back into the force dynamics, which does not depend on the actuator. An important model-based control consists in compensating for this physical load velocity feedback [Boaventura et al., 2012a].

The load velocity dynamics introduces a zero in the valve input-to-force transfer function. This zero depends on the load damping and can seriously limit the achievable closed-loop torque bandwidth. The position of these zeros cannot be changed by feedback control techniques, and [Alleyne et al., 1998] says that more advanced control algorithms are a *necessity, not just a luxury.*

The load velocity compensation was initially discussed for hydraulic actuators in [Conrad and Jensen, 1987], where it is shown that closed-loop control with force feedback is ineffective without velocity feedforward, or full state feedback. The influence of the load motion is shown for a hydraulic actuator in [Dyke et al., 1995], which focused in the structural control for civil engineering against environmental loads such as strong earthquakes and high winds. The authors called this concept *natural velocity feedback.* [Dimig et al., 1999] proposed a possible solution to negate the natural velocity feedback through the creation of an additional feedback loop, and applied it to seismic simulations for structural testing. Zhao [Zhao, 2003] extended the velocity feedback compensation to consider servo-system nonlinearities. The proposed nonlinear velocity feedback compensation scheme permitted to apply dynamic forces to a mass-spring-dashpot structural system at all frequencies of interest.

2. RELATED WORK

Previous works addressed the compensation of the load motion for electrical drives as well. Hori et al [Hori et al., 1994] implemented disturbance observers to compensate for the effect of the load torque by feeding back the motor velocity signal. State feedback gains were found by pole placement techniques. Dhaouadi et al [Dhaouadi et al., 1993] designed a speed controller based on a torque observer to increase the phase margin at the resonant frequency and to reduce the limit cycles resulting from the gear backlash. Kaneko et al [Kaneko et al., 1991] attained similar results designing an acceleration controller and using positive feedbacks from torque and load position. This suppressed the effects of both load torque and motor friction, setting a single inertia behavior to the system.

Even if the load motion compensation has been investigated in previous works, a general framework for this problem is currently missing in the literature. In this thesis, the generalized force control problem is summarized, for one degree of freedom (DOF), into a common framework with *only three elements*: a velocity source, a transmission, and a load. A parallel is drawn between a generic mechanical case and the two different actuators employed in the quadruped robot HyQ: electric and hydraulic. This analogy emphasizes that the feedback of the load velocity exists independently on the actuation system and also helps clarifying important robot design aspects that can be useful when building a robot.

Due to the intrinsic flow and pressure nonlinearities found in hydraulic actuators, linear controllers often do not provide satisfactory response and a nonlinear controller has to be designed. Nonlinear controllers have been extensively investigated especially for position control [Davliakos and Papadopoulos, 2007; Hahn et al., 1994; Sirouspour and Salcudean, 2000; Yao et al., 2000]. Regarding nonlinear force control with hydraulic actuators, [Alleyne and Hedrick, 1995] developed a nonlinear adaptive force controller to be used in hydraulic active suspension systems. In [Liu and Alleyne, 2000] and [Sirouspour and Salcudean, 2000] a Lyapunov-based control design technique was employed for performing force control. An input-output feedback linearization was employed in a cascade control architecture in [Ayalew and Kulakowski, 2006], where both position outer loop and inner pressure loop were linearized.

2.3   Compliance control

Compliance at the end-effector (or contact point) can be achieved in two ways: *passively* or *actively* [Mason, 1981; Whitney, 1985]. *Passive compliance* is obtained through hardware and can be attributed to physical elements such as the limited stiffness of the robot's links, the compliance of the actuator transmission (e.g. springs, gearboxes, harmonic drives, hydraulic oil, air, etc), and the softness of the robot "skin" (e.g. a layer of rubber around the end-effector). On the other hand, *active compliance* is usually achieved via the control of the joint torques, regardless of additional passive elements.

There are many ways of actively controlling the compliance at the end-effector, as discussed previously (e.g. impedance control [Hogan, 1985c], operational space control [Khatib, 1987], and virtual model control [Pratt et al., 2001]). However, its practical implementation has been challenging because of the absence of high-performance torque-controlled robots. Technological limitations such as computing power, communication technologies, sensors, and electronics integration used to cause stability problems and made impossible to increase the force gains, strongly limiting the closed-loop force control bandwidth [Seering, 1987]. The sluggish performance obtained restricted for many years the use of active compliance to applications with very slow dynamics [Klein and Briggs, 1980].

With the technological development of the last two decades, active compliance for highly-dynamic applications became feasible [Boaventura et al., 2012b; Luca et al., 2006]. For legged robots, an intuitive way to actively obtain a desired dynamic behavior is using virtual springs and dampers, that are virtually "attached" to the robot structure [Pratt et al., 2001]. These virtual components can have complex characteristics (e.g. nonlinear stiffness and damping) and can be situated anywhere in the robot, no matter how difficult it would be to physically realize and place them, which is a great advantage over passive compliance. Another benefit of using virtual components is that enables to change the components characteristics, such as stiffness and damping, on-the-fly while performing a certain task. For instance, theories about leg stiffness variations for terrains with different surface properties [Ferris et al., 1998] and also about reasons for gait selection in running quadrupeds

[Farley and Taylor, 1991] can be experimentally validated with an actively-compliant robot.

To ensure a stable contact between the environment and an actively-compliant leg, the compliance controller has to be passive. The range of achievable compliance parameters that keep the system stable is often called *Z-width* (where *Z* stands for impedance) [Colgate and Brown, 1994].

[Colgate and Schenkel, 1997] demonstrated that the passivity of a one DOF haptic device, when digitally controlled, depends also on the system sampling time. In this work it is also shown that the viscous friction of the device is the factor that limits the most the Z-width and consequently the proportional and derivative gains of the controller. Other important issues, such as filtering, can also limit the Z-width. In [Janabi-Sharifi et al., 2000], an adaptive filtering was proposed to estimate the velocity in discrete time. This filtering was able to successfully increase the Z-width of a hapitc device when compared with a Kalman filter and a filter based on the finite difference method.

Although the Z-width for virtual environments has been intensively investigated for haptics devices, there are no studies on the achievable range of impedances for virtual components in legged robots and neither studies that consider the torque closed-loop bandwidth impact in such range.

Chapter 3

Hydraulic Actuation

Hydraulic actuators transform hydraulic power into mechanical power based on Pascal's law, which states that "any change in pressure at any point of an incompressible and confined fluid at rest is transmitted equally in all directions". Even though a fluid is very slightly compressible, this property allows hydraulic actuators to produce large forces and high speeds, becoming thus a very attractive actuation system to dynamic robotic applications.

This section aims to familiarize the robotics community with this kind of actuation, providing insights into the main relevant fluid properties and components, such as pumps, valves and cylinder. Furthermore, the main advantages and drawbacks of this actuation technology are discussed.

Initially, the nonlinear model of the hydraulic actuation employed in HyQ is presented, and afterwards a linearization is carried out for controller design purposes. Despite of all nonlinearities that might be present in hydraulics, a linear model is able to sufficiently describe the hydraulic dynamics. Also, the next chapters will show that simple approaches are sufficient to very effectively control both the position and the force in hydraulic actuators.

3.1   Fluid properties

The most common fluids applied in hydraulic actuation are based on mineral oil. The oil is only very slightly compressible, a fact that makes it very suitable for transmitting power very quickly from one part of the system to the other. Meanwhile, the

oil also lubricates and cools down components such as valves and cylinders. HyQ uses the oil-based fluid ISO VG46.

Another fluid that is being focus of research especially in the last decades is the water. Although it is environmentally-friendly, clean, and safe, it is still a challenge to manufacture water-based hydraulic components due to corrosion, flow erosion, and higher internal leakage due to the low water viscosity[Garry W. Krutz, 2004]. A comparison between oil and water hydraulics can be found in [Yang et al., 2009].

The cleanness of the hydraulic fluid is an important issue in hydraulics, and a filter is always necessary. Some components require very low oil contamination levels to work properly. For instance, the HyQ valves [MOOG Inc., 2003], which have a tiny hydraulically driven stage, need a $3\mu m$ filter in the line. Particles in the order of tens of micrometers can already totally or partially clog the valve, reducing its performance or even rendering it unusable. Also, many sealing components, especially towards the end of their life-cycle, start to degrade and contaminate the oil. This fact augments the need of a good filtering system on a hydraulic circuit.

Another important issue in a hydraulic circuit is the temperature. The oil viscosity is highly dependent on its temperature: the viscosity drops when the temperature increases, and vice-versa. The viscosity has a big impact in the fluid dynamics, influencing the response characteristic of closed control loops, as well as its damping and also stability [Merritt, 1967]. To avoid changes in the system performance due to changes in the oil viscosity, the system should operate always around the same temperature. Thus, a cooler is usually installed in the hydraulic circuit to keep the oil in a steady-state temperature. For HyQ, the cooler kicks in when the oil reaches about $40°C$. The cooler is also a safety component, avoiding that the oil heats up too much so that it could damage components, and, in an extreme case, burn people.

3.1.1 Bulk Modulus

The most important fluid property for compliance control is its compressibility. The fluid compressibility is defined by its modulus of elasticity, the so-called *Bulk modulus* β, as follows:

$$\beta = -v_0 \left(\frac{\partial p}{\partial v} \right) \qquad (3.1)$$

where,

v_0: initial volume of the confined fluid $[m^3]$

v: final volume of the pressurized fluid $[m^3]$

p: pressure applied to the fluid $[Pa]$

For mineral oil, typical bulk modulus values range from 1400 to 1600 MPa. However, from a practical point of view, this might be a rough approximation, as the bulk modulus varies considerably with pressure, enclosed air, and pipe line compliance. An *effective Bulk modulus* β_e, which takes into account these effects, can be theoretically or empirically estimated. According to Eggerth's method [Jelali and Kroll, 2003], the effective Bulk modulus for HyQ was estimated to be $\beta_e = 1300$ MPa.

3.2 Pump

In hydraulics, the pump is the element that converts mechanical power into hydraulic power. It introduces power into the system by drawing fluid from a reservoir and releasing it with a certain pressure and flow into the output line. In hydraulics, non-SI units are still very often used to describe some physical quantities such as flow (l/min instead of the SI m^3/s) and pressure (bar instead of Pa). Using these commonly used units, the hydraulic power can be mathematically defined as:

$$p_{hyd} = \frac{q \, p}{600} \tag{3.2}$$

where,

p_{hyd}: hydraulic power $[kW]$

q: flow $[l/min]$

p: pressure $[bar]$

The most common sources of power to hydraulic pumps are electric motors and internal combustion engines. The former is usually used in indoor applications, since it is less noisy and it does not expel gases, and the latter in outdoor applications or where energy density is very critical.

Although combustion engines are about 3 times less efficient than electric motors, the energy density of fossil fuels is around 30 times higher than the energy density of the newest commercially available batteries (see Table 3.1). Therefore, many of the robots that are supposed to present a high level of energy autonomy use combustion engine.

	Efficiency	Energy density	Autonomy
Combustion Engine & Gasoline	30%	12 kWh/kg	40 min/kg
Electric Motor & Battery	90%	0.4 kWh/kg	4 min/kg

Table 3.1: Comparison between two different ways of driving a pump: a *combustion engine* with gasoline as fuel vs. an *electric motor* powered by high-energy batteries. The average efficiency of the actuators, the energy density of the fuel and battery, and the HyQ autonomy considering 1 kg of fuel/battery during a medium-velocity walking (5 kW/h energy consumption) are displayed for each actuation modality. To calculate it, the pump efficiency was considered to be 90% for both cases. The higher autonomy reached with an internal combustion engine is the reason for its use in autonomous hydraulic robots.

There are two main ways of transmitting the hydraulic power from the pump to the actuators. The first way is to use servovalves between the pump and the actuator to control the inlet actuator flow. These systems are called *valve-controlled* systems, and it is also employed in HyQ. The second is to connect the pump directly to the actuator. In this case, the inlet actuator flow is controlled by the speed of the pump. These systems are called *pump-controlled* systems, or also hydrostatic transmissions [Korn and of Technology, 1969]. The faster control capability of valve-controlled systems (servovalves have normally higher bandwidth than pumps) make this arrangement preferred in the majority of applications, including robotics, in spite of its lower theoretical maximum operating efficiency of 67% [Merritt, 1967]. Nevertheless, pump-controlled systems are more efficient and it can be an option for high-power applications that do not require fast responses.

Hydraulic pumps can be divided essentially into two big groups according to their pumping principle. Some pumps carry a fixed amount of fluid volume in every revolution, and they are named *fixed-displacement* or simply *gear pumps* (Fig. 3.1). These pumps always maintain the same outlet flow and a relief valve controls the
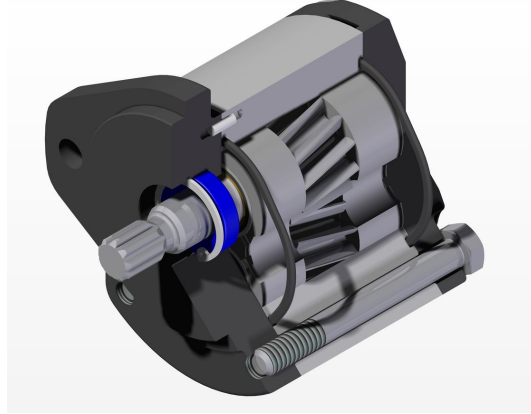
Figure 3.1: CAD picture of a fixed displacement gear pump. It has helical gears, which reduces the backlash (T3S model, from JIHOSTROJ a.s.)

pressure. Thus, if the hydraulic system does not use all of the flow, the remaining flow is returned to the tank through the relief valve. This represents a large loss of power which compromises the efficiency of the overall valve-controlled hydraulic system. On the other hand, *variable-displacement* pumps deliver a variable flow, which changes according to the system demand. This increases significantly the efficiency of a valve-controlled hydraulic circuit. Hence, in autonomous hydraulically-actuated robots that are valve-controlled, a variable-displacement pump should always be preferred to increase the robot efficiency and autonomy.

The main sources of losses of power in hydraulic pumps are friction and internal leakage. The efficiency of pumps can be very dependent on the system pressure: the higher the pressure, the higher the leakage flows and the lower the efficiency. For variable displacement pumps, at low pressures ($< 100\ bar$), the pump efficiency can reach 99%, and for higher pressures ($< 250\ bar$) the efficiency can drop to about 90%. Also the fluid temperature influences the pump efficiency since the temperature changes the viscosity, and consequently the (leakage) flow dynamics.

3.3 Valve

The valve is the hydraulic component in charge of controlling the hydraulic power, supplied by the pump, that goes to the actuators. The most common type of valve employed on hydraulically-actuated robots, including HyQ, are flow-control

servovalves. These valves regulate the output flow according to a control signal input.

HyQ uses off-the-shelf servovalves manufactured by Moog Inc. [MOOG Inc., 2003] (Fig. 3.2a). These valves have four ports (a, b, s, and t) and the valve spool is hydraulically-driven by a pilot stage. The port a connects the valve to the actuator chamber a and the port b to the chamber b, while the port s (stands for Supply) connects the valve to the pump and the port t (stands for Tank) connects the valve to the reservoir. The pressure at the valve ports a, b, s, and t are named as p_a, p_b, p_s, and p_t respectively. The valve input voltage is u. A hydraulic schematic for the valve is depicted in Fig. 3.2b
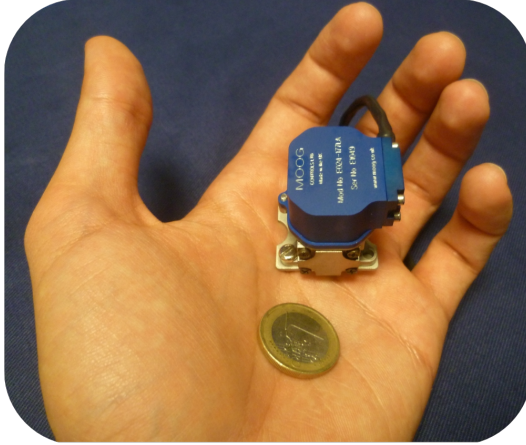
(a) Miniature MOOG E024 servovalves..
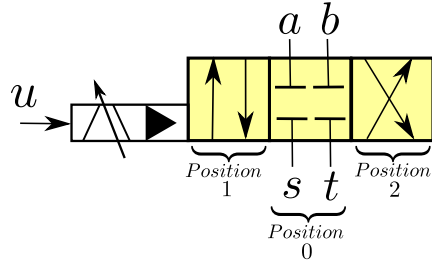
(b) ..and respective schematic

Figure 3.2: As seen in (a), compared to most of the available servovalves, the HyQ servovalves are small-size and light-weight. The valve schematic in (b) shows the three valve positions and its four ports a, b, s, and t.

In comparison with the commonly available servovalves, these miniature valves have many aspects that make them very suitable for robotics, such as:

- Very compact and light-weight (92 $grams$);

- High bandwidth ($\geq 250\ Hz$);

- High peak flow capability (7.5 l/min)

In the next sections, the main aspects regarding the valve modeling are discussed. Firstly, the valve spool dynamics is presented and, later, the flow equation and parameters are characterized.

3.3.1 Valve spool dynamics

In a servovalve, the spool is a movable part located inside the valve housing. By sliding back and forth it can, totally or partially, block and/or open the valve channels, setting like this the flow direction and magnitude.

The spool moves inside the valve housing according to the electrical input u applied to the valve. The relation between the valve input u and the spool position x_v can be modeled as a linear second order system:

$$\Delta x_v(s) = \frac{K_{spool}}{\frac{1}{\omega_v^2}s^2 + \frac{2D_v}{\omega_v}s + 1}\Delta u(s) \tag{3.3}$$

where,

K_{spool}: steady-state valve input-to-spool-position gain $[m/A]$

ω_v: valve spool angular frequency $[rad/s]$

D_v: valve spool damping

The gain K_{spool} relates the input, which for HyQ is a current, to the position of the spool in steady-state. The valve spool natural frequency F_v, where $F_v = \omega_v/2\pi$, is the most important parameter on the valve spool dynamics, and it can be approximated as the *valve bandwidth* [Merritt, 1967]. Essentially, F_v indicates how fast the spool can move. Also, since in the HyQ valves the spool is moved by a hydraulic-pilot stage, F_v is highly dependent on the supply pressure level: *the higher the supply pressure, the higher the valve bandwidth*. For instance, at the maximum supply pressure of 210 *bar*, F_v is about 250 *Hz* for $\pm25\%$ of the spool displacement, and about 100 *Hz* for $\pm100\%$. This high valve bandwidth is a key aspect for reaching high-performance torque and compliance control with hydraulic actuators. This important issue is discussed in more details in Chapters 5 and 6.

The hydraulic pressure and force dynamics are very fast and require a rapid actuation to control them. Therefore, attention must be paid in all the hardware levels to avoid inserting a slower element which could compromise the overall actuation bandwidth by adding delays to the response. For instance, the valve drivers, which usually convert voltage to current or *vice-versa*, must have a fast electrical dynamics so that it does not modify significantly the input from the controller to the valve.

3. HYDRAULIC ACTUATION

For most of the commercially available servovalves, the spool position cannot be measured. Moreover, usually there is a lack of mechanical details about the valve internal parts on the valve data sheet, so that it might be hard to define gains such as K_{spool}. To overcome these issues, it is useful to express the spool position in terms of the valve input u, that is:

$$\Delta u_v(s) = \frac{1}{\frac{1}{\omega_v^2}s^2 + \frac{2D_v}{\omega_v}s + 1} \Delta u(s) = \frac{1}{K_{spool}} \Delta x_v(s) \tag{3.4}$$

In the above definition, the u_v transfer function has unity gain in steady-state, and u_v has the same units of u, that for the HyQ valve is *Ampere*. Thus, u_v can be seen as a filtered version of the input u, where the lag introduced by the filter corresponds to the spool dynamics delay. In other words, u_v is a current that represents the actual spool position, as if it was the output of a spool position sensor. From here onwards, u_v will refer to the spool position, and x_v will not be used in the modeling.

(a) Under-lapped spool   **(b)** Zero-lapped spool   **(c)** Over-lapped spool
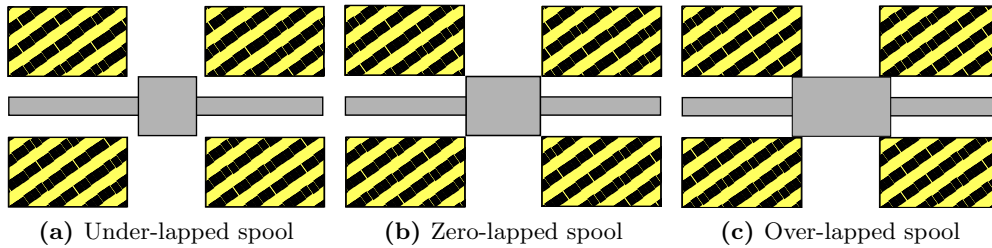
Figure 3.3: Different sizes of spool. In (a) the under-lapped spool land does not cover the whole port orifice and a large internal leakage is observed; in (b) the spool land aligns with the edge of the ports. This is the spool size of the valves used in HyQ; in (c) the spool is over-sized with respect to the valve ports and a dead-band is present around the null spool position.

3.3.2   Flow through valves

As discussed previously, the valve spool is the component in charge of controlling the flow direction and magnitude. The flow magnitude is controlled by manipulating the adjustable area $a(u_v)$ of the valve control orifices, which changes linearly with the spool position u_v, that is:

$$a(u_v) = W u_v \tag{3.5}$$

where,

W: area gradient $[m^2/A]$

Besides the orifice area $a(u_v)$, the flow magnitude q through an orifice is also a function of the differential pressure Δp across the orifice, and it can be written in the following ways:

$$q = C_d a(u_v) \sqrt{\frac{2\Delta p}{\rho}} = C_d W u_v \sqrt{\frac{2\Delta p}{\rho}} = \frac{C_d W \sqrt{2}}{\sqrt{\rho}} u_v \sqrt{\Delta p} = K_v u_v \sqrt{\Delta p} \tag{3.6}$$

where,

C_d: discharge coefficient ($C_d \approx 0.6$ is often assumed [Merritt, 1967])

ρ: oil density (for HyQ ISO VG46 oil, $\rho = 850 \ kg/m^3$)

K_v: valve gain

As seen in the right-side of Eq. 3.6, the term that multiplies $u_v \sqrt{\Delta p}$ can be written as a constant K_v and it accounts essentially for the valve size. Again, due to the lack of information in most valve data sheets, it might be difficult to estimate W and also to obtain a precise equation for the flow. Thus, another definition for this sizing constant, which is based on common data sheet information, is presented [De Negri et al., 2008].

3.3.2.1 Valve gain

Usually, the way valve manufacturers give information about the valve size in the data sheets is through three parameters: *nominal flow*, *nominal pressure drop*, and *nominal valve input*. In many cases, the nominal points are given as the maximum ones, however any operating point within the valve flow range can be used for sizing it.

The standard procedure for obtaining these three nominal parameters is by interconnecting the valve control ports a and b ($p_a = p_b$), applying a constant electrical

input u_{vn} to the valve, and measuring the steady-state flow q_n which passes through the valve.
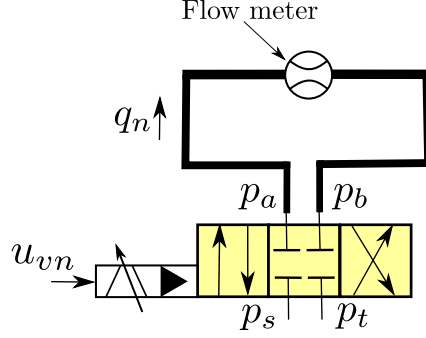
Figure 3.4: Hydraulic circuit schematic for determining the valve gain

Assuming the pressure drop Δp_{n1} across the ports s and a is the same as across the ports b and t ($\Delta p_{n1} = p_s - p_a = p_b - p_t$), the nominal pressure drop across all the valve control ports can be written as:

$$\Delta p_{n2} = (p_s - p_a) + (p_b - p_t) = p_s - p_t = 2\Delta p_{n1} \tag{3.7}$$

where,

Δp_{n1}: nominal pressure drop across one control port of the valve $[Pa]$

Δp_{n2}: nominal pressure drop across two control ports of the valve $[Pa]$

It is important to identify in the valve data sheet which pressure drop is given, whether it is across one or two control ports, to be able to properly estimate the valve size. The most common pressure drop to be reported in data sheets is Δp_{n2}.

Once the nominal flow with the respective pressure drop and valve input are known, Eq. 3.6 can be rewritten for the nominal case and the valve gain K_v can be redefined as:

$$K_v = \frac{c_d W \sqrt{2}}{\sqrt{\rho}} = \frac{q_n}{u_{vn}\sqrt{\Delta p_{n1}}} = \frac{q_n}{u_{vn}\sqrt{\frac{\Delta p_{n2}}{2}}} \tag{3.8}$$

where,

u_{vn}: nominal valve input $[A]$

q_n: nominal flow $[m^3/s]$

The definition of the valve sizing gain K_v shown in Eq. 3.8 is very easily obtainable from the valve datasheet. Therefore, from here onwards the flow equation will always be written in terms of K_v.

3.4 Asymmetric Cylinder

The most common actuator in hydraulics is the linear actuator, or hydraulic cylinder. It converts hydraulic energy into mechanical energy. It consists of two main parts: a hollow cylindrical body and a piston, which is inserted inside the body and is free to move. The piston rod is the part which connects the piston to an external object, or more generically, to a load.

There are essentially two kind of cylinders: cylinders with rods at both extremities (named symmetric or double-rod cylinders) and cylinders with only one rod (called asymmetric or single-rod cylinders), as depicted in Fig. 3.5a.

(a)   **(b)**
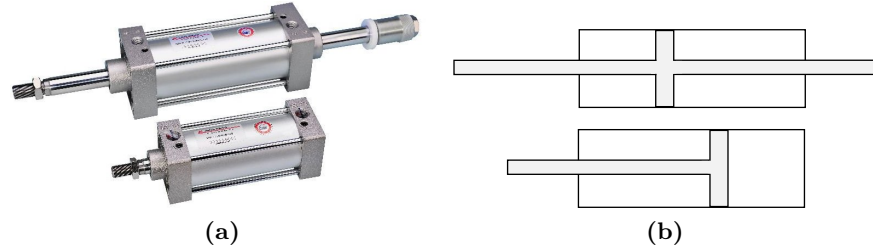
Figure 3.5: (a): Picture of symmetric and asymmetric cylinders; and (b) the respective hydraulic schematic used to represent these components.

As mentioned before, HyQ uses asymmetric cylinders for moving the HFE and KFE joints (see Fig. 1.2a and Fig. 1.2b). In these kind of cylinders, the asymmetry leads to different effective chamber areas. The larger area A_p is called piston area. The rod-side area, also called annular area, is smaller by a factor of $\alpha < 1$. Symmetric cylinders have $\alpha = 1$. For the HyQ cylinders, this area ratio is $\alpha \cong 0.61$.

The hydraulic schematic shown in Fig. 3.6 represents the hydraulic actuation circuit that is employed in the hydraulically-actuated joints of HyQ. It is composed of a servovalve and an asymmetric cylinder. The inertial load is represented by a mass M_l with viscous friction B_l, which includes mainly the friction in the joint
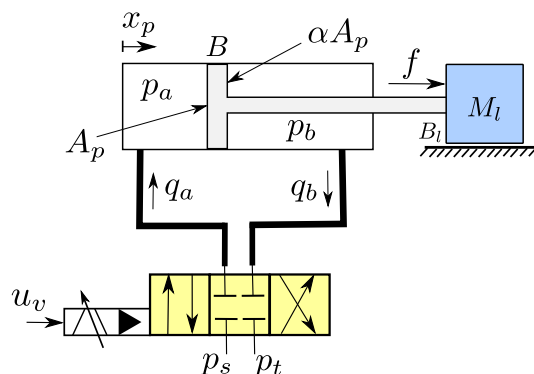
Figure 3.6: Hydraulic schematic of the HyQ hydraulic actuation system. The valve, in yellow, choses the direction and magnitude of the chamber flows q_a and q_b. These flows change the pressures p_a and p_b inside the asymmetric cylinder chambers, and consequently the force f that is transmitted to the load, which takes into account the cylinder friction B. The load, represented by the blue block, is simplified in this schematic to be an inertial load with constant mass M_l and friction B_l.

bearings. Throughout this thesis, the color blue will always be associated to the load, and the yellow color to the actuation.
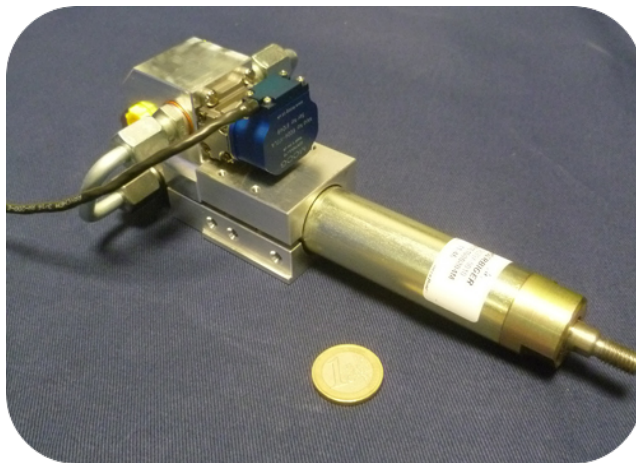
Figure 3.7: The HyQ valves are attached as close as possible to the cylinder to reduce the hydraulic compliance of the system. Also, rigid tubes are used to connect both. These two design decisions increase the actuation bandwidth.

The HyQ valves are assembled on a small manifold which is mounted directly on the cylinder body. The valve ports a and b are connected to the cylinder ports through rigid tubes in an "u" shape, as depicted in Fig. 3.7. To place the valves as close as possible to the cylinder has the main goal of reducing the compliance of the

system. This reduction is achieved by reducing the amount of oil between the valve and the cylinder and also by using rigid tubes instead of flexible hoses. This topic is further discussed in Chapter 7.

The chamber flows q_a and q_b can be modeled as Eq. 3.6, depending on the valve spool position u_v:

$$
q_a = \begin{cases} K_v u_v \sqrt{p_s - p_a}, & u_v > 0. \\ K_v u_v \sqrt{p_a - p_t}, & u_v < 0. \end{cases} \tag{3.9}
$$

$$
q_b = \begin{cases} K_v u_v \sqrt{p_b - p_t}, & u_v > 0. \\ K_v u_v \sqrt{p_s - p_b}, & u_v < 0. \end{cases} \tag{3.10}
$$

Neglecting external and internal leakages, the mass conservation principle can be applied to each of the chambers by using the continuity equation, and the following well-known expressions for the chamber pressure dynamics can be written [Merritt, 1967]:

$$
\dot{p_a} = \frac{\beta_e}{v_a} \left(q_a - A_p \dot{x}_p \right) \tag{3.11}
$$

$$
\dot{p_b} = \frac{\beta_e}{v_b} \left(-q_b + \alpha A_p \dot{x}_p \right) \tag{3.12}
$$

where,

v_a: chamber a volume $[m^3]$

v_b: chamber b volume $[m^3]$

The chamber volumes vary according to the piston position x_p. The volume inside the hoses which connect the valve to the actuator is also included in the total volumes chamber, which can be defined as follows:

$$
v_a = V_{pl} + A_p x_p \tag{3.13}
$$

$$
v_b = V_{pl} + (L_c - x_p)\alpha A_p \tag{3.14}
$$

where,

V_{pl}: pipe line volume $[m^3]$

L_c: cylinder length or stroke (total distance the cylinder can travel) $[m]$

The pipe line volume V_{pl} depends on the internal diameter D_{pl} of the pipe and on its length L_{pl} ($V_{pl} = L_{pl}\pi D_{pl}^2/4$).

3.4.1 Hydraulic Force

The hydraulic force f_h created by the hydraulic cylinder is defined as the force created exclusively by the difference of pressures in the cylinder chambers, that is:

$$f_h = A_p p_a - \alpha A_p p_b = A_p(p_a - \alpha p_b) \tag{3.15}$$

The pressure difference $p_a - \alpha p_b$ can also be defined as the *load pressure* for an asymmetric cylinder. It is the pressure difference that effectively produces a force. Thus, Eq. 3.15 can be rewritten as:

$$f_h = A_p p_l \tag{3.16}$$

where,

p_l: load pressure ($p_l = p_a - \alpha p_b$) $[Pa]$

Taking the time derivative of Eq. 3.15, and considering the definition of load pressure as well as Eq. 3.11 and 3.12, the hydraulic force dynamics can be obtained as follows:

$$\dot{f}_h = \frac{A_p \beta_e}{v_a}(q_a - A_p \dot{x}_p) - \frac{\alpha A_p \beta_e}{v_b}(-q_b + \alpha A_p \dot{x}_p) \tag{3.17}$$

3.4.2 Friction Force

Since hydraulic components such as cylinders are used to work with fluids under high pressures, the piston sealing is usually quite tight to avoid internal leakages. This small clearance in between the cylinder piston and the cylinder body increases substantially the friction forces, which work also as natural damping, but also insert nonlineartities into the system.

The friction forces in a hydraulic cylinder can be modeled as follows [Jelali and Kroll, 2003]:

$$f_f = B\dot{x}_p + sign(\dot{x}_p) \left(F_{c_0} + F_{s_0}\ e^{-\frac{|\dot{x}_p|}{C_s}} \right) \tag{3.18}$$

where,

B: viscous friction coefficient $[Ns/m]$

F_{c_0}: Coulomb friction coefficient $[N]$

F_{s_0}: static friction coefficient $[N]$

C_s: static decay friction coefficient (known also as Stribeck velocity) $[m/s]$
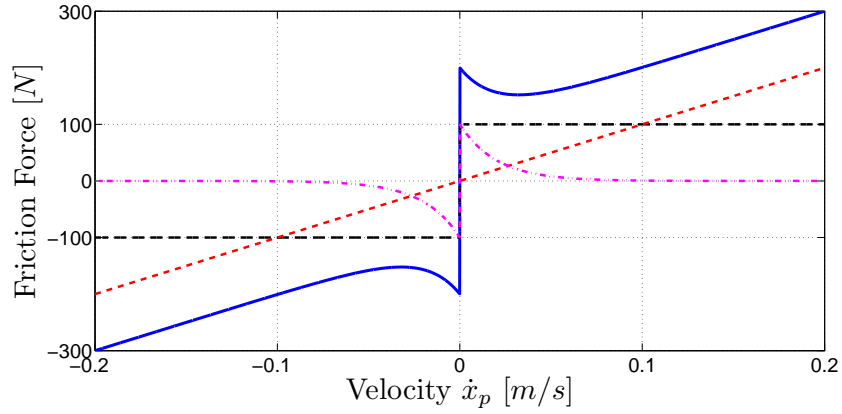
Figure 3.8: Typical theoretical friction curve for a hydraulic actuator. The continuous blue line shows the total friction force f_f, and it is the sum of all the other three curves. The black dashed line plots the constant Coulomb friction for $F_{c_0} = 100\ N$; the pink dot-dashed line the static friction with $F_{s_0} = 100\ N$ and $C_s = 0.02$; and the red dashed line the linear viscous friction considering $B = 1000\ Ns/m$.

As seen in Eq. 3.18 and Fig. 3.8, the friction forces in hydraulic cylinders can be decomposed essentially in three main components:

- Viscous friction: it is the only linear component of the friction forces, and because of that it is usually the only force considered in the modeling. It is proportional to the piston velocity magnitude.

- Coulomb friction: it is a constant force that depends only on the sign of the piston velocity.

- Static friction: this force acts mainly at zero velocity. It decays exponentially to zero as soon as the piston starts to move.

All these parts create the well-known Stribeck forces curve, shown in Fig. 3.8 [Armstrong-Hélouvry et al., 1994]. For HyQ, the friction forces f_f were estimated experimentally by measuring the hydraulic force f_h with pressure sensors, and also the load force f with a load cell, as shown in Eq. 3.19. The results were very dependent on the system velocity. As seen in Fig. 3.9a, 3.9b, and 3.9c, a hysteresis nonlinearity was always present, especially for positive velocities. At low velocities the curve was more linear, being the Coulomb friction estimated as $F_{c_0} \cong 100\ N$. The viscous friction coefficient was estimated as $B \cong 1000\ Ns/m$. Some models that describe the nonlinearities seen in these experimental data can be found in the literature [Xuan Bo Tran and Yanada., 2012].

The high friction in hydraulic actuators is a drawback from the energy point of view. A significant part of the fluid power is lost in friction. However, this high friction is also beneficial for the force controller. It essentially increases the stability margins. The higher the friction, the faster the hydraulic force controller can respond. This topic is further discussed in Section 7.1.2.

3.4.3 Load force

The force that is truly applied to a load attached to the piston rod is called herein *load force*, and it is defined as the difference between the hydraulic force f_h produced by the load pressure and the forces f_f lost through friction, that is:

$$f = f_h - f_f \tag{3.19}$$

where,

f: load force $[N]$

In the HyQ leg, the load force is measured by a small-size load cell attached in series with the piston rod (Fig. 3.10b). As it is described in Chapter 5, this measurement is used to control the torque that is applied to the joints of HyQ, and also to control its compliance.

The miniature load cell, shown in Fig. 3.10a has an axial force measurement range of $10000\ N$ ($-5000\ N$ to $5000\ N$). This large range is required to guarantee mechanical robustness and control accuracy even in presence of the big impacts that
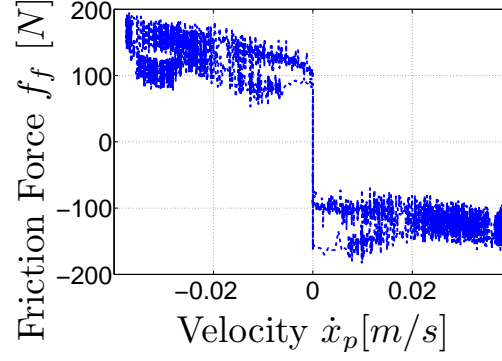
(a) 0.1 Hz
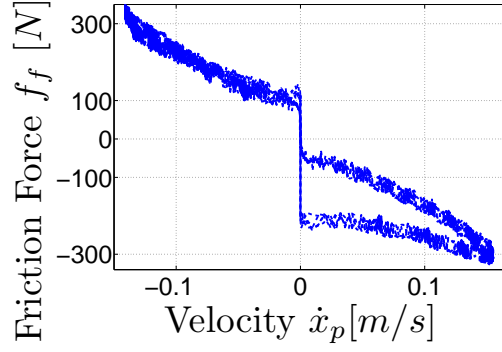
(b) 1 Hz
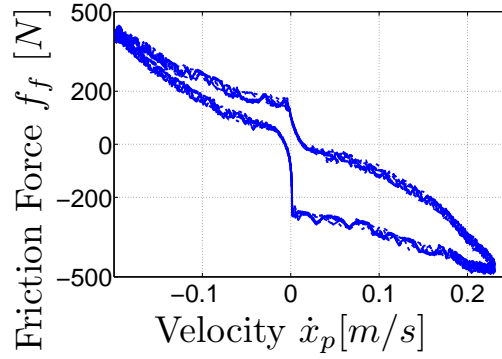
(c) 3 Hz

Figure 3.9: Friction forces obtained with the HyQ cylinder for different velocity ranges. A sinusoidal motion was applied to the piston at different frequencies. As seen, many nonlinearities are present in the response. For a low speed experiment shown in (a), the viscous friction coefficient was estimated as $B \cong 1000 \ Ns/m$ while the Coulomb friction as $F_{c_0} \cong 100 \ N$.

Figure 3.10: The HyQ load cell, shown in (a), is able to measure axial forces in the range of $-5000\ N$ to $5000\ N$. In (b), the HyQ cylinder is connected with the load cell in series with the rod.

the HyQ leg can face during locomotion tasks. It has a relatively small noise of $\pm 1\%$ in comparison with the whole range. However, in absolute values it is relatively high ($\pm 50\ N$). This noise degrades the force control performance when it has to control forces that are in the range of the noise. Strong filtering cannot be used because it would introduce significant delays into the fast force dynamics and reduce the overall system stability. This issue is further discussed in Section 6.2.

The load force dynamics can be expressed by taking the time derivative of Eq. 3.19. Taking into account Eq. 3.9, 3.10, and 3.17, and considering only the viscous friction, the following load force dynamics can be written:

$$\dot{f} = \dot{f}_h - B\ddot{x}_p =$$

$$= \begin{cases} -\beta_e A_p^2 \left(\frac{1}{v_a} + \frac{\alpha^2}{v_b} \right) \dot{x}_p - B\ddot{x}_p + \beta_e A_p K_v \left(\frac{\sqrt{p_s - p_a}}{v_a} + \frac{\alpha\sqrt{p_b - p_t}}{v_b} \right) u_v, & u_v > 0. \\ -\beta_e A_p^2 \left(\frac{1}{v_a} + \frac{\alpha^2}{v_b} \right) \dot{x}_p - B\ddot{x}_p + \beta_e A_p K_v \left(\frac{\sqrt{p_a - p_t}}{v_a} + \frac{\alpha\sqrt{p_s - p_b}}{v_b} \right) u_v, & u_v < 0. \end{cases}$$

$$(3.20)$$

The load force dynamics equation shown in Eq. 3.20 might be the most important equation in this chapter. The force model-based controllers, described in Chapter 5, are based on this equation.

3.5 Hydraulic actuation linearized model

A linear model can be very useful for understanding the system characteristics through the use of linear system's tools, such as transfer functions, root locus, and

bode plot. These tools also help in designing simple linear controllers, such as the well-known PID controller.

In this section, the nonlinear model described in the previous section will be linearized around an operating point $P_\oslash = (p_{a\oslash}, p_{b\oslash}, u_{v\oslash})$. The most common operating point used in the literature to linearize the nonlinear hydraulic dynamics is $P_\oslash = (\frac{p_s}{2}, \frac{p_s}{2}, 0)$ [Jelali and Kroll, 2003]. The operating pressures $p_{a\oslash}$ and $p_{b\oslash}$, in this case, are the same and maintain a symmetric cylinder in equilibrium, that is, with load pressure $p_{l\oslash} = 0$.

For an asymmetric cylinder, for achieving a force equilibrium the operating pressures cannot be the same since the effective piston areas are different. Thus, a more convenient operating point can be defined as $P_\oslash = (\frac{\alpha p_s}{1+\alpha}, \frac{p_s}{1+\alpha}, 0)$. With these new pressures $p_{a\oslash}$ and $p_{b\oslash}$, the load pressure $p_{l\oslash}$ for an asymmetric cylinder is zero and the cylinder is in equilibrium. For $\alpha = 1$ (symmetric cylinder) the previous operating point $P_\oslash$ is obtained.

Regarding the operating valve spool position, $u_{v\oslash} = 0$ is normally chosen since most of the valves have symmetric opening and the spool is mainly moving around this null position.

In the next sections, the nonlinear flow and pressure dynamics will be linearized around this equilibrium point $P_\oslash$ to obtain a linear load force dynamics.

3.5.1   Valve coefficients

The chamber flows dynamics, described in Eq. 3.9 and 3.10, are nonlinear. To linearize them, they can be expanded using Taylor series about the equilibrium point $P_\oslash$ and truncated after the first differential term [Merritt, 1967]:

$$\Delta q_a = K_{qa}\Delta u_v - K_{ca}\Delta p_a \tag{3.21}$$

$$\Delta q_b = K_{qb}\Delta u_v - K_{cb}\Delta p_b \tag{3.22}$$

The terms K_{qa}, K_{qb}, K_{ca}, and K_{cb} are part of the so-called *valve coefficients*. These coefficients represent the main characteristics of a valve, and they can be defined as:

$$K_{qa} = \left.\frac{\partial q_a}{\partial u_v}\right|_{P_\oslash} = \begin{cases} K_v\sqrt{p_s - p_{a\oslash}}, & u_v > 0. \\ K_v\sqrt{p_{a\oslash} - p_t}, & u_v < 0. \end{cases} \tag{3.23}$$

$$K_{qb} = \left.\frac{\partial q_b}{\partial u_v}\right|_{P_\oslash} = \begin{cases} K_v\sqrt{p_{b\oslash} - p_t}, & u_v > 0. \\ K_v\sqrt{p_s - p_{b\oslash}}, & u_v < 0. \end{cases} \tag{3.24}$$

$$K_{ca} = -\left.\frac{\partial q_a}{\partial p_a}\right|_{P_\oslash} = \begin{cases} \frac{K_v u_{v\oslash}}{2\sqrt{p_s - p_{a\oslash}}}, & u_v > 0. \\ \frac{-K_v u_{v\oslash}}{2\sqrt{p_{a\oslash} - p_t}}, & u_v < 0. \end{cases} \tag{3.25}$$

$$K_{cb} = -\left.\frac{\partial q_b}{\partial p_b}\right|_{P_\oslash} = \begin{cases} \frac{-K_v u_{v\oslash}}{2\sqrt{p_{b\oslash} - p_t}}, & u_v > 0. \\ \frac{K_v u_{v\oslash}}{2\sqrt{p_s - p_{b\oslash}}}, & u_v < 0. \end{cases} \tag{3.26}$$

K_{qa} and K_{qb} are called *flow gains*. They describe how much flow is produced for a certain valve opening. They also directly affect the open-loop gain in a system and therefore its stability. The *flow-pressure coefficients* K_{ca} and K_{cb} characterize the leakage in the valve, that is, how the flow is influenced by a change in pressure. They directly affect the damping of the valve-actuator combination [Merritt, 1967].

Another important valve characteristic is the *pressure sensitivity*, which is defined by:

$$K_{pa} = \left.\frac{\partial p_a}{\partial u_v}\right|_{P_\oslash} = \frac{K_{qa}}{K_{ca}} \begin{cases} \frac{2K_v(p_s - p_{a\oslash})}{u_{v\oslash}} & u_v > 0. \\ \frac{-2K_v(p_{a\oslash} - p_t)}{u_{v\oslash}}, & u_v < 0. \end{cases} \tag{3.27}$$

$$K_{pb} = \left.\frac{\partial p_b}{\partial u_v}\right|_{P_\oslash} = \frac{K_{qb}}{K_{cb}} \begin{cases} \frac{-2K_v(p_{b\oslash} - p_t)}{u_{v\oslash}} & u_v > 0. \\ \frac{2K_v(p_s - p_{b\oslash})}{u_{v\oslash}}, & u_v < 0. \end{cases} \tag{3.28}$$

As seen in Eq. 3.25 and 3.26, and Eq. 3.27 and 3.28, for an ideal valve at the null position ($u_{v\oslash} = 0$) the flow-pressure coefficients are theoretically zero ($K_{ca} = K_{cb} = 0$) and the pressure sensitivities are infinity ($K_{pa} = K_{pb} = \infty$). Nevertheless, more realistic values can be obtained through experimental tests with the valve to increase the fidelity of the model. For instance, in Fig. 3.11b the pressure sensitivities for the HyQ valves can be estimated through the slope of the pressure curves as $K_{pa} \cong K_{pb} \cong 5.7 \cdot 10^{11}\ [Pa/A]$.

The hydraulic circuit used to obtain the pressure sensitivities are depicted in Fig. 3.11a. In this circuit, the valve ports are blocked, a slow sinusoidal input u
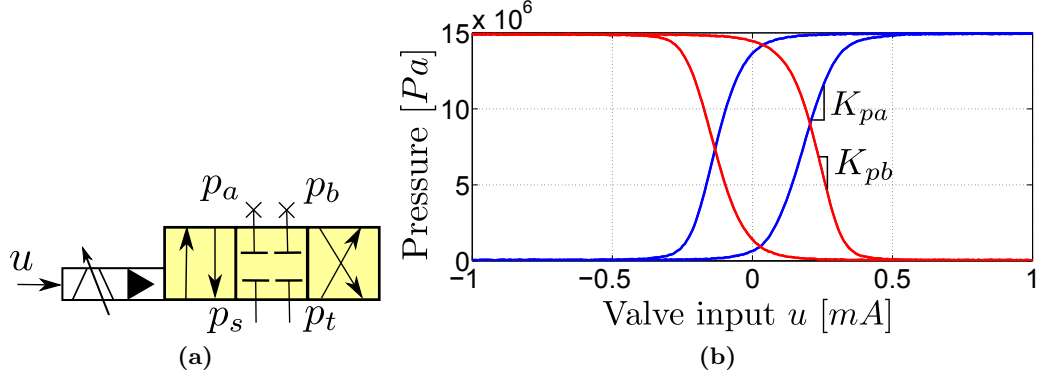
Figure 3.11: (a): Hydraulic schematic of the hydraulic circuit used for obtaining the pressure sensitivity coefficient. The valve ports a and b are blocked and a very slow sinusoidal input u is applied to the valve. The results are shown in (b), where the valve pressure sensitivity coefficients can be estimated as the slope of the pressure curves. The pressure p_a is displayed in blue and p_b in red.

is applied to the valve, and the pressures p_a and p_b are measured using pressure sensors.

The HyQ valve flow gain is presented in the valve datasheet. Thus, an experimental test to identify them was not necessary.

3.5.2 Steady-state and constant volume constraints

The most common linear model found in the literature for describing the force dynamics produced by a hydraulic cylinder is based on the following well-known steady-state flow relations:

$$q_a = A_p \dot{x}_p \tag{3.29}$$

$$q_b = \alpha A_p \dot{x}_p \tag{3.30}$$

Combining these steady-state equations with Eq. 3.9 and 3.10, and assuming p_s and p_t constant, the pressures p_a and p_b can be linearized as a function of the load pressure p_l as:

$$\Delta p_a = \frac{1}{1+\alpha^3}\Delta p_l \tag{3.31}$$

$$\Delta p_b = \frac{-\alpha^2}{1+\alpha^3} \Delta p_l \tag{3.32}$$

Another common simplification done in the literature during linearization is to assume that the cylinder volumes v_a and v_b are constant. This is a valid assumption if the piston velocity $\dot{x}_{p\oslash}$ and valve opening $u_{v\oslash}$ at the operating point are both zero.

Thus, considering v_a and v_b constant, the hydraulic force (Eq. 3.17) can be linearized as:

$$\Delta \dot{f}_h = \left.\frac{\partial \dot{f}_h}{\partial q_a}\right|_{P_\oslash} \Delta q_a + \left.\frac{\partial \dot{f}_h}{\partial q_b}\right|_{P_\oslash} \Delta q_b + \left.\frac{\partial \dot{f}_h}{\partial \dot{x}_p}\right|_{P_\oslash} \Delta \dot{x}_p =$$
$$\frac{A_p \beta_e}{v_{a\oslash}} \left(\Delta q_a - A_p \Delta \dot{x}_p\right) - \frac{\alpha A_p \beta_e}{v_{b\oslash}} \left(-\Delta q_b + \alpha A_p \Delta \dot{x}_p\right) \tag{3.33}$$

where,

$v_{a\oslash}$: volume of the chamber a at the operating point $[m^3]$

$v_{b\oslash}$: volume of the chamber b at the operating point $[m^3]$

Taking into account the linear relations for the flows (Eq. 3.21 and 3.22) and pressures (Eq. 3.31 and 3.32), the linear hydraulic force dynamics can be written as:

$$\Delta \dot{f}_h = K_{\dot{x}_p} \Delta \dot{x}_p + K_{u_v} \Delta u_v + K_{f_h} \Delta f_h \tag{3.34}$$

where the linear constants $K_{\dot{x}_p}$, K_{u_v}, and K_{f_h} are defined as:

$$K_{\dot{x}_p} = -A_p^2 \beta_e \left(\frac{1}{v_{a\oslash}} + \frac{\alpha^2}{v_{b\oslash}}\right) \tag{3.35}$$

$$K_{u_v} = A_p \beta_e \left(\frac{K_{qa}}{v_{a\oslash}} + \frac{\alpha K_{qb}}{v_{b\oslash}}\right) \tag{3.36}$$

$$K_{f_h} = \frac{\beta_e}{1+\alpha^3} \left(\frac{K_{ca}}{v_{a\oslash}} - \frac{\alpha^3 K_{cb}}{v_{b\oslash}}\right) \tag{3.37}$$

The Laplace transform of Eq. 3.34 can be represented with the block diagram shown in Fig. 3.12. The inertial load has mass M_l. The cylinder friction B was
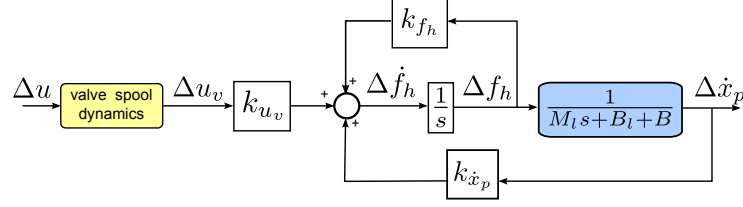
Figure 3.12: Block diagram of the hydraulic force dynamics. The load, represented by the blue block, was modeled as a constant mass M_l. The cylinder friction B was added to the load friction B_l since the rod can be considered part of the load when a hydraulic force f_h is applied.

added to the load damping B_l. As it is shown in Chapter 7, this load damping B_l cannot be neglected in the hydraulic modeling. Also, if the valve spool dynamics shown in Eq. 3.4 is taken into account, the following transfer function can be written:

$$\frac{\Delta f_h(s)}{\Delta u(s)} = \left(\frac{1}{\frac{1}{\omega_v^2} s^2 + \frac{2D_v}{\omega_v} s + 1} \right) \left(\frac{K_{u_v}(M_l s + B_l + B)}{(s - K_{f_h})(M_l s + B_l + B) - K_{\dot{x}_p}} \right) \tag{3.38}$$

Once the linear hydraulic force dynamics, shown in Eq. 3.34, was obtained, the linear load force dynamics can be finally written using the relation presented in Eq. 3.20, where only the cylinder viscous friction B is considered.

$$\Delta \dot{f} = K_{\dot{x}_p} \Delta \dot{x}_p + K_{u_v} \Delta u_v + K_{f_h} \Delta f_h - B \Delta \ddot{x}_p \tag{3.39}$$
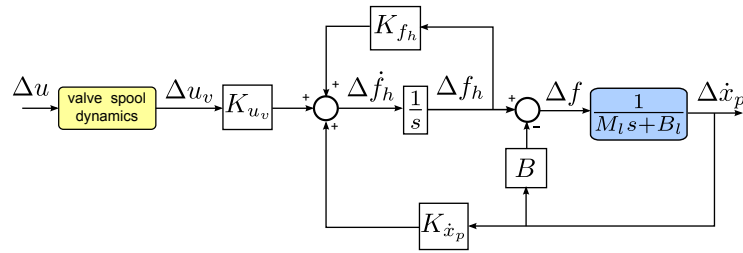
Figure 3.13: Block diagram for the linearized load force

Again, by applying the Laplace transform to Eq. 3.39, the block diagram shown in Fig. 3.13 can be obtained. In this block diagram, the cylinder friction B was separated from the load dynamics. Thus, the load dynamics block depicts only the load friction B_l, which is derived mainly from bearings. Considering the valve spool

dynamics, the following transfer function can be written:

$$\frac{\Delta f(s)}{\Delta u(s)} = \left(\frac{1}{\frac{1}{\omega_v^2} s^2 + \frac{2D_v}{\omega_v} s + 1} \right) \left(\frac{K_{u_v}(M_l s + B_l)}{(s - K_{f_h})(M_l s + B_l + B) - K_{\dot{x}_p}} \right) \qquad (3.40)$$

The linear hydraulic force Δf_h and the linear load force Δf have very similar dynamics. As seen in Eq. 3.38 and Eq. 3.40, they have exactly the same poles. However, the locations of the zeros are different. The zero from the load force dynamics Δf is closer to the origin then the zero from the hydraulic force dynamics Δf_h, as shown in the root locus in Fig. 3.14b and 3.14a. The high-frequency poles from the valve dynamics are not depicted in these root loci.
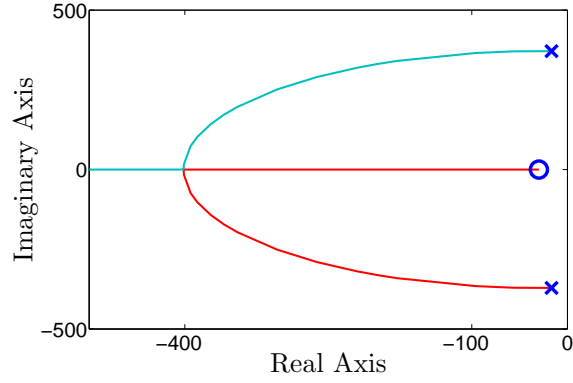
(a) Δf_h root locus
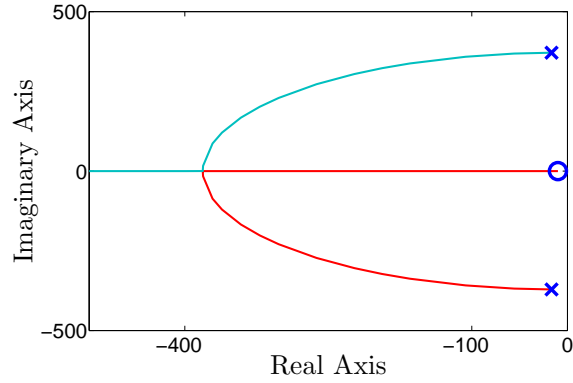
(b) Δf root locus

Figure 3.14: Root locus for the dominant poles of the linear hydraulic ((a)) and load forces ((b)). The poles from the valve dynamics are in high frequencies and are not displayed in this graph. The complex conjugated poles from the load and cylinder/valve dynamics are depicted with blue crosses. As seen in (a), Δf_h has a real zero at around $s = -30 \ rad/s$ while Δf in (b) has a zero at $s = -10 \ rad/s$. Both are represented by blue circles. This higher frequency zero permits to obtain a faster closed-loop force dynamics with the hydraulic force than with the load force.

Chapter 4

Load Velocity Feedback in Force Dynamics

For reasons of causality, force is always controlled over a transmission element that is deformable or compressible. The force is transmitted from the actuator to the load through this compliant transmission element.

This chapter introduces a new framework for representing the force dynamics in terms of three generic elements: a velocity source, a transmission, and a load. Using basic physical principles, it is shown that this framework fits for all different types of actuator types that perform force control. To illustrate it, this chapter will draw a parallel between a generic mechanical case, and the two different actuators employed on HyQ: electric and hydraulic.

This new framework, based on the transmission stiffness, has the strong advantage of making explicit an important and intrinsic physical phenomena in force control: a natural feedback of the load velocity into the force dynamics [Boaventura et al., 2012a]. This chapter discusses the limitations this feedback imposes onto the controlled system, and how these limitations can be overcome.

4.1   Generic Mechanical Case

The force dynamics depends on both actuator, transmission, and load dynamics. This interaction always exists, independently of the kind of actuator and/or load.

4. LOAD VELOCITY FEEDBACK IN FORCE DYNAMICS

Fig. 4.1 shows a basic mechanical system composed of three basic elements: an actuator, represented by an ideal velocity source vs; a transmission with stiffness K_t; and a generic *load*.
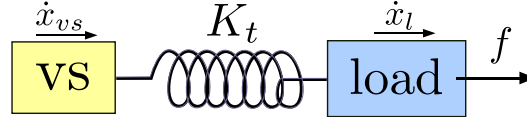
Figure 4.1: Generic spring-mass system representing a velocity source, that drives a load through a compliant transmission.

Since springs are impedances, they have velocity as input to their dynamics and force as output. On the other hand, masses are admittances and have forces as input and velocity as output to their dynamics [Hogan, 1985b]. In Fig. 4.1 the velocity source vs is a mass, accelerated by an external actuator, and has an instantaneous velocity $\dot{x}_{vs}$, which is transmitted to the transmission spring. The spring output force f acts on the load mass, which is accelerated and has an instantaneous velocity $\dot{x}_l$. The load force dynamics $\dot{f}$ can be written as:

$$\dot{f} = K_t \left(\dot{x}_{vs} - \dot{x}_l \right) \tag{4.1}$$

The presence of $\dot{x}_l$ in Eq. 4.1 underlines that the dynamics of the force that is transmitted to the load depends also on the load itself, and not only on the actuator. The actuator dynamics defines how quickly the velocity $\dot{x}_{vs}$ can be changed. On the other hand, the load dynamics determines how fast the load velocity $\dot{x}_l$ changes given an input force.
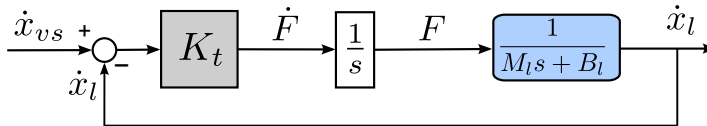
Figure 4.2: Block diagram for a generic velocity source, acting on a load through a transmission stiffness K_t. The load velocity $\dot{x}_l$ is clearly being fed back into the load force dynamics.

This interaction between force and load dynamics is intrinsic to the force physics, independent of the actuation and load characteristics, and it can be mathematically seen as a *load velocity feedback*. Based on the block diagram of Fig. 4.2, given that

M_l is the mass and B_l is the damping of the load, the following transfer function can be obtained:

$$\frac{f(s)}{\dot{x}_{vs}(s)} = \frac{K_t (M_l s + B_l)}{s (M_l s + B_l) + K_t} \tag{4.2}$$

Looking at Fig. 4.2, it can be noticed that the pole of the load dynamics appears also as a zero of the force transfer function in Eq. 4.2. This result occurs regardless of how fast the actuation dynamics is [Dyke et al., 1995]. Thus, if a force control loop is closed, both the controller gain and the performance of the system are limited by the frequency of this zero.

In the following sections the details of the two different actuation systems present on the HyQ platform (electric and hydraulic) are presented. These next sections show that their models fit well into the generic mechanical case introduced in this section.

4.2 Hydraulic Actuation

In hydraulics, the velocity source is the pump and valve together. The pump pressurizes the fluid and the valve controls the fluid flow that is going into the hydraulic cylinder. An accumulator is usually placed upstream of the valve to compensate for the pump dynamics and eventual pressure drops so that the supply line can be considered a perfect pressure source. Therefore, the velocity source dynamics is determined only by the valve and flow dynamics. The transmission is characterized by the fluid, and the transmission stiffness by the fluid compressibility and volume.

The hydraulic force dynamics, shown in Eq. 3.17, consists of a balance between the forces created in the cylinder chambers a and b. Both chamber forces fit the same generic form described in Eq. 4.1, that is: a *controllable input velocity*, represented by a flow; the *load velocity*, represented by the piston velocity $\dot{x}_p$, in this case multiplied by a gain that is equal to the respective chamber area; and a *transmission stiffness*, which depends on the Bulk modulus and on the chamber area and volume. To make it easier to identify these elements, Eq. 3.17 is rewritten as follows:

$$\dot{f}_h = K_{tha} (q_a - A_p \dot{x}_p) - K_{thb} (-q_b + \alpha A_p \dot{x}_p) \tag{4.3}$$

where,

$K_{tha} = \frac{A_p \beta_e}{v_a}$: hydraulic transmission stiffness for chamber a $[Pa/m]$

$K_{thb} = \frac{\alpha A_p \beta_e}{v_b}$: hydraulic transmission stiffness for chamber b $[Pa/m]$

(a) Chamber hydraulic stiffness   **(b)** Equivalent hydraulic stiffness
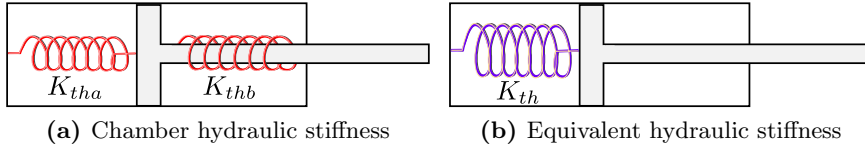
Figure 4.3: (a): Hydraulic transmission springs for each chamber, with stiffness K_{tha} for chamber a and K_{thb} for chamber b. (b): Equivalent hydraulic stiffness for the whole system, with stiffness K_{th}.

The two different hydraulic transmission stiffnesses K_{tha}, and K_{thb} created by the two cylinder chambers, can be modeled as parallel springs [Skinner and Long, 1998], as depicted in Fig. 4.3a. Thus, a resultant hydraulic stiffness K_{th} can be defined as:

$$K_{th} = K_{tha} + K_{thb} = A_p \beta_e \left(\frac{1}{v_a} + \frac{\alpha}{v_b} \right) \tag{4.4}$$

Using the definition of the equivalent hydraulic transmission K_{th}, Eq. 4.3 can be rewritten in a more similar form to the generic case in Eq. 4.1, that is:

$$\dot{f}_h = K_{th} \left(q_e - A_e \dot{x}_p \right) \tag{4.5}$$

where,

q_e: equivalent flow $[m^3/s]$

A_e: equivalent area $[m^2]$

The equivalent flow q_e and area A_e can be obtained through simple algebraic manipulations as:

$$q_e = \frac{v_b q_a + \alpha v_a q_b}{v_b + \alpha v_a} \tag{4.6}$$

$$A_e = \frac{-K_{\dot{x}_p}}{K_{th\oslash}} = A_p \left(\frac{v_b + \alpha^2 v_a}{v_b + \alpha v_a} \right) \tag{4.7}$$

It is important to underline that Eq. 4.5 is exactly equivalent to Eq. 3.17. However, Eq. 4.5 is written in a more convenient form since it explicits an important physical characteristic of the system: the transmission stiffness. Also, the presence of the piston velocity $\dot{x}_p$ in Eq. 4.5 makes clear the natural feedback of the load dynamics into the hydraulic force dynamics. As previously discussed, this phenomenon is intrinsic to any force control problem and does not depend on the actuator type.

Since the equivalent flow q_e (Eq. 4.6) is based on the nonlinear chamber flows q_a and q_b, it is also a nonlinear function. To linearize it, the same procedure used in Section 3.5 can be applied to obtain a linearized function:

$$\Delta q_e = K_{qe}\Delta u_v + K_{ce}\Delta p_l \tag{4.8}$$

where,

K_{qe}: equivalent flow gain $[m^3/sA]$

K_{ce}: equivalent flow-pressure coefficient $[m^3/sPa]$

where the linear constants K_{qe} and K_{ce} are defined as:

$$K_{qe} = \frac{K_{u_v}}{K_{th\oslash}} = \frac{v_{b\oslash}K_{qa} + \alpha v_{a\oslash}K_{qb}}{v_{b\oslash} + \alpha v_{a\oslash}} \tag{4.9}$$

$$K_{ce} = \frac{K_{f_h}A_p}{K_{th\oslash}} = \frac{1}{1+\alpha^3}\left(\frac{v_{b\oslash}K_{ca} - \alpha^3 v_{a\oslash}K_{cb}}{v_{b\oslash} + \alpha v_{a\oslash}}\right) \tag{4.10}$$

Thus, the linearized hydraulic force dynamics $\Delta\dot{f}_h$ can be represented as:

$$\Delta\dot{f}_h = K_{th\oslash}\left(\Delta q_e - A_{e\oslash}\Delta\dot{x}_p\right) \tag{4.11}$$

where,

$K_{th\oslash}$: hydraulic transmission stiffness at the equilibrium point $P_\oslash$ $[Pa/m]$

$A_{e\oslash}$: equivalent area at the equilibrium point $P_\oslash$ $[m^2]$

Eq. 4.11 is an alternative way to represent the hydraulic force dynamics. In comparison with Eq. 3.34, it has the advantage of including explicitly the hydraulic transmission characteristics at the equilibrium point $K_{th\oslash}$. The transmission stiffness is an essential physical quantity in the force dynamics. The stiffer the trans-

mission, the faster the force dynamics. A knowledge of the transmission stiffness can give important insights into the force control design and also into the robot mechanical design. This topic is further discussed in Section 7.2.

The block diagram of the linearized hydraulic force shown in Eq. 4.11 is presented in Fig. 4.4. This block diagram is equivalent to the one developed in the previous section (Fig. 3.13), where the hydraulic force was defined using the constants $K_{\dot{x}_p}$, K_{u_v}, and K_{f_h}.
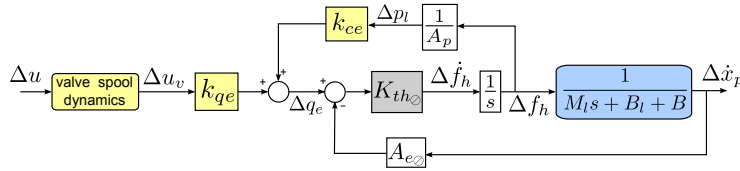
Figure 4.4: Block diagram for an open-loop hydraulic actuator. The blocks related to the valve are depicted in yellow. The piston velocity $\Delta \dot{x}_p$ is multiplied by the equivalent area $A_{e\oslash}$ and is transformed in a flow. This flow is then fed back into the force dynamics. This block diagram is equivalent to the one shown in Fig. 3.12.

Neglecting the valve spool dynamics, the hydraulic force transfer function can be written based on the block diagram of Fig. 4.4:

$$\frac{\Delta f_h(s)}{\Delta u_v(s)} = \frac{K_{th\oslash}K_{qe}\left(M_l s + B_l + B\right)}{\left(M_l s + B_l + B\right)\left(s - \frac{K_{th\oslash}K_{ce}}{A_p}\right) + K_{th\oslash}A_{e\oslash}} \tag{4.12}$$

The valve spool dynamics shown in Fig. 4.4 is being neglected in Eq. 4.12. Despite this fact, the transfer function in Eq. 4.12 is equivalent to the one shown in Eq. 3.38. Nevertheless, it has the advantage of being expressed in terms of a hydraulic transmission stiffness $K_{th\oslash}$.

The velocity framework can also be applied to the load force, which is the physical quantity that is being controlled in the HyQ leg to achieve compliance. Thus, also Eq. 3.40 can be written in this more convenient framework:

$$\frac{\Delta f(s)}{\Delta u_v(s)} = \frac{K_{th\oslash}K_{qe}\left(M_l s + B_l\right)}{\left(M_l s + B_l + B\right)\left(s - \frac{K_{th\oslash}K_{ce}}{A_p}\right) + K_{th\oslash}A_{e\oslash}} \tag{4.13}$$
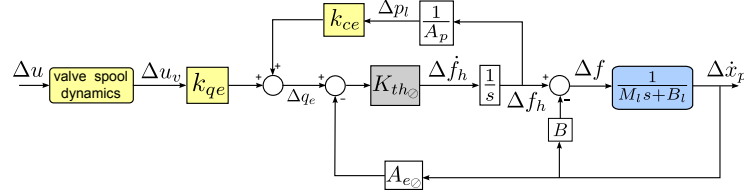
Figure 4.5: Block diagram for an open-loop force dynamics. Differently from the hydraulic force shown in Fig. 4.4, there are two paths were the velocity influences the load force dynamics: one through A_e and another through the viscous friction B in the hydraulic cylinder. This block diagram is equivalent to the one shown in Fig. 3.13.

4.3 Electric Actuation

This section shows that the natural velocity feedback happens also with electric actuators. It is one more example to demonstrate that the velocity feedback is an intrinsic phenomena of force control, independent of the actuator type.

As discussed in Section 1.2, HyQ uses electric motors to actuate the HAA joint of its legs (Fig. 1.2a). An electric motor has its rotor as velocity source for the transmission, which in most of the cases in robotics, including HyQ, consists of a gear box.

The gear box behaves as a rigid torsional spring, introducing an elasticity between the rotor and the load. This elasticity defines the rotational transmission stiffness K_{te} for the electric actuation. HyQ uses a harmonic drive with ratio $1:100$ and stiffness $K_{te} = 2.7{\cdot}10^4 \ Nm/rad$ [Focchi et al., 2012].

The dynamics of the torque t_l transmitted to the load is the rotational version of the linear dynamics shown in Eq. 4.1, that is:

$$\dot{t}_l = K_{te}\left(\frac{\dot{\theta}_m}{N} - \dot{\theta}_l\right) \tag{4.14}$$

where,

    $\dot{\theta}_m$: angular velocity of the rotor of the electric motor $[rad/s]$

    $\dot{\theta}_l$: angular velocity of the load $[rad/s]$

    N: gear ratio

The motor dynamics can be modeled as a second order system, with inertia J_m and damping coefficient B_m, which includes both rotor and gear box viscous frictions.

4. LOAD VELOCITY FEEDBACK IN FORCE DYNAMICS

Considering a load with inertia J_l and damping B_{l_θ}, the following transfer function from the motor input u_m to the load torque t_l can be obtained (see [Boaventura et al., 2012b] for model equations):

$$\frac{\Delta t_l(s)}{\Delta u_m(s)} = \frac{K_i K_{te} (J_l s + B_{l_\theta}) N}{(J_l s^2 + B_{l_\theta} s + K_{te}) N^2 (R (J_m s + B_m) + K_i K_\omega) + R K_{te} (J_l s + B_{l_\theta})} \tag{4.15}$$

where,

K_i: current-to-torque motor constant $[Nm/A]$

K_ω: back-emf motor constant $[Vs/rad]$

R: motor coil resistance $[ohm]$

The electrical voltage-to-current dynamics is neglected. As for the previous cases, the torque transfer function has a zero due to the load dynamics. All the poles (one real and two complex) depend on both load and motor parameters. The corresponding block diagram is shown in Fig. 4.6, where, again, it is evident the presence of a natural velocity feedback into the torque dynamics.
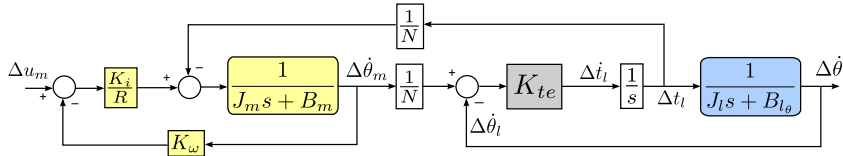
Figure 4.6: Block diagram for an open-loop electric motor: once again, the load velocity feedback is clearly present in the dynamics.

	Hydraulics	Electrics
Actuator	Pump + valve	Stator
Velocity Source	Fluid (e.g. oil)	Rotor
Transmission	Fluid (e.g. oil)	Gear box
Transmission Stiffness	$K_{th} = 1 \cdot 10^7 \ N/m$	$K_{te} = 2.7 \cdot 10^4 \ Nm/rad$

Table 4.1: Actuation description: the actuator accelerates a mass (velocity source) that transmits velocity to a springy transmission. The transmission produces a force, which is transmitted to a load and accelerates it.

Chapter 5

Force Control

It has long been known that torque and impedance control of the joints and end-effector are very fundamental requirements in robotics [Whitney, 1985]. Even though decades ago theoretical studies produced control strategies that required the application of torques to the robot joints [Hogan, 1985c; Khatib, 1987], at that time the limitation in sensory, hardware, and computational technology restricted significantly the performance in practical implementations. However, even if nowadays technology is not a limitation to the implementation of force-based control approaches anymore, to date most available articulated robots are still only position controlled.

Nevertheless, in most robotic systems the motor system is attached to a rigid link, which is an inertial load. Inertial loads are admittances to which one cannot physically apply velocity but only force: velocity is the outcome, i.e. the velocity is the integral of the applied force over time [Hogan, 1985a]. Therefore, *the input to a robot (a rigid body system) is fundamentally determined to be a torque (or generalized force)*, and a joint-space torque controller makes straightforward the application of such inputs.

Given the importance of force control in rigid body robots, a whole chapter is dedicated to this topic. This chapter firstly introduces the rigid body dynamics and afterwards it presents some control approaches for controlling the force at the HyQ joints. This chapter also aims to demonstrate that hydraulic control is not as complicated as commonly thought.

An important remark: in HyQ, to control the joint torques is equivalent to controlling the forces at the hydraulic cylinders since the cylinder rod is rigidly connected to the joints. The joint torques can be computed by simply multiplying the cylinder force by the actual lever arm length l_{la} [Semini, 2010]. Note that throughout this thesis the terms *force control* and *torque control* are used interchangeably.

5.1 Rigid Body Systems

Most of the manipulators and robots presently are designed with rigid links. Rigidity generally guarantees kinematic accuracy [Wang et al., 1998]. For this reason, they are usually modeled as rigid body systems. This assumption simplifies the modeling and increases the computational efficiency [Featherstone and Orin, 2000; Sciavicco and Siciliano, 2001].

Rigid body systems consist of a composition of rigid bodies connected together via joint elements. There are many types of joints, such as: revolute, translational, spherical, planar, universal, etc. In HyQ, all the joints are of the revolute type. This kind of joint has only one rotational DOF, and all the other DOF are constrained by the joint mechanism.

The joint-space rigid body dynamics defines a relation between the torques (or generalized forces) acting on the robot joints and the accelerations they produce. It can be expressed as:

$$\boldsymbol{\tau} = \boldsymbol{M}(\boldsymbol{q})\ddot{\boldsymbol{q}} + \boldsymbol{h}(\boldsymbol{q}, \dot{\boldsymbol{q}}) + \boldsymbol{J}(\boldsymbol{q})^T \boldsymbol{f_{ext}} \tag{5.1}$$

where,

$\boldsymbol{\tau}$: joint torque vector

$\boldsymbol{q}$: joint angles vector, $\boldsymbol{q} = \{\theta_1, \theta_2, ..., \theta_n\}$

$\boldsymbol{h}(\boldsymbol{q}, \dot{\boldsymbol{q}})$: Coriolis, centripetal, and Gravity force vector

$\boldsymbol{M}(\boldsymbol{q})$: joint-space inertia matrix

$\boldsymbol{f_{ext}}$: vector of external forces acting at the end-effector

$\boldsymbol{J}(\boldsymbol{q})^T$: Jacobian transpose matrix of the end-effector forces

The vectors $\boldsymbol{\tau}$, $\boldsymbol{q}$, $\dot{\boldsymbol{q}}$, $\ddot{\boldsymbol{q}}$, and $\boldsymbol{h}(\boldsymbol{q}, \dot{\boldsymbol{q}})$ are n-dimensional, where n is the number of (independent) joints of the robot. The vector $\boldsymbol{h}(\boldsymbol{q}, \dot{\boldsymbol{q}})$ contains all the acceleration-

independent terms, while the matrix $\boldsymbol{M}(\boldsymbol{q})$ maps joint accelerations into joint torques. The matrix $\boldsymbol{M}(\boldsymbol{q})$ has important characteristics: it is symmetric, positive-definite, and has dimension $n \times n$ [Featherstone and Orin, 2000]. The external force vector $\boldsymbol{f_{ext}} = \{f_x, f_y, f_z, \tau_x, \tau_y, \tau_z\}$ is usually described as a 6 dimension vector, being 3 linear forces and 3 torques that act at the end-effector. The Jacobian $\boldsymbol{J}(\boldsymbol{q})$ has dimension $n \times 6$ and maps the forces acting at the end-effector into joint torques.

The rigid body model of a robot can be very useful. On one hand, the forward rigid body dynamics, or simply *forward dynamics*, consists in calculating the joint accelerations given the joint torques. The forward dynamics is very important for simulating and observing the rigid body systems behavior when a certain torque is applied to joints. On the other hand, the inverse rigid body dynamics, or simply *inverse dynamics*, works out the required joint torques to realize given joint accelerations.. The inverse dynamics can become a very powerful tool to improve the performance of robots. If a desired trajectory is known *a priori*, the desired accelerations $\ddot{\boldsymbol{q}}_{ref}$ can be calculated and fed into the inverse dynamics to obtain the *feed forward* torques $\boldsymbol{\tau_{ff}}$ required to follow that desired trajectory. Considering no external forces, the rigid body inverse dynamics can be written as follows:

$$\boldsymbol{\tau_{ff}} = \boldsymbol{M}(\boldsymbol{q})\ddot{\boldsymbol{q}}_{ref} + \boldsymbol{h}(\boldsymbol{q}, \dot{\boldsymbol{q}}) \tag{5.2}$$

where,

$\boldsymbol{\tau_{ff}}$: feed forward inverse dynamics torques vector

$\ddot{\boldsymbol{q}}_{ref}$: desired joint accelerations vector

As shown in [Buchli et al., 2009], one immediate advantage of inverse dynamics control is that it allows for compliant and more robust locomotion since it permits a reduction of the position gains without sacrificing tracking performance. Having these capabilities is not only desirable but mandatory for locomotion in unstructured and partially unknown environments. This topic is discussed in more details in Section 6.1.1.

Rigid body manipulators and robots can be classified into two groups according to the freedom of their bases: *fixed-base* robots are rigidly attached to a fixed support in the environment (e.g. industrial robot arms); *floating-base*, or *free-floating* robots

are not fixed to their environments and are free to move about (e.g. legged mobile robots, flying robots, swimming robots). The theory presented in this chapter refers to fixed-base robots but a generalization to non-fixed (i.e. floating) base robots is possible.

5.2 Force control design

As previously discussed, robots are typically modeled as rigid body systems, having torques as input to their dynamics. In general, to achieve high control performance it is important to measure and to control the inputs applied to the plant with the highest possible accuracy. Therefore, for rigid robots a high-fidelity torque source is of great significance.

Due to the naturally high hydraulic stiffness, the pressure dynamics has a high bandwidth and requires a very fast flow controller [Neal, 1974]. The key aspects for achieving high-performance torque control with a hydraulic system are [Boaventura et al., 2012b]:

- to use servovalves with high flow control bandwidth to exploit the naturally high hydraulic stiffness;

- to improve the torque controller performance using model-based control.

Both aspects together are able to provide a high control bandwidth that is able to handle the high hydraulic stiffness and high-frequency inputs.

Servovalves with sufficient bandwidth for a torque control application have been a very well established technology for many decades [Thayer, 1958]. While at the time of their introduction analog control technology had to be used to exploit their full bandwidth, today even low-cost commodity hardware is powerful enough to be used to develop flexible digital controllers for such a system.

As described in Section 3.3, HyQ uses fast valves with bandwidth of about 250 Hz. This section describes the control designs that permit to take advantage of such fast valves to produce a high-bandwidth closed-loop force control.

To close the force loop, the sign convention for the torques and forces are shown in Fig. 5.1. The torques sign was chosen based on the angles sign (Fig. 6.2): positive torques create a positive displacement. On the other hand, the force sign convention

defines a positive load force when the cylinder piston is extending. Thus, the lever arm l_{la}, which is the variable that relates force and torque, will obtain a sign so that the torque and force conventions match. That is, for the HFE joint the lever arm l_{la} is negative (since a positive force creates a negative torque) and for KFE it is positive (since a positive force creates a positive torque)
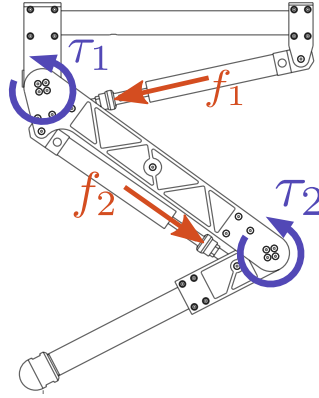
Figure 5.1: Torque and force sign conventions for the HyQ left front leg. In blue, the hip τ_1 and knee τ_2 torques, which are based on the sign definition of the leg angles (Fig. 6.2). The force sign definition is defined based on the cylinder motion: the force is positive for forward movements. To match the torque and force sign definitions, the lever arm l_{la} of the HFE joint is negative and of the KFE is positive.

5.2.1 Force PID

The PID error feedback controller is by far the most popular controller since it is simple and robust [Levine, 1996]. However, for performing force control the derivative term can cause stability problems during numerical differentiation due to the high level of noise in strain-gage-based force sensors. In this case, the derivative term might not be convenient, and a PI should be preferred. Also, if the controllable variable is the hydraulic force instead of the load force, the damping introduced by derivative term is not necessary due to the high viscous friction in the piston.

The simple block diagram shown in Fig. 5.2 illustrates the feedback control of the force from the hydraulic dynamics. The torque is obtained by multiplying the load force Δf by the lever arm l_{la} [Semini, 2010]. The output of the PID controller u_{PID} controls the HyQ valves, that are part of the block *Hydraulic dynamics*.
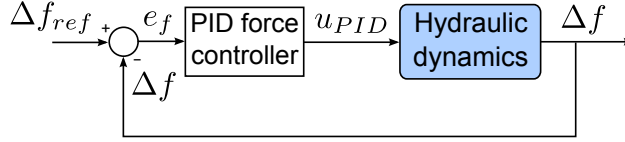
Figure 5.2: Block diagram of the PID force control approach. The torque is fed back and a control output u_{PID} is calculated based on the force tracking error e_f and sent to the valve input.

A parallel PID controller output u_{PID} can be defined by the following transfer function. It has two real poles, being one at the origin and one at $s = -N$ due to the derivative filter. In addition, it has two zeros that can be complex or real.

$$\frac{u_{PID}(s)}{e_f(s)} = K_p + \frac{K_i}{s} + K_d \; s \left(\frac{N}{s + N} \right) \tag{5.3}$$

where,

e_f: force error

K_p: proportional gain

K_i: integral gain

K_d: derivative gain

N: derivative filter coefficient

The variable to be controlled is the force Δf that is transmitted to the load, defined by the open-loop transfer function in Eq. 3.40. Using a PID controller to close the force loop, the root locus presented in Fig. 5.3 is obtained. The poles and gains from the open-loop force transfer function are displayed in blue, and the ones from the controller in red. The closed-loop poles are marked with black squares.

As seen in Fig. 5.3, there is a dominant closed-loop pole at very low frequency, close to the origin. This pole slows down significantly the response and the settling time can increase to the order of many tens of seconds. Practically, it means that the open-loop zero cancels out the effect of the controller integrator. In other words, when the load has low friction, a traditional PID controller behaves in practice as a PD controller and the system will always present an error in steady-state. More details about this topic and also results with a PID controller are shown in Section 7.1.
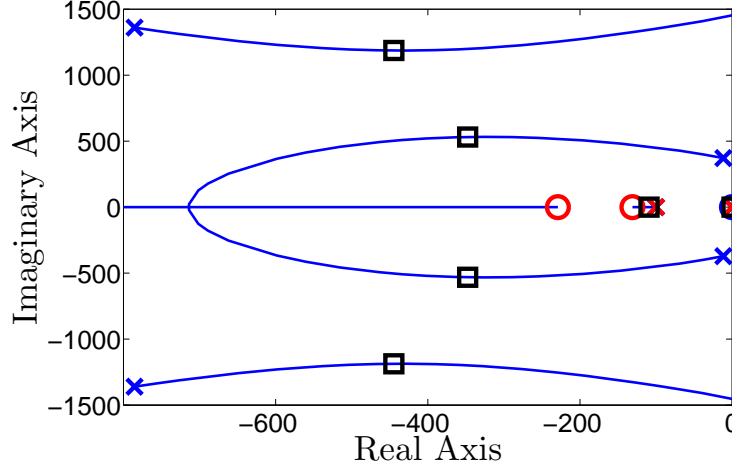
Figure 5.3: Root locus for the closed-loop load force using a PID controller. The closed-loop poles are marked with black squares, the open-loop poles and zero in blue, and the controller poles and zeros in red. As seen, the open-loop zero, which is very close to the origin, creates a dominant closed-loop pole at very low frequencies which slows down the system response.

5.2.2   Load velocity compensation + PI controller

As described in Chapter 4, the dynamics of the force that is transmitted from the actuator to the load depends not only on the actuator dynamics but also on the load dynamics. The load dynamics introduces a zero into the force transfer function, which limits the achievable force bandwidth. This bandwidth limitation as well as the impossibility of increasing the system performance by feedback controllers, such as a PID, is well-known [Alleyne et al., 1998] and was discussed in the previous section.

Therefore, this section introduces a feed forward controller which aims to cancel out the load dynamics influence and increase the force tracking performance. The feedback controller is simplified to a PI, instead of the PID presented in the previous section.

Considering the generic scheme of Fig. 4.1, an intuitive way for compensating this load motion influence is to measure the load velocity $\dot{x}_l$ and to *continuously* apply, with our ideal velocity source, an extra velocity $\dot{x}_{ex} = \dot{x}_l$. By applying $\dot{x}_{ex}$, the generic load force dynamics (Eq. 4.1) is given by:

$$\dot{f} = K_t \left[(\dot{x}_{vs} + \dot{x}_{ex}) - \dot{x}_l\right] = K_t \dot{x}_{vs} \qquad (5.4)$$

Taking the Laplace transform of Eq. 5.4, it is possible to write the transfer function for the velocity-compensated system as:

$$\frac{f(s)}{\dot{x}_{vs}(s)} = \frac{K_t}{s} \qquad (5.5)$$

Comparing the compensated force transfer function in Eq. 5.5 with the non-compensated shown in Eq. 4.2, it is possible to notice that the mathematical effect of the load velocity compensation is to algebraically eliminate the term K_t from the denominator of Eq. 4.2. This is equivalent to open the natural loop created by the load velocity feedback. By eliminating this term, a perfect zero/pole cancellation becomes possible and the same velocity-compensated dynamics shown in Eq. 5.5 is obtained.

To cancel out the influence of the load zero in the force dynamics is the main goal of the load velocity compensation. With this zero/pole cancellation, it is possible to theoretically increase the gains without making the system unstable, taking the dominant closed-loop pole to higher frequencies.

Considering a hydraulic actuator, the extra velocity $\dot{x}_{ex}$ represents an extra flow q_{ex} that has to be supplied by the valve. This extra flow that has to be supplied depends on whether the hydraulic force or load force is being controlled. Since HyQ does not have pressure sensors to measure the chambers pressure, it is not possible to control in closed-loop the hydraulic force, which is defined only as the pressure difference in the chambers (Eq. 3.15). The load force, instead, includes the friction forces (Eq. 3.19) and represents the force that is applied to the load. It is measured by a load cell, which is used to close a control loop.

Although HyQ controls only the load force, the control of the hydraulic force is presented in the next section. It might be useful for those who have chamber pressure sensors in the hydraulic circuit. Also, the analysis of the velocity compensation for the hydraulic force illustrates well the purpose of this feed forward control.

5.2.2.1 Hydraulic force control

As seen in the hydraulic force block diagram in Fig. 4.4, the velocity is fed back as a flow into the force dynamics with a gain $A_{e\oslash}$. It is easy to see that to compensate for the quantity an extra flow $q_{ex} = A_{e\oslash}\Delta\dot{x}_p$ must be supplied.

To design a control signal to supply this extra flow q_{ex}, the valve spool dynamics will be neglected. It is assumed that a valve input voltage Δu is instantaneously converted into valve spool opening Δu_v. Thus, feeding back the piston velocity $\Delta\dot{x}_p$, the valve input u_{vc} that compensates for the velocity feedback is:

$$u_{vc} = \frac{A_{e\oslash}\Delta\dot{x}_p}{K_{qe}} \tag{5.6}$$

The control effort u_{vc} can be applied as a feed forward term which aims to compensate for the changes in force due to the load velocity. This term can then be summed with a the control effort u_{PI} from a PI controller, as described in Section 5.2.1. The block diagram of this force control approach is shown in Fig. 5.4.
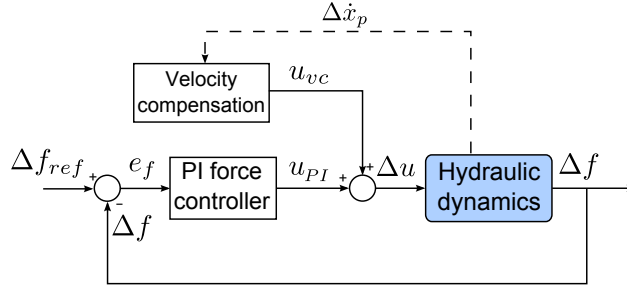
Figure 5.4: Block diagram of the velocity compensation + PI hydraulic force control approach. The velocity compensation is a feed forward control which feeds back the velocity state $\Delta\dot{x}_p$ to calculate u_{vc}. This term is then summed with the PI feedback force control output u_{PI}, resulting in the final valve input Δu.

In terms of block diagram, to supply this extra flow q_{ex} is equivalent to opening the velocity loop, which is equivalent to making $A_{e\oslash} = 0$ in Fig. 4.4. By looking at Eq. 4.12, it is clear that, by algebraically eliminating the term $K_{th\oslash}A_{e\oslash}$, the same zero/pole cancellation that was discussed before is obtained.

This is a great improvement in the system dynamics since the zero at low frequencies which limits the system response is eliminated. Using the control architecture presented in Fig. 5.4, a simulation has been carried out to demonstrate the

very satisfactory capabilities of such simple approach when the hydraulic force is controlled.

A PI controller was tuned differently for the compensated and non-compensated system. In all cases, the gains were chosen to obtain the fastest non-oscillatory closed-loop response possible (margin phase of at least 60 deg).

Parameters based on the hydraulic system of HyQ ($A_{e\oslash} = 1.63 \cdot 10^{-4}$, $K_{th\oslash} = 5.5 \cdot 10^{10}$, $K_{qe} = 0.018$, $K_{ce} = -7.85 \cdot 10^{-11}$, all in SI units) were used to simulate the hydraulic dynamics and obtain the response shown in Fig. 5.5. The load with mass was set as $M_l = 50\ kg$ and damping as $B = 1000\ Ns/m$.
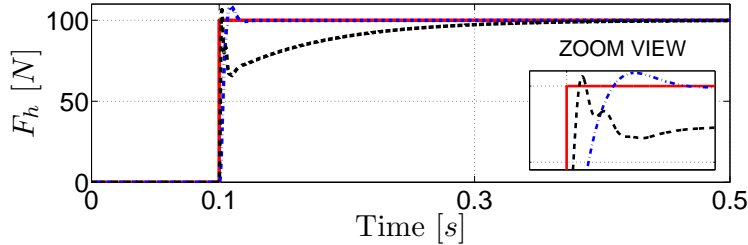
Figure 5.5: Hydraulic force step response in simulation for a hydraulic cylinder. The solid red line shows the hydraulic force reference, the dashed black the non-compensated response, and the dot-dashed blue line the response when the load motion is compensated for. The zoom view, around 0.1 s, clearly shows the force drop due to the load motion influence.

As seen in Fig. 5.5, the velocity-compensated system has a much smaller settling time than the non-compensated one. Furthermore, the influence of the load motion is clearly noticed in the non-compensated response. That is, it raises as quickly as the compensated one, but after a short period the force magnitude drops drastically. This drop happens exactly when the load starts to move and "uncompress" the transmission spring. This reduces the oil pressure inside the chamber, and consequently the force.

5.2.2.2 Load force control

In the previous section it was shown that a perfect zero/pole cancellation occurs when the velocity compensation is performed. This cancellation permits to improve significantly the performance of the system, as seen in Fig. 5.5. Now, the velocity compensation for the load force dynamics is presented.

Unlike the hydraulic force, the load force has not only one but two feedback points in the system, as clearly shown in Fig. 4.5. Thus, to completely eliminate the load velocity influence from the load force dynamics, both paths must be compensated for.

The compensation of the path where the velocity is fed back through the gain $A_{e\oslash}$ can be done similarly to the compensation performed in the previous section for the hydraulic force. By choosing the same control effort u_{vc} shown in Eq. 5.6 this path is eliminated also in the load force dynamics. However, an additional control effort has to be supplied to compensate for the losses due to friction. Thus, the final control effort u_{vc} that fully compensates for the load velocity can be written as:

$$u_{vc} = \frac{(A_{e\oslash} - BK_{ce})\Delta\dot{x}_p}{K_{qe}} + \frac{B\Delta\ddot{x}_p}{K_{qe}K_{th\oslash}} \tag{5.7}$$

As noticed, to eliminate the load motion from the load force dynamics requires also the piston acceleration $\Delta\ddot{x}_p$. Since the acquisition of this quantity in practice is generally through double numerical differentiation, it might be too noisy to be used. Thus, an approximation of the u_{vc} shown Eq. 5.7 could neglect the acceleration-dependent term. The effect of neglecting this term is presented in Fig. 5.6. As seen, to neglect this term does not influence significantly the velocity-compensated system response. Also, comparing the load force response in Fig. 5.6 with the hydraulic force response in Fig. 5.5, it can be seen that the non-compensated response (black line) does not converge to the reference in the load force case due to the low damping in the load.

In terms of transfer function, the simplified load velocity compensation (i.e., neglecting the acceleration term) does not cancel the zero with a pole in the load force transfer function shown in Eq. 4.13. However, even though the low-frequency zero remains, the two complex conjugated poles from the hydraulic dynamics become real. Therefore, it becomes possible to further increase the closed-loop gain and consequently the system performance.

To demonstrate the effectiveness of the velocity compensation approach in practical force control applications, an experiment has been performed with the HFE joint of the HyQ leg. A 10 kg weight was fixed to the end-effector to permit a reasonable torque step magnitude. As seen in Fig. 5.7, the experimental results are
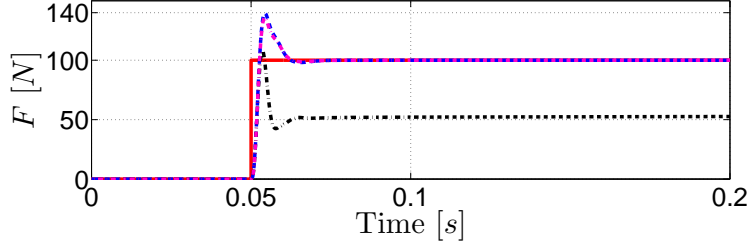
Figure 5.6: Simulation of the load force step response. The red solid line depicts the load force reference, the blue dashed shows the response with the full velocity compensation, the pink dashed neglects the acceleration term in the velocity compensation, and the black dot-dashed shows the response with no velocity compensation. As seen, neglecting the acceleration term does not cause big impacts in the system response.

coherent with the simulation results presented before. The compensated response has a settling time that is more than *three times faster* (about 0.25 s) than the non-compensated one (0.8 s).
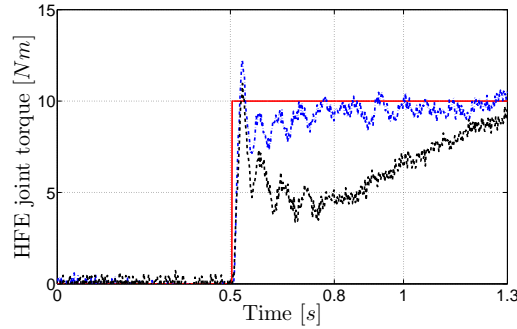
Figure 5.7: Response to a step torque reference for the hydraulic hip joint HFE: in dashed black the non-compensated response, and in dot-dashed blue the compensated one. The velocity compensation makes the system about 3 times faster.

In the previous experiment, the load force was being controlled. However, as seen in Fig. 5.7, the experimental non-compensated load force response, depicted through the dashed black line, is more similar to the simulation results of the hydraulic force (Fig. 5.5) than the ones from the load force (Fig. 5.6). The reason for this mismatch is simple: during the experiment, there was a significant counter-force due to gravity. The gravitational force created a load that permitted the non-compensated response to reach the reference after some time. In the simulation results for the load force presented in Fig. 5.6, a simple inertial load moving in a low-friction plane was considered and the effects of gravity were neglected. Thus,

in this case no significant counter forces are created, and as a consequence the non-compensated load force cannot increase its magnitude. It is important to underline that *the non-compensated response raises proportionally to the forces that oppose the motion.* In the simulation of the hydraulic force shown in Fig. 5.5, the counter force which enables the non-compensated response to reach the reference is the cylinder viscous friction.

Details about the velocity compensation of electric actuators, as well as experimental results, can be found in [Boaventura et al., 2012a].

5.2.3   Force feedback linearization

The hydraulic flow dynamics (Eq. 3.9 and 3.10) is nonlinear, and thus also the hydraulic force dynamics is nonlinear. Since analysis and control design are far easier for linear than for nonlinear models, a linearization is usually performed.

Traditional linearization procedures find a linear model that approximates a nonlinear model in the neighborhood of an equilibrium point. Therefore, a controller based on this linear model behaves as designed only close to the equilibrium point. However, it is desirable that the controller performance indexes, such as rising time and overshoot, are satisfied for the whole range of operation of the nonlinear system and not only in proximity of the equilibrium point.

To overcome this issue, this section introduces the *input-output feedback linearization* approach [Slotine and Li, 1991]. In this approach, state feedback is used to linearize the relation between the control input and the controlled variable within the whole range of operation of the system.

Feedback linearization is a model-based control approach, so the better the model the better the linearization and also the controller performance. Because of that, a proper identification of the parameters is very important for obtaining the expected results.

The approach described in this section does not follow the traditional feedback linearization approach design, which uses Lie derivatives. This traditional method, which is more methodical and complicated, is shown in Appendix B and is equivalent to the approach presented in this section.

The approach used in here uses the load force model shown in Chapter 3. The nonlinear force dynamics, represented by Eq. 3.20, can be rewritten in a more convenient way to perform the feedback linearization:

$$\dot{f} = f(x_p, \dot{x}_p, \ddot{x}_p) + g(P, x_p)u_v \tag{5.8}$$

where $f(x_p, \dot{x}_p, \ddot{x}_p)$ is a function that depends on the cylinder position x_p, velocity $\dot{x}_p$, and acceleration $\ddot{x}_p$. It groups all the terms that do not depend on the control input u_v. The function $g(P, x_p)$ depends on the cylinder position x_p and on the system pressures $P = \{p_a, p_b, p_s, p_t\}$. This function groups all the terms of the force dynamics that multiply u_v. These two functions can be defined as:

$$f(x_p, \dot{x}_p, \ddot{x}_p) = \beta_e A_p^2 \left(\frac{1}{v_a} + \frac{\alpha^2}{v_b} \right) \dot{x}_p - B\ddot{x}_p \tag{5.9}$$

$$g(P, x_p) = \begin{cases} \beta_e A_p K_v \left(\frac{\sqrt{p_s - p_a}}{v_a} + \frac{\alpha\sqrt{p_b - p_t}}{v_b} \right), & u_v > 0. \\ \beta_e A_p K_v \left(\frac{\sqrt{p_a - p_t}}{v_a} + \frac{\alpha\sqrt{p_s - p_b}}{v_b} \right), & u_v < 0. \end{cases} \tag{5.10}$$

Since Eq. 5.8 defines already a direct analytical relation between the valve input u_v and the load force output f, a feedback linearization can be easily performed. Neglecting the valve dynamics, a valve control input u_{FL} can be set in the following form to linearize the system for all configurations:

$$u_{FL} = \frac{1}{g(P, x_p)} \left(v - f(x_p, \dot{x}_p, \ddot{x}_p) \right) \tag{5.11}$$

As seen in Eq. 5.9, the function $f(x_p, \dot{x}_p, \ddot{x}_p)$ contains terms dependent on the piston velocity $\dot{x}_p$ and acceleration $\ddot{x}_p$. When inserted in the control input u_{FL}, this function $f(x_p, \dot{x}_p, \ddot{x}_p)$ plays the role of compensating for the load velocity influence in the force dynamics. The contribution of this function in the composition of the final control signal u_{FL} can be seen as a nonlinear equivalent of the linear velocity compensation input u_{vc} shown in Eq. 5.7. If on one hand $f(x_p, \dot{x}_p, \ddot{x}_p)$ compensates for the load velocity influence, the function $g(P, x_p)$, on the other hand, aims to compensate for the pressure dynamics nonlinearities. These two functions together are able to give a linear force response that does not depend on the load dynamics.

By applying the control input u_{FL} described in Eq. 5.11 to the system in Eq. 5.8, the load force dynamics becomes $\dot{f} = v$. Choosing v as a PI controller with

an additional feed forward term corresponding to the time derivative of the force reference, the following linear dynamics is obtained:

$$\dot{f} \;=\; v \;=\; \dot{f}_{ref} - K_p\left(f_{ref} - f\right) - K_i \int \left(f_{ref} - f\right) dt \qquad (5.12)$$

Then, solving the following ordinary differential equation for the linearized force error dynamics shown in Eq. 5.13, the gains K_p and K_i can be easily designed to satisfy the system requirements such as rise time and overshoot.

$$\dot{e}_f - K_p e_f + K_i \int e_f \, dt = 0 \qquad (5.13)$$

where,

e_f: load force tracking error $(e_f = f_{ref} - f)$ $[N]$
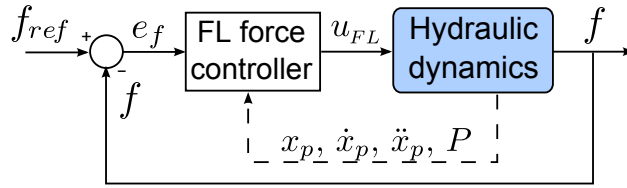
Figure 5.8: Block diagram of the feedback linearization control approach. The feedback linearization is a model-based controller which feeds back the piston position x_p, velocity $\dot{x}_p$, and acceleration $\ddot{x}_p$ to calculate the valve input u_{FL}. This control approach compensates for both the load velocity influence and the nonlinearities of the pressure dynamics.

The implementation of the feedback linearization controller in the real hardware was not straightforward. Firstly, HyQ does not have pressure sensors for measuring the chamber pressures p_a and p_b of the actuators. HyQ measures only p_s and p_b. Since the function $g(P, x_p)$ requires the chamber pressures, they were estimated using the load cell data and the friction model obtained in Section 3.4.2. Therefore, using Eq. 3.19, the hydraulic force and consequently the pressures could be estimated. In addition, to handle modeling errors and ensure stability, the gains K_{pc} and K_{vc} were introduced in the control law shown in Eq. 5.11:

$$u_{FL} = \frac{K_{pc}}{g(P, x_p)} \left(v - K_{vc}\, f(x_p, \dot{x}_p, \ddot{x}_p)\right) \qquad (5.14)$$

where,

K_{vc}: velocity compensation gain

K_{pc}: pressure compensation gain

To assess the performance of the feedback linearization controller, an experiment was performed with the leg from the HyL setup. A fast 5 Hz sinusoidal position reference was created for both HFE and KFE joints. A position loop, as described in Section 6.1.1, was used as outer loop. This outer loop created the force references to the force controllers. The results for the HFE joint are presented in Fig. 5.9. The solid red line represents the force reference, and the dashed black one the actual force. As seen, practically no amplitude and phase errors are present. This very satisfactory result ensures the high-performance that can be obtained with a feedback-linearization-based force controller using hydraulic actuators.
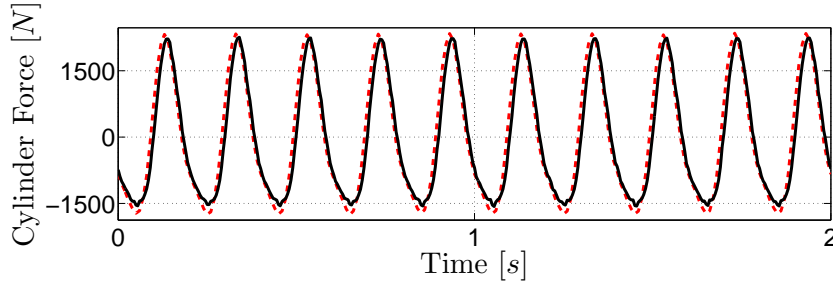
Figure 5.9: High-performance force tracking for the HFE joint: the dashed red line is the 5 Hz force reference, created by a sinusoidal motion, and the solid black line is the actual force created by the hydraulic cylinder.

Chapter 6

Active compliance

Physical contacts are inherent to robotics applications such as assembly, service duties, and legged locomotion. To properly handle these physical contacts, it is essential to be able to control the interaction forces, or more generally speaking, to control the robot's compliance.

Animals are constantly using muscle power for controlling their compliance. Legged animals, for instance, adapt their leg muscle stiffness according to the performed motion and terrain [Hoyt and Taylor, 1981]. The capability to change between different stiffness profiles permits to choose the most suitable compliance characteristic for a certain situation. Being able to mimic this adaptive capability is a big step towards truly versatile robots and the main motivation behind the use of active compliance in the HyQ robot.

This chapter introduces the compliance control scheme of the HyQ robot. It presents some approaches for implementing the compliance controller and also discusses about the main aspects that affect the stability of such controllers under physical contacts with the environment. It is demonstrated that the performance of the force controller also influences the stability of the compliance controller as a whole.

Before starting, an important remark: the term *compliance* has been used in robotics in the last decades in an ambiguous manner. In mechanics, compliance is an intrinsic characteristic of a material, and not of a structure. Its inverse is the *elastic modulus* of the material. The correct term, in the robotics case, should be *flexibility*, which is the inverse of the *stiffness* of a structure. Nevertheless, this

imprecise terminology is kept in this thesis for historical and clarity reasons. That is, *in this thesis the term compliance refers to the relation between the motion and forces generated at the contact point.* It includes both the stiffness and the damping of the structure, but not its inertia.

6.1 Compliance control

The HyQ compliance controller uses a cascade control architecture, as depicted in the block diagram of Fig. 6.1. It consists of an outer control loop that manipulates the reference input of an inner torque control loop. The inner torque loop can employ any of the force control approaches described in Chapter 5. The torque is transformed into force through a variable lever arm l_{la}. [Semini, 2010].
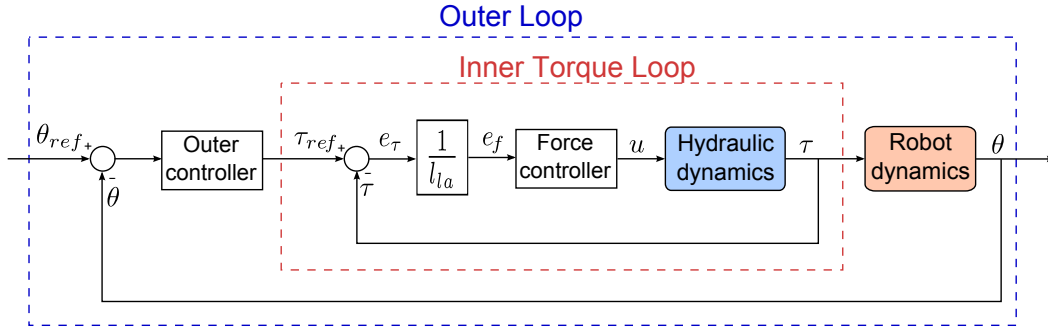
Figure 6.1: Block diagram for the cascade control. An outer loop creates the torque reference for the inner torque loop, which calculates the input u to the valve. The torque error e_τ is transformed into a force error e_f through a lever arm l_{la} that varies according to the leg position. Both outer and inner controllers can use state feedback from the hydraulic and robot dynamics in case a model-based controller is employed.

The high performance that can be obtained with the inner torque controller, described in Chapter 5, is essential for being able to successfully achieve compliance only through software, without any real spring on it [Boaventura et al., 2012b; Focchi et al., 2012].

Also, the existence of an inner high-fidelity joint-space torque controller permits to consider the robot joints as torque sources, a fact that simplifies considerably the implementation of advanced control approaches that have joint torques as output, such as rigid body inverse dynamics control, virtual model control, and impedance control. All these control approaches are investigated and presented in the next

sections as possible controllers for the outer loop of the HyQ cascade compliance control shown in Fig. 6.1.

6.1.1 *PD* joint-space position control + inverse dynamics

The easiest form of implementing a compliance controller is probably by closing a *PD* joint-space position loop. The integral term is not usually necessary because to have zero steady-state position error, in general, is not a *must* in a compliant system. Also, the PD control terms have physical counterparts that are directly related to the common intuition of compliance:

- Proportional term: it can be interpreted as a spring. It creates a control action that is proportional to the position error.

- Derivative term: it can be interpreted as a damper. It creates a control action proportional to the velocity error.

When the position controller is set in cascade with an inner torque controller, the output of the position controller τ_{ref} is necessarily a torque and has the unit Nm. In this case, the position proportional gain K_p has the unit Nm/rad, which corresponds to the units of a rotational spring, and the derivative gain $K_d\ Nms/rad$, which corresponds to a rotational damper. Having these units for the controller gains is a great advantage since the gains acquire a direct and simple physical meaning and their tuning becomes much more intuitive.

In the absence of an inner force loop, the output of the feedback controller τ_{ref} is directly an analog input to the actuator (e.g. voltage or current). Considering τ_{ref} is a voltage, K_p would have unit V/rad, while K_d would have unit Vs/rad. Even though these units do not have a clear physical meaning, the actuator would still behave as a more complex spring-damper, that is, it would still react proportionally to position and velocity errors. However, the tuning of such gains are not as intuitive as when an inner torque loop is present.

The method presented in here is a *single-input-single-output (SISO)* control approach. That is, each joint compliance is controlled individually, one at a time. Considering the HyQ control architecture shown in Fig. 6.1, the outer PD control law can be defined for a certain joint as:

$$\tau_{fb} = K_p(\theta_{ref} - \theta) + K_d(\dot{\theta}_{ref} - \dot{\theta}) \tag{6.1}$$

where,

τ_{fb}: output of the *feedback* position controller $[Nm]$

K_p: proportional gain $[Nm/rad]$

θ_{ref}: joint position reference $[rad]$

θ: current joint position $[rad]$

K_d: derivative gain $[Nms/rad]$

$\dot{\theta}_{ref}$: joint velocity reference $[rad/s]$

$\dot{\theta}$: current joint velocity $[rad/s]$

This PD controller is designed based on a linearized model of the robot dynamics. Thus, the parameters used in the design, such as overshoot and settling time, are valid only close to the equilibrium point of the linear model. In practice, it means that the position response is not always the same within the leg range of motion.

To close the position loop, an angle convention was employed. The angles for the left front leg of HyQ, which is identical to the one used in the HyL setup, are shown in Fig. 6.2. The angles definitions for the other HyQ legs are shown in [Semini, 2010].
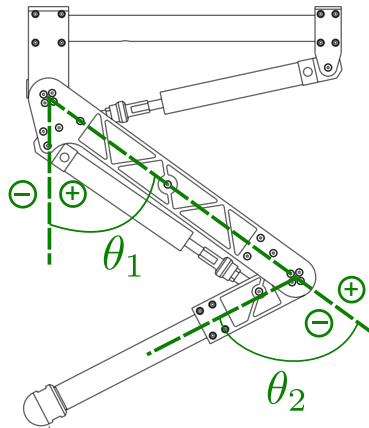
Figure 6.2: Angles conventions for the HyQ left front leg

Many of the robots built so far are typically controlled via traditional position control techniques. To guarantee that the robot follows satisfactorily the desired trajectories, the position controller gains have to be set as high as possible. The higher the position gains, the better the position tracking. These high position gains give a stiff characteristic to the robot since it would create a significant force for a small deviation from the desired position. However, this stiff behavior is inappropriate for interacting with the environment and/or people. The high forces created by a stiff robot when it hits an obstacle can injure people, damage the environment, or even break the robot.

The rigid body inverse dynamics, introduced in Section 5.1, is a model-based feature that permits to obtain *at the same time* good position tracking *and* a compliant behavior. It is possible because the inverse dynamics control, based on the robot rigid body model information, is able to predict the torques needed for performing some motion. If the model is accurate, the predicted torques would be sufficient for following the desired trajectory with small position errors. The better the model, the smaller the position errors. A perfect model would produce torques that would track perfectly the predefined trajectory even without a feedback position controller. Also, note that in Eq. 5.2, the inverse dynamics control signal does not depend on the position error. For instance, in case the robot hits an unmodeled and unperceived obstacle, the inverse dynamics does not increase the estimated torques in order to keep tracking the desired position.

All these characteristics of the inverse dynamics control become very useful when an inner torque loop is present. In this case, the predicted torques τ_{ff} can be easily added in the torque reference signal τ_{ref} as a *feed forward* control term, as shown in Fig. 6.4. It is important to note that $\boldsymbol{\tau_{ff}}$ in Eq. 5.2 is a vector, while in here τ_{ff} is one of the components of this vector, that is, a scalar.

$$\tau_{ref} \;=\; \tau_{ff} + \tau_{fb} \;=\; \tau_{ff} + K_p(\theta_{ref} - \theta) + K_d(\dot{\theta}_{ref} - \dot{\theta}) \qquad (6.2)$$

Thus, if the torque controller is precise and the rigid body model accurate, the robot would move as predicted and the position error would be small. Therefore, the contribution of the feedback control action τ_{fb}, which is based on the position error (Eq. 6.1), in the torque reference τ_{ref} (Eq. 6.2) would also be small during

the position tracking. Fig. 6.3 shows an experimental result with position and force tracking for a 5 Hz sine position reference for the HFE joint of the left front HyQ leg (first and second plot, respectively). This experiment was performed with the HyL setup, and the torque controller is based on the feedback linearization approach (Section 5.2.3). The third plot shows the two components τ_{fb} and τ_{ff} of the torque reference that goes to the torque controller. It can be seen that τ_{fb} is very small. This highlights the accuracy of the HyQ leg rigid body model and torque controller at high velocities.
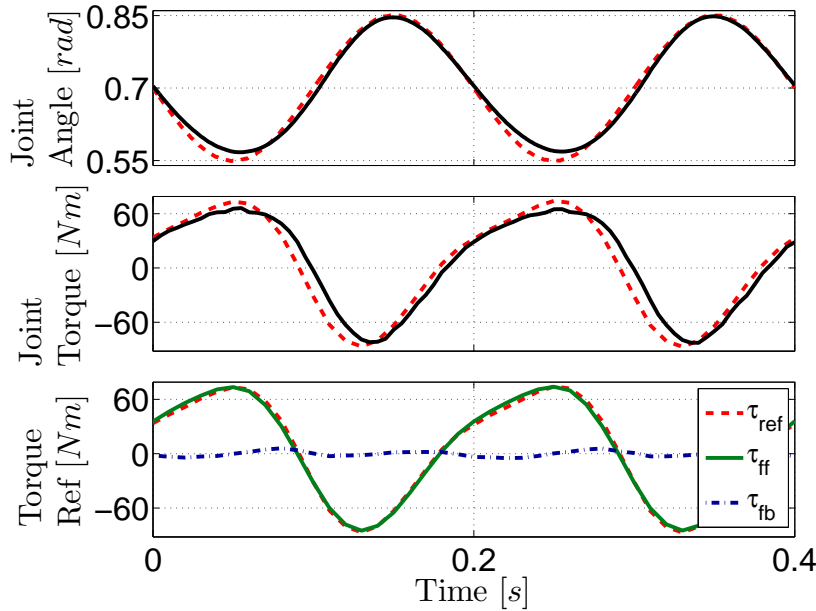
Figure 6.3: Precise position and force tracking for a 5 Hz sine position reference for the HFE joint. In the first two plots, the red dashed lines indicate the reference command and the black solid ones the actual value. The last plot shows that the reference torque τ_{ref} is generated as the sum of feed-forward and the position error feedback term: $\tau_{ref} = \tau_{ff} + \tau_{fb}$. The reference torque is almost completely obtained by the feed-forward term, indicating a very accurate rigid body dynamics model of the HyQ leg segments.

The fact that the feedback position control loses importance when the feed forward inverse dynamics control is used is a very important aspect in the compliance control. Since the feedback term becomes small, it is possible to reduce the position gains K_p and K_d with no significant losses in the position tracking capabilities. The reduction of these gains is the important aspect for the compliance control, since

these gains are directly related to the stiffness and damping of the robot joints. The smaller K_p the smaller the joint stiffness. And the smaller K_d the smaller the joint damping. Thus, with inverse dynamics control it becomes possible to set low stiffness and damping to the robot joints and keep a good position tracking *at the same time*. This is a very desirable behavior for robots that have to safely deal with human beings or with unstructured and partially unknown environments [Buchli et al., 2009].

The HyQ control architecture with the feedback *PD* joint-space position controller and the feed forward inverse dynamics control is shown in Fig. 6.4.
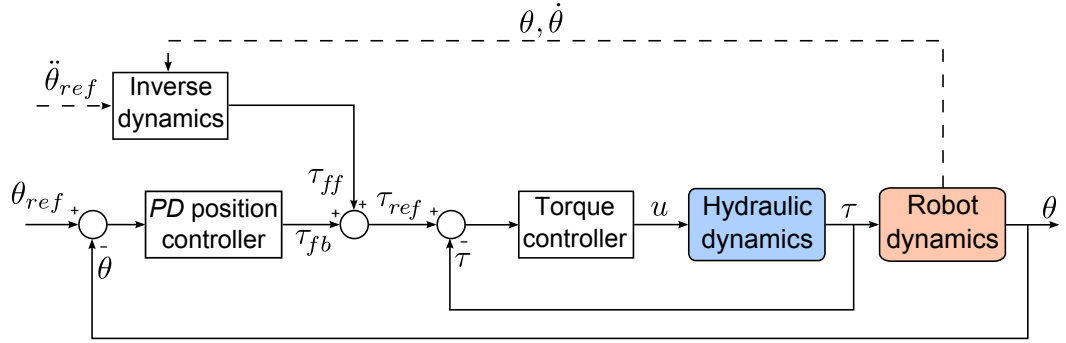
Figure 6.4: Block diagram for the HyQ cascade control with an outer feedback joint-space position loop. It creates, together with a feed forward term from the rigid body inverse dynamics, the torque reference τ_{ref} for the inner torque loop. For sake of simplicity, the lever arm l_{la} is not shown in the block diagram and the force controller is seen as a torque controller. The model-based inverse dynamics controller needs the feedback of the joint position θ and velocity $\dot{\theta}$, and also the reference acceleration $\ddot{\theta}_{ref}$ to calculate the feed forward command τ_{ff}.

Since the PD controller is a linear controller, its designed performance is satisfied only in proximity of the linearization point. To ensure the same position response within all the leg workspace, a nonlinear and more advanced control approach is proposed in the next section.

6.1.2 Position feedback linearization

The *PD* position control method described in the previous section is based on the traditional linearization procedure of finding a transfer function that represents the nonlinear system around an equilibrium point. However, this method does not

guarantee that the performance indexes used in the control design, such as rising time and overshoot, are satisfied in the whole range of motion of the HyQ legs.

To be able to obtain the same response characteristic in any leg configuration, a different control method is proposed in this section: the *input-output feedback linearization* [Slotine and Li, 1991]. This approach was already introduced in Section 5.2.3, where the load force dynamics was linearized. However, in here the feedback linearization consists of a *multiple-input-multiple-output (MIMO)* controller, and the nonlinear relation that is linearized is between the joint torques and joint accelerations.

The rigid body dynamics presented in Eq. 5.1 can be rewritten in a more convenient manner as follows:

$$\ddot{\boldsymbol{q}} = \boldsymbol{f}(\boldsymbol{q}, \dot{\boldsymbol{q}}) + \boldsymbol{G}(\boldsymbol{q})\boldsymbol{\tau} \tag{6.3}$$

where $\boldsymbol{f}(\boldsymbol{q}, \dot{\boldsymbol{q}}) = -\boldsymbol{M}(\boldsymbol{q})^{-1}\boldsymbol{h}(\boldsymbol{q}, \dot{\boldsymbol{q}})$ is a vector, and $\boldsymbol{G}(\boldsymbol{q}) = \boldsymbol{M}(\boldsymbol{q})^{-1}$ is a matrix.

With the position dynamics represented in the form of Eq. 6.3, the torque vector $\boldsymbol{\tau}$ which linearizes the system for all the positions is:

$$\boldsymbol{\tau} = \boldsymbol{G}(\boldsymbol{q})^{-1}\left(\boldsymbol{v} - \boldsymbol{f}(\boldsymbol{q}, \dot{\boldsymbol{q}})\right) \tag{6.4}$$

where $\boldsymbol{v}$ is a vector of linear functions defined as *PD* controllers with the addition of the term $\ddot{\boldsymbol{q}}_{\boldsymbol{ref}}$, that is:

$$\boldsymbol{v} = \ddot{\boldsymbol{q}}_{\boldsymbol{ref}} + \boldsymbol{K_p}(\boldsymbol{q}_{ref} - \boldsymbol{q}) + \boldsymbol{K_d}(\dot{\boldsymbol{q}}_{ref} - \dot{\boldsymbol{q}}) \tag{6.5}$$

where,

$\boldsymbol{K_p}$: diagonal matrix with proportional joint-space position gains

$\boldsymbol{K_d}$: diagonal matrix with derivative joint-space position gains

Then, inserting Eq. 6.5 into Eq. 6.4, and also considering the inverse dynamics torques $\boldsymbol{\tau_{ff}}$ defined in Eq. 5.2, the following control effort is obtained:

$$\boldsymbol{\tau} = \boldsymbol{\tau_{ff}} + \boldsymbol{M}(\boldsymbol{q})\left(\boldsymbol{K_p}(\boldsymbol{q}_{ref} - \boldsymbol{q}) + \boldsymbol{K_d}(\dot{\boldsymbol{q}}_{ref} - \dot{\boldsymbol{q}})\right) \tag{6.6}$$

As seen in Eq. 6.6, the output torques vector $\boldsymbol{\tau}$ has a very similar form to the output torque obtained with the SISO *PD + inverse dynamics* approach presented in Eq. 6.2. However, despite being a MIMO approach, this new feedback linearization controller has another significant difference in comparison to its SISO fashion: it multiplies the PD output vector by the variable leg inertia matrix $\boldsymbol{M}(\boldsymbol{q})$.

The multiplication by $\boldsymbol{M}(\boldsymbol{q})$ implements the very intuitive concept that the heavier the link the more torque it requires for performing a certain motion. Furthermore, since the leg inertia $\boldsymbol{M}(\boldsymbol{q})$ changes according to the leg configuration, the influence of the PD gains in the output torques $\boldsymbol{\tau}$ is also position-dependent. Thus, this *a priori* knowledge about the link inertias can be used to scale the torques accordingly.

In addition, the inertia matrix $\boldsymbol{M}(\boldsymbol{q})$ is not diagonal for the HyQ leg. The non-diagonal elements express the interaction that exists between the links. They determine the torques created at a certain joint due to the accelerations of the other links. Therefore, the multiplications by $\boldsymbol{M}(\boldsymbol{q})$ also ensures that the interaction torques created due to these accelerations do not affect the position tracking.

Finally, the torques $\boldsymbol{\tau}$ shown in Eq. 6.6 can be applied to the position dynamics shown in Eq. 6.3 to obtain the linear position error dynamics:

$$\ddot{\boldsymbol{e}}_{\boldsymbol{\theta}} + \boldsymbol{K_d}\dot{\boldsymbol{e}}_{\boldsymbol{\theta}} + \boldsymbol{K_p}\boldsymbol{e}_{\boldsymbol{\theta}} = \boldsymbol{0} \tag{6.7}$$

where,

$\boldsymbol{e}_{\boldsymbol{\theta}}$: vector of the joint-position errors

By solving the ordinary differential equation above, the gain matrices $\boldsymbol{K_p}$ and $\boldsymbol{K_d}$ can easily be calculated to satisfy a certain desired error dynamics. In case the requirements are the same for all joints, these gain matrices can become simple scalars K_p and K_d.

6.1.3 Virtual Model Control

The most intuitive way of setting a desired compliance profile to a robot is probably through virtual model control [Pratt et al., 2001]. In this framework, virtual elements that have physical counterparts, for example mechanical spring, damper, and so on,
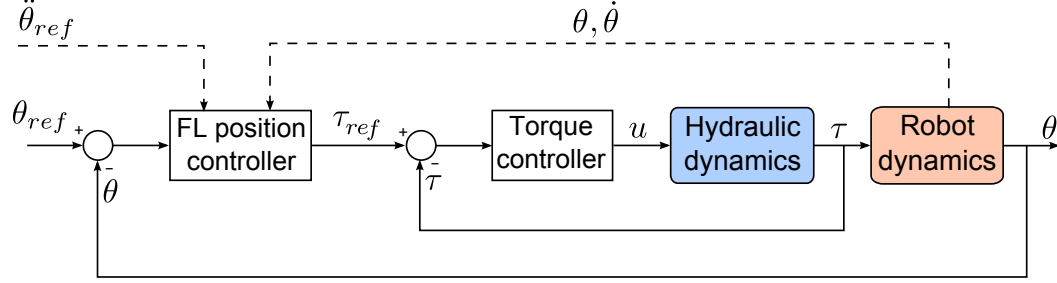
Figure 6.5: Block diagram for one joint showing the HyQ cascade control with an outer feedback linearization (*FL*) position loop. It is a model-based controller that feedbacks the joint position θ and velocity $\dot{\theta}$, and also gets the reference acceleration $\ddot{\theta}_{ref}$ to calculate the torque reference command τ_{ref}.

are placed at points of interest within the reference frames of the robot. Once the placement is done, it is possible to define a Jacobian matrix that relates the virtual component velocities to the joint velocities. Then, through the Jacobian transpose the interaction forces between these virtual components and the robot generate the desired joint torques $\boldsymbol{\tau_{ref}}$ to the actuators.

The cascade control architecture, shown in Fig. 6.1, is still used in here, with a virtual model controller employed as outer loop. As for all outer loop control approaches described so far, the effectiveness of this procedure is highly dependent on the inner torque tracking capabilities. Considering the closed-loop systems are stable, the higher the performance of the torque control the more realistic the virtual elements behavior.

In the virtual model approach, for making the HyQ robot actively-compliant a virtual linear spring-damper is used in between the HFE and the foot, as depicted Fig. 6.6. The desired force f_{vl} created by these virtual components can be defined as:

$$f_{vl} = K_{vl}\delta l_{vl} + B_{vl}\dot{l}_{vl} \tag{6.8}$$

where,

K_{vl}: virtual leg stiffness $[N/m]$

B_{vl}: virtual leg damping $[Ns/m]$

l_{vl}: virtual leg length $[m]$

The variation δl_{vl} of the virtual leg length is defined as $\delta l_{vl} = l_{vl_0} - l_{vl}$, where
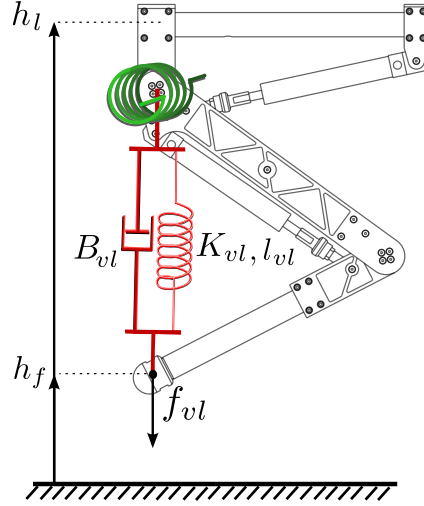
Figure 6.6: Virtual components implemented on the HyQ leg: a rotational spring-damper at the hip joint, and a linear spring-damper between the hip and the foot. The virtual leg damping is B_{vl}, the stiffness K_{vl}, and the virtual spring length l_{vl}. The force f_{vl} is created by these virtual components. The foot height is named h_f and the virtual leg height h_l.

l_{vl_0} is the initial (free) length of the virtual spring. The change ratio of the spring length is represented by $\dot{l}_{vl}$.

The desired force f_{vl} in Eq. 6.8, created by the virtual spring-damper, represents a control law that is equivalent to a position PD control in task-space, where the reference position is defined by the initial (free) length l_{vl_0} of the spring, and the reference end-effector velocity is always *zero*, with K_{vl} being the position gain and B_{vl} the velocity gain, both defined in the spring direction. An equivalent definition of the virtual characteristics can be done in Cartesian space (see Appendix C).

The control law for the hip joint is simpler, where its compliance is regulated only by a joint-space PD position control, as shown in Eq. 6.1. It can also be seen, using the virtual elements approach, as a rotational spring-damper. The hip joint control is important for moving the virtual prismatic leg, for instance during the flight phase of a hopping experiment, to a desired position. In this thesis, the hip compliance is not investigated and it is set constant, with $K_{hip} = 70~Nm/rad$ and $B_{hip} = 3~Nms/rad$.

Although in Eq. 6.8 a linear spring was used to create the force f_{vl}, other behaviors can be easily programed. For instance, a spring with an exponential stiffness

profile could be represented by the following virtual force f_{vl}:

$$f_{vl} = f_{vl_0} e^{K_{vl_e} \delta l_{vl}} \tag{6.9}$$

where,

    f_{vl_0}: virtual leg force at equilibrium (with no spring compression) $[N]$

    K_{vl_e}: exponential stiffness gain $[1/m]$

To demonstrate HyQ's ability to behave as virtual elements, a linear and an exponential spring were implemented. Both springs are placed at the same position, as depicted by the red elements in Fig. 6.6. For obtaining a force vs. displacement plot, the leg was manually pushed down to compress the virtual springs. As can be seen in Fig. 6.7, the tracking of such elements characteristics is very satisfactory. However, during these experiments the leg was not subject to high-frequency inputs, such as impacts. Results that include a damper to an exponential spring can be found in [Boaventura et al., 2011] and in Section 6.3.
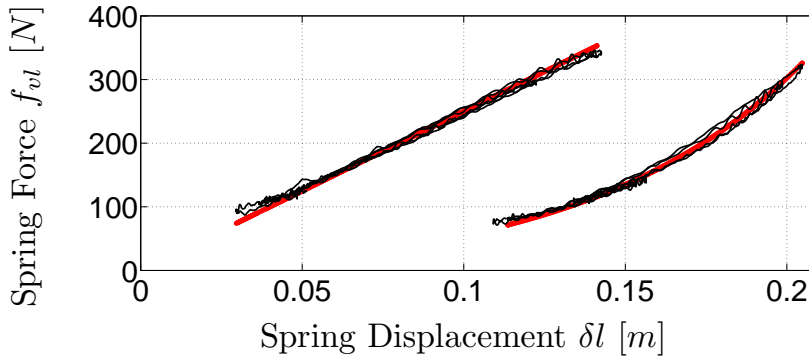
Figure 6.7: Two different virtual springs implemented on the real hardware: a linear one ($f_{vl} = 2500\,\delta l_{vl}$) and an exponential one ($f_{vl} = 16\,e^{15\,\delta l_{vl}}$). The red line in the back represents the desired stiffness profile, and the black line on top the spring characteristics created by the HyQ leg.

The use of the virtual linear leg is a simple way of actively implementing the well-known spring loaded inverted pendulum (SLIP) model [Blickhan, 1989; Hutter et al., 2010], which is a useful abstraction that describes the spring-like behavior found in human and animal running. A mechanical way of achieving similar dynamics to the SLIP model is to design prismatic robotic legs [Raibert, 1986]. Although active

compliance can be reached through numerous ways, to bring the simple abstraction of the SLIP approach into the robot dynamics is another motivation to implement active compliance in the way presented in this section (i.e. using virtual elements).

How to choose the most suitable virtual leg stiffness and damping is still not clear. It might depend on the terrain characteristics as well as on the tasks (e.g. walking, running, trotting). This topic must be investigated to improve the performance of legged robots in general, and it is listed in the *Future Works* in Section 8.1.

6.1.4 Impedance control

Impedance control is a suitable framework to control robots in contact with unknown environments, as for example legged locomotion over rough terrains. A well established framework for impedance control was introduced by Hogan [Hogan, 1985c]. In [Albu-Schäffer and Hirzinger, 2002] an overview of different controller architectures (impedance together with admittance control and stiffness control) is given.

The underlying idea of impedance control is to properly design the disturbance response when a deviation from the prescribed motion occurs. It is possible to define a desired impedance to any point of the robot, given a kinematic transformation between this point and the actuated joint variables exists. The most common point used to implement the impedance control is the robot end-effector, which is the part that is normally in contact with the environment and/or other objects. However, other points such as the robot CoG can also be used to give a desired dynamical characteristic to the system [Sentis and Khatib, 2006].

In this section, an end-effector Cartesian impedance controller for the HyQ robot leg is described [Focchi et al., 2012]. The main goal is to define a dynamic relationship between the end-effector position vector $\boldsymbol{x_{ee}} = \{x, y, z\}$ (i.e. the foot of the robot) and the Cartesian forces vector $\boldsymbol{f_{ext}} = \{f_x, f_y, f_z\}$. The torque components in the force vector $\boldsymbol{f_{ext}}$ are not considered in here.

A common choice for the impedance behavior is a dynamical system of second order as follows:

$$\boldsymbol{f_{ext}} = \boldsymbol{K_{ee}}(\boldsymbol{x_{ee_d}} - \boldsymbol{x_{ee}}) + \boldsymbol{B_{ee}}(\boldsymbol{\dot{x}_{ee_d}} - \boldsymbol{\dot{x}_{ee}}) + \boldsymbol{M_{ee}}\boldsymbol{\ddot{x}_{ee}} \qquad (6.10)$$

where,

f_{ext}: end-effector reaction forces vector $[N]$

x_{ee}: end-effector position vector $[m]$

x_{ee_d}: end-effector desired position vector $[m]$

$\dot{x}_{ee}$: end-effector velocity vector $[m/s]$

$\dot{x}_{ee_d}$: end-effector desired velocity vector $[m/s]$

$\ddot{x}_{ee}$: end-effector acceleration vector $[m/s^2]$

K_{ee}: end-effector desired stiffness matrix $[N/m]$

B_{ee}: end-effector desired damping matrix $[Ns/m]$

M_{ee}: end-effector desired inertia matrix $[kg]$

For the HyQ leg, since it has 3 DOF and the foot orientation is not being controlled, the matrices K_{ee}, B_{ee}, and M_{ee} have dimension 3×3.

To implement the target behavior defined in Eq. 6.10, the desired end-effector impedance is expressed in joint-space, then a model of the manipulator dynamics is used to derive the required controller equations [Hogan, 1985c] as follows.

The desired behavior expressed in Eq. 6.10 can be rearranged into a specification of the desired end-effector acceleration due to an external force f_{ext} applied to it:

$$\ddot{x}_{ee} = M_{ee}^{-1} \left[K_{ee}(x_{ee} - x_{ee_d}) + B_{ee}(\dot{x}_{ee} - \dot{x}_{ee_d}) + f_{ext} \right] \qquad (6.11)$$

To find the joint torques that produce the specified end-effector acceleration $\ddot{x}_{ee}$ above, the following well-known joint-space dynamics relationships are used [Sciavicco and Siciliano, 2001]:

$$\begin{aligned} \dot{x}_{ee} &= J(q)\dot{q} \\ \ddot{x}_{ee} &= J(q)\ddot{q} + \dot{J}(q)\dot{q} \\ \ddot{q} &= J(q)^{-1} \left(\ddot{x}_{ee} - \dot{J}(q)\dot{q} \right) \end{aligned} \qquad (6.12)$$

Then, by plugging Eq. 6.11 into the last equation in Eq. 6.12, the joint accelerations $\ddot{q}_{ref}$ needed to satisfy the desired impedance in the Cartesian space can be obtained:

$$\ddot{\boldsymbol{q}}_{ref} = \boldsymbol{J}(\boldsymbol{q})^{-1} \left(\boldsymbol{M_{ee}}^{-1} \left[\boldsymbol{K_{ee}}(\boldsymbol{x_{ee}} - \boldsymbol{x_{ee_d}}) + \boldsymbol{B_{ee}}(\dot{\boldsymbol{x}}_{ee} - \dot{\boldsymbol{x}}_{ee_d}) + \boldsymbol{f_{ext}} \right] - \dot{\boldsymbol{J}}(\boldsymbol{q})\dot{\boldsymbol{q}} \right)$$
(6.13)

Considering the desired joint acceleration above and the leg rigid body dynamics described in Eq. 5.1, the torques that produce the desired dynamics to the end-effector can be finally expressed as [Hogan, 1985c]:

$$\boldsymbol{\tau_{ref}} = \boldsymbol{M}(\boldsymbol{q})\boldsymbol{J}(\boldsymbol{q})^{-1} \left\{ \boldsymbol{M_{ee}}^{-1} \left[\boldsymbol{K_{ee}}(\boldsymbol{x_{ee}} - \boldsymbol{x_{ee_d}}) + \boldsymbol{B_{ee}}(\dot{\boldsymbol{x}}_{ee} - \dot{\boldsymbol{x}}_{ee_d}) + \boldsymbol{f_{ext}} \right] - \right.$$
$$\left. - \dot{\boldsymbol{J}}(\boldsymbol{q})\dot{\boldsymbol{q}} \right\} + \boldsymbol{h}(\boldsymbol{q}, \dot{\boldsymbol{q}}) + \boldsymbol{J}(\boldsymbol{q})^T \boldsymbol{f_{ext}}$$
(6.14)

It is important to underline that the matrix $\boldsymbol{M}(\boldsymbol{q})$ and the vector $\boldsymbol{h}(\boldsymbol{q}, \dot{\boldsymbol{q}})$ depend on the joint configuration, while $\boldsymbol{M_{ee}}$, $\boldsymbol{B_{ee}}$, and $\boldsymbol{K_{ee}}$ are constant desired values for the end-effector dynamics.

From Eq. 6.14 it can be seen that the dynamics of the robot and of the end-effector are strongly coupled. Desired passive impedance can be chosen by having $\boldsymbol{M_{ee}}$, $\boldsymbol{B_{ee}}$, and $\boldsymbol{K_{ee}}$ as symmetric, positive definite matrices. It is possible to choose the directions in which to set the maximum/minimum stiffness, damping, and inertia by selecting the eigenvectors of these matrices. For a diagonal matrix, the impedance is set along the directions of the end-effector coordinate frame. More details about the implementation of the impedance controller on the HyQ leg can be found in [Focchi et al., 2012].

The impedance control law shown in Eq. 6.14 can be simplified in case a change in the end-effector inertia is not required. Also, if the gravity and Coriolis/centripetal forces do not need to be compensated for, the impedance controller would create only a virtual spring-damper at the end-effector space which attaches the end-effector to its desired trajectory. The advantage of this approach is that it does not require a measurement of the interaction forces at the end-effector. Thus, since the design of a 3-axis foot sensor is still part of an ongoing work, this simpler approach is the one implemented in the HyQ leg. The implementation of the full impedance controller (Eq. 6.14) is part of the *Future Works* in Section 8.1.

The idea of this simpler approach is that, whenever an external disturbance creates a deflection of the actual end-effector position $\boldsymbol{x_{ee}}$ with respect to the desired equilibrium point $\boldsymbol{x_{ee_d}}$, the leg creates forces $\boldsymbol{f_{ext}}$ in the Cartesian space that are a function of this deflection:

$$\boldsymbol{f_{ext}} = \boldsymbol{K_{ee}}(\boldsymbol{x_{ee_d}} - \boldsymbol{x_{ee}}) + \boldsymbol{B_{ee}}(\boldsymbol{\dot{x}_{ee_d}} - \boldsymbol{\dot{x}_{ee}}) \tag{6.15}$$

Again, the joint torques that create this end-effector force $\boldsymbol{f_{ext}}$ can be found through the end-effector Jacobian transpose matrix:

$$\boldsymbol{\tau_{ref}} = \boldsymbol{J(q)}^T \left[\boldsymbol{K_{ee}}(\boldsymbol{x_{ee_d}} - \boldsymbol{x_{ee}}) + \boldsymbol{B_{ee}}(\boldsymbol{\dot{x}_{ee_d}} - \boldsymbol{\dot{x}_{ee}}) \right] \tag{6.16}$$

All the Cartesian forces $\boldsymbol{f_{ext}}$ can be mapped into the joint space with the Jacobian transpose. It is important to remark that, even if Eq. 6.15 and Eq. 6.10 require the inverse or the transpose Jacobian, they do not require inversion of the kinematics equations. Only forward kinematic equations need to be computed. Therefore, this approach can be easily extended to a manipulator with kinematic redundancies for which no closed form solution of the inverse kinematic equations exists [Hogan, 1985c].

Furthermore, this framework can be extended to any point of the robot (e.g. the CoG) following the same recipe and using as Jacobian the one that defines the movement of that point with respect to the joint variables.

The control law in Eq. 6.15 is very similar to the virtual model one shown in Eq. 6.8. The difference between both approaches is fundamentally the definition of the stiffness and damping values. As shown in Appendix C, the virtual leg stiffness and damping can also be written in the end-effector coordinate frame. In this frame, the virtual leg stiffness and damping are not constant anymore and depend on the leg configuration. On the other hand, the stiffness and damping in this simple impedance control approach are constant in the end-effector space. However, generally speaking, both methods consist of a PD controller in task-space. It is only the definition of task-space that changes.

6.2 Passivity of an actively-compliant system

It is well-known that a strictly passive system, connected to any passive environment, is necessarily stable [Colgate and Hogan, 1989]. Thus, since most terrain surfaces are passive, to ensure a stable contact with the environment also the robot leg has to be passive. In this section, the main factors that influence the actively-compliant leg passivity are analyzed, such as filtering, sampling time, and torque controller gains.

When compliance is reached by assembling a real physical spring or damper onto the leg, it is certain that this component is intrinsically passive. In other words, it cannot provide additional energy to the system. However, when compliance is obtained actively, the compliant behavior is emulated by a controlled actuator, which can inject energy into the system and lead to instability.
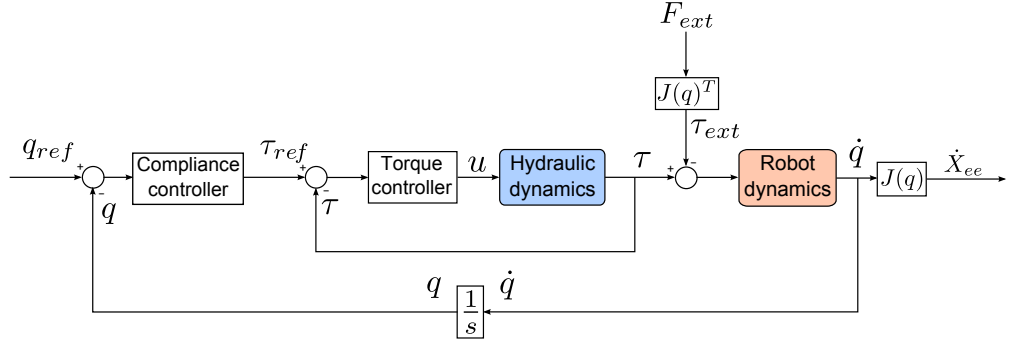
Figure 6.8: Block diagram of the HyQ control architecture for the MIMO case (all variables are vectors or matrices). The external force vector $\boldsymbol{f_{ext}}$, which is translated to joint-space through the end-effector Jacobian matrix $\boldsymbol{J(q)}$, acts as a perturbation into the system. The end-effector admittance matrix $\boldsymbol{Y}$ relates the the external forces $\boldsymbol{f_{ext}}$ with the end-effector velocities $\boldsymbol{\dot{x}_{ee}}$.

The mechanical driving-point impedance (denoted Z) is defined as the dynamic operator that determines an output force as a function of time from an input velocity as a function of time at the interaction port. The admittance Y, in the other hand, is defined as the inverse of the impedance Z, that is, it determines the output velocity given an input force [Kurfess, 2004]. For a MIMO system, as the HyQ leg, the admittance $\boldsymbol{Y(s)}$ is a matrix which groups individual admittance transfer functions. It can be defined as:

$$\dot{\boldsymbol{X}}_{\boldsymbol{ee}} = \boldsymbol{Y}(\boldsymbol{s}) \ \boldsymbol{F}_{\boldsymbol{ext}}(\boldsymbol{s}) \ \Leftrightarrow \begin{bmatrix} \dot{X}_{ee_x} \\ \dot{X}_{ee_z} \end{bmatrix} = \begin{bmatrix} Y_{xx}(s) \ Y_{xz}(s) \\ Y_{zx}(s) \ Y_{zz}(s) \end{bmatrix} \begin{bmatrix} F_{ext_x}(s) \\ F_{ext_z}(s) \end{bmatrix} \tag{6.17}$$

where,

$\boldsymbol{F}_{\boldsymbol{ext}}(\boldsymbol{s})$: external forces vector applied at the end-effector $[N]$

$F_{ext_x}(s)$: external forces applied in the *x direction* at the end-effector $[N]$

$F_{ext_z}(s)$: external forces applied in the *z direction* at the end-effector $[N]$

$\dot{\boldsymbol{X}}_{\boldsymbol{ee}}$: velocity vector at the end-effector $[m/s]$

$\dot{X}_{ee_x}$: velocity in the *x direction* at the end-effector $[m/s]$

$\dot{X}_{ee_z}$: velocity in the *z direction* at the end-effector $[m/s]$

The Cartesian directions x and z for the HyQ leg are defined in Fig. C.1. The admittance transfer functions in $\boldsymbol{Y}(\boldsymbol{s})$ can be obtained through the block diagram shown in Fig. 6.8, which uses the end-effector Jacobian matrix $\boldsymbol{J}(\boldsymbol{q})$ and the dynamic relationships shown in Eq. 6.12.

Necessary and sufficient conditions for passivity of a linear time invariant multi-port system are well-known in the literature [Anderson and Vongpanitlerd, 1973]. Considering Eq. 6.17, $\boldsymbol{Y}(\boldsymbol{s})$ is passive if and only if:

1. $\boldsymbol{Y}(\boldsymbol{s})$ has no poles in right-half plane $\Re(s) > 0$;

2. $\boldsymbol{Y}(\boldsymbol{s}) + \boldsymbol{Y}^*(\boldsymbol{s})$ is positive semi-definite in $\Re(s) > 0$;

where $\boldsymbol{Y}^*(\boldsymbol{s})$ is the conjugate transpose of $\boldsymbol{Y}(\boldsymbol{s})$.

When $\boldsymbol{Y}(\boldsymbol{s})$ has no poles in $\Re(s) \geq 0$, then condition 2 can be simplified to:

2a. The matrix $\boldsymbol{Y}(\boldsymbol{j\omega}) + \boldsymbol{Y}^*(\boldsymbol{j\omega})$ is positive semi-definite for all real ω.

In this case, it is possible to evaluate condition $2a$ by computing the minimum eigenvalue of $\boldsymbol{Y}(\boldsymbol{j\omega}) + \boldsymbol{Y}^*(\boldsymbol{j\omega})$ as a function of ω, and by checking that this is not negative.

For sampled data control systems, [Colgate, 1994] has suggested an approximate method based on computing the corresponding discrete time transfer function matrix $\boldsymbol{Y}(\boldsymbol{z})$, assuming that the port of interaction is also sampled. The phase of all the

entries in $\boldsymbol{Y}(\boldsymbol{z})$ is computed and corrected by adding $\omega T_s/2 \ rad$ to each term, where T_s is the sampling time interval. After this correction, the modified matrix and its transpose conjugate are added and the smallest eigenvalue computed. To guarantee passivity, this eigenvalue cannot be negative and $\boldsymbol{Y}(\boldsymbol{z})$ should not have poles outside the unit circle.

6.2.1 The Z-width

A legged robot is always interacting with the environment. Every time the robot's feet touch the ground, it is important to ensure this interaction is stable. To guarantee this stability the leg foot must be passive. Since the compliance at the foot is actively-controlled, the foot passivity depends on both position and torque controller gains.

The range of position gains that keep the leg passive is called Z-width [Colgate and Brown, 1994]. In other words, Z-width is the range of achievable virtual impedances, and it defines the combinations of stiffness and damping that can be passively rendered by a certain mechanism. The Z-width for virtual environments has been extensively investigated for haptics devices [Colgate and Schenkel, 1997; Janabi-Sharifi et al., 2000]. These devices are in general very simple and composed of only one DOF. Also, usually they do not perform any kind of force/torque control, but only position control. Therefore, some of the results present in the literature might not be applicable to more complex systems with different control architectures and multiple DOF. In addition, to the best of the authors' knowledge, the concept of Z-width has never been investigated for legged systems. The main reason for the absence of studies about the Z-width in this field is, most likely, the lack of actively-compliant legged robots.

The results obtained in [Colgate and Schenkel, 1997] suggest that the intrinsic system capability of dissipating energy, represented by the viscous friction, is the most important parameter for determining the size of the Z-width. Practically, the bigger the friction the bigger the range of achievable passive impedances. In other words, one should not inject more energy than the system can naturally dissipate.

In this perspective, the high friction of hydraulic actuators becomes an advantage since it increases their natural Z-width, although it is energetically inefficient. In

[Weir et al., 2008], for instance, friction is intentionally added to an electrically-actuated haptic device through a physical damper in order to artificially increase the Z-width.

Other factors, such as the sampling time and velocity filtering, have also been analyzed [Janabi-Sharifi et al., 2000]. All these studies were done for a single DOF system. In this thesis, this analysis is extended for considering a multi-DOF system, such as the HyQ leg.

6.2.2 Torque control & Z-width

Although many studies have been carried out for analyzing the passivity of sampled-data systems, there is still a lack of information about the influence of the closed-loop torque control bandwidth in the Z-width. Previous researches did no address nested control loops, and only the position signal used to be fed back [Colgate and Schenkel, 1997]. Hence, there is no information in the literature about how the torque loop performance and the actuator dynamics affect the passivity of an actively-compliant system that uses a cascade control approach as the one depicted in Fig. 6.8. Therefore, this section clarifies the importance of the torque loop in the HyQ leg passivity and shows that also the actuator bandwidth plays an important role in the Z-width. The results presented in here can be applied also to other systems besides legged robots.

The following analysis is based on a linearized model of the HyQ left-front leg. The hydraulic actuation is linearized as presented in Section 3.5, with operating point $P_\oslash = (p_{a\oslash}, p_{b\oslash}, u_{v\oslash}) = (\frac{\alpha p_s}{1+\alpha}, \frac{p_s}{1+\alpha}, 0)$. The leg angles used in the rigid body linearization are $\theta_{1\oslash} = 0.73 \ rad$ for the hip joint and $\theta_{2\oslash} = -1.5 \ rad$ for the knee.

To analyze the leg passivity at the end-effector, the hip impedance is set constant ($K_{hip} = 70 \ Nm/rad$ and $B_{hip} = 3 \ Nms/rad$). For the virtual leg, a sufficiently large range was chosen based on the values that are currently used both in simulations and experiments: the virtual leg stiffness K_{vl} ranging from 1 up to 20000 N/m and the damping B_{vl} from 1 up to 1600 Ns/m. Then, the passivity is checked by performing the criteria described at the beginning of Section 6.2 for every possible combination of K_{vl} and B_{vl}.

The control approaches chosen for this analysis were the *velocity compensation for the inner torque loop*, as described in Section 5.2.2, and the *virtual model control*

for the outer loop. In addition, the effect of gravity has been ignored. It is assumed that there is a separated gravity compensation scheme that counteracts the effects of gravity. Moreover, the sampling time was set as $T_s = 0.001 \ s$ and the digital inner PI torque controllers for both joints are identical and defined as:

$$C_{pi} = K_{PI} \frac{0.03838 \, (z - 0.9953)}{z - 1} \tag{6.18}$$

This controller provides the largest bandwidth possible for the torque loop with gain margins that guarantee a non-oscillatory response. Degradations in the response start with the hip gain $K_{PI} = 3.5$, where response is still stable but highly oscillatory, while for the knee this value is $K_{PI} = 3.0$.

Usually, the torque loop is set to be as fast as possible within the stability limits. The higher the torque control bandwidth the closer the joints are to a perfect torque source. However, depending on the actuation system and control, the torque bandwidth limit can vary. The closed-loop torque bandwidth can vary, for instance, by changing the controller gains and also by changing the actuator dynamics, as further discussed in this section.

The first set of analyses looks at the impact of the controller gains in the system passivity. In particular, the gain K_{PI} shown in Eq. 6.18 is the gain that is going to change. The effects of varying the location of the controller zero were not investigated. Changes on the K_{PI} gain of the *knee* PI torque controller have the most prominent impact on stability and passivity of the virtual leg. With $K_{PI} = 1$, the maximum damping which still keeps the system passive is about $B_{vl} = 1300 \ Ns/m$ (Fig. 6.9b). Setting $K_{PI} = 2$ constrained the passivity region to a maximum damping of $B_{vl} = 400 \ Ns/m$ (Fig. 6.9a), while setting $K_{PI} = 0.5$ enlarged the passivity region to fully covering all the chosen range of values for the virtual parameters (Fig. 6.9c).

The passivity results shown in Fig. 6.9 were obtained using the criteria described at the beginning of Section 6.2. Essentially, they show for which combination of stiffness and damping the system matrix $Y(z) + Y^*(Z)$ has a negative eigenvalue and/or $Y(z)$ is not stable, and thus not passive. The red areas represent those combinations where $Y(z)$ is unstable, that is, when it has a pole outside the unit circle. The blue regions show where all the eigenvalues are non-negative and $Y(z)$

is stable. Finally, the green area depicts where $\boldsymbol{Y}(\boldsymbol{z})$ is stable but not passive, that is, where at least one eigenvalue of the matrix $\boldsymbol{Y}(\boldsymbol{z}) + \boldsymbol{Y}^*(\boldsymbol{Z})$ is negative. These results show that the closed-loop torque gains have a big impact on the Z-width. For a given system, *the higher the torque loop gains, the smaller the range of impedances that can be passively rendered.*

Although a reduction of the torque PI controller gains increases the Z-width, it decreases the system capabilities in mimicking the virtual components. This topic is discussed in more details in the next section (Section 6.3). Therefore, in case a robot needs to enlarge its Z-width, to reduce the torque gains is not the best approach. In this case, an alternative to increase the Z-width is by changing the actuator. For valve-controlled hydraulic systems, as HyQ, it means to change the valve.

The second set of passivity analyses consists in assessing the influence of the actuator dynamics in the Z-width. The controller structure is still the same used in the previous analyses (i.e., velocity compensation for the inner torque loop and virtual model control for the outer loop). Three different valve bandwidths F_v (Eq. 3.3, where $\omega_v = 2\pi F_v$) were chosen: 50, 150, and 250 Hz. For all these valve bandwidths, the PI torque controller was differently tuned to give always the same closed-loop torque bandwidth of about 40 Hz. Then, the same passivity criteria used in Fig. 6.9 was again employed to determine the Z-width with these three different valves. Fig. 6.10a shows the Z-width for a valve with bandwidth of 50 Hz, while Fig. 6.10b depicts the Z-width for a valve bandwidth of 150 Hz and Fig. 6.10c for a valve of 250 Hz bandwidth. These plots clearly show that *the higher the valve bandwidth, the higher the Z-width.* In this new analysis, the damping range was increased (from $B_{vl} = 1600$ to $B_{vl} = 4000$) with respect to the previous results shown in Fig. 6.9 so that the difference in the Z-width could be seen.

The previous results demonstrated that, given a desired closed-loop torque bandwidth, faster valves are able to increase the Z-width of a system. Now, a third set of analyses aims to set a constant Z-width to examine the influence of different valves in the closed-loop torque tracking bandwidth. For each valve, the torque controller was tuned to obtain a desired Z-width with maximum passive damping of about $B_{vl} = 800 Ns/m$, as shown in the left plots of Fig. 6.11. The controller gain K_{PI} is also shown in these left plots. The plots in the right show the magnitude for the τ_{ref} to τ transfer function. The bandwidth is shown as the frequency where the
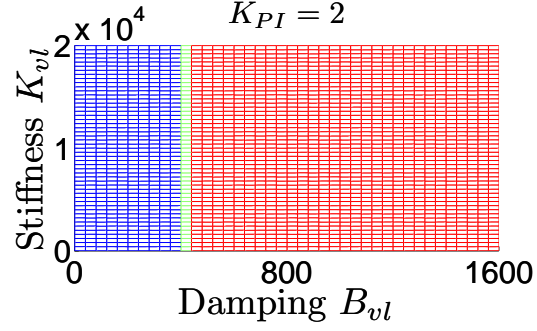
(a)
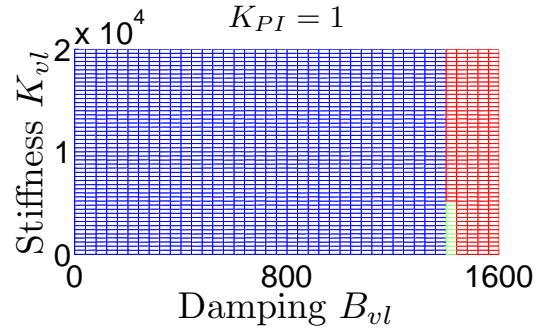
(b)
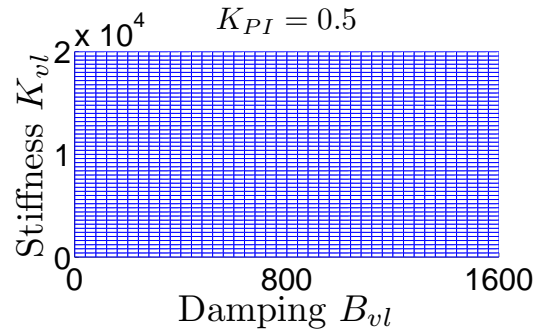
(c)

Figure 6.9: Z-width (blue area) for the HyQ leg considering different K_{PI} gains for the knee PI torque controller. The red area represents the *unstable* (and thus *non-passive*) range of impedances, the blue area with *passive* combinations of stiffness and damping, and the green one where the system is *stable but not passive*. As seen, the higher the inner torque controller gains, the smaller the Z-width.
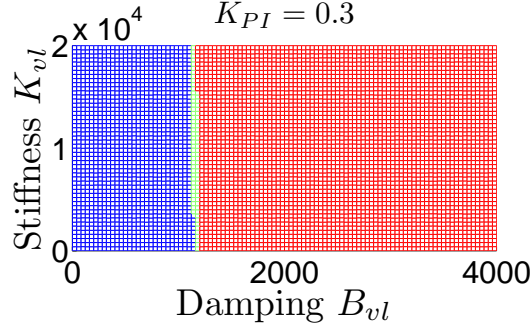
(a) Valve bandwidth $F_v = 50\ Hz$
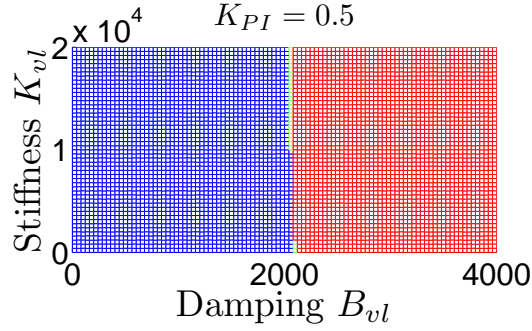
(b) Valve bandwidth $F_v = 150\ Hz$
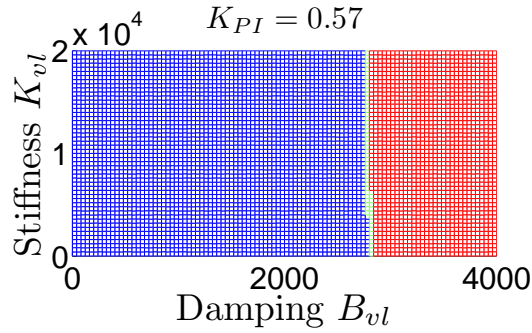
(c) Valve bandwidth $F_v = 250\ Hz$

Figure 6.10: Z-width for the HyQ leg with different valve bandwidths. The K_{PI} gain was adjusted to give the same closed-loop torque bandwidth of about $40\ Hz$ with all the valves. Again, the red area represents the *unstable* range of impedances, the blue area the *passive* impedances, and the green region the *stable, but not passive* combinations of stiffness and damping. As seen, faster valves are able to increase the Z-width for a given closed-loop torque bandwidth.

Table 6.1: Range of virtual stiffness K_{vl} and B_{vl} with different filters (Filter 1 is an averaging filter, and Filter 2 is a Butterworth filter), sampling time T_s, and torque controller gain K_{PI} for the knee joint. The valve bandwidth is the same for all these experiments ($F_v = 250\ Hz$).

$K_{vl}\ [N/m]$	$B_{vl}\ [Ns/m]$	Knee K_{PI}	Filter 1	Filter 2	$T_s\ [s]$
$1 - 20000$	$1 - 1600$	0.5	No	No	0.001
$1 - 20000$	$1 - 1380$	1	No	No and 1st order	0.001
$1 - 20000$	$1 - 400$	2	No	No	0.001
$1 - 20000$	$1 - 480$	2	No	1st and 2nd order	0.001
$1 - 20000$	$1 - 1600$	1	Yes	No	0.001
$1 - 20000$	$1 - 1200$	1	No	$2^{nd} order$	0.001
$1 - 20000$	$1 - 1000$	1	No	No	0.002
$1 - 20000$	$1 - 1600$	1	No	No	0.0005

magnitude is $-3\ db$. As seen, for a given Z-width, *the higher the valve dynamics the higher the closed-loop torque bandwidth.*

The influence of sampling time in the Z-width was also analyzed. As expected, for a given valve bandwidth ($F_v = 250\ Hz$), increasing the sampling time ($T_s = 0.002$ s) reduced the Z-width, and decreasing it ($T_s = 0.0005\ s$) made the system passive for all the selected range of impedances.

The introduction of velocity filtering, for dealing with noise and quantization errors, was also analyzed. Averaging filters increased the range of dampings from $B_{vl} = 1380$ to $B_{vl} = 1600\ Ns/m$. First order Butterworth did not cause any changes on the Z-width, while a second order Butterworth filter reduced the maximum stable damping to $B_{vl} = 1200\ Ns/m$. Since similar results have already been shown in the literature (see [Janabi-Sharifi et al., 2000]), such graphics will not be displayed in this thesis. However, the Table 6.1 presents a summary with many combinations of the controller gain K_{PI}, sampling time T_s, and filtering: the higher K_{PI}, the smaller the Z-width; the faster the sampling, the larger the Z-width; averaging or first order Butterworth filters could be used to reduce noises and quantization errors in the velocity signal and to increase the Z-width. The compliance tracking quality for some of these situations is discussed in the next section.

(a) Valve bandwidth $F_v = 50\ Hz$

(b) Valve bandwidth $F_v = 150\ Hz$

(c) Valve bandwidth $F_v = 250\ Hz$
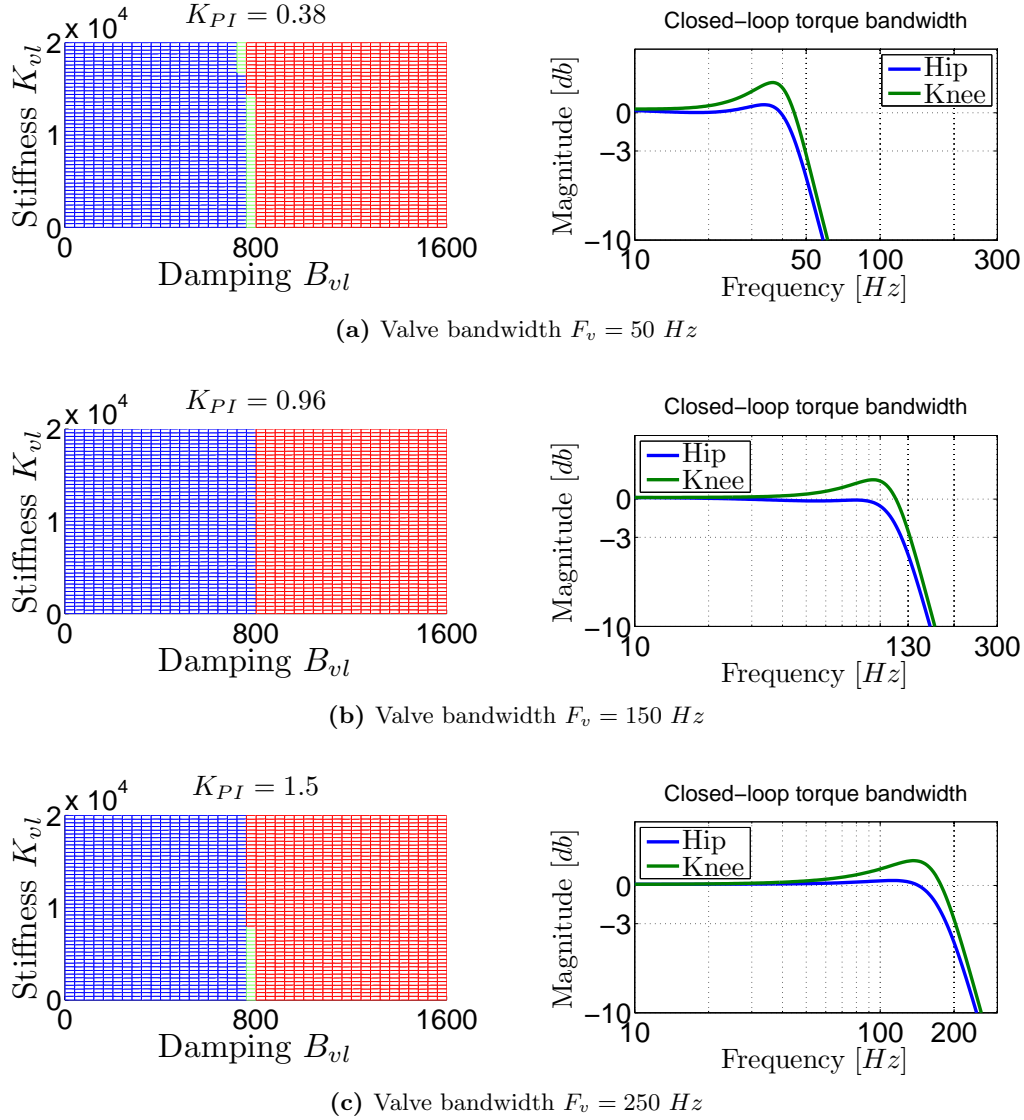
Figure 6.11: Z-width and magnitude plot of the closed-loop torque transfer function with different valve bandwidths. The K_{PI} gain was tuned to give, for all the cases, a Z-width with maximum passive damping of about $B_{vl} = 800\ Ns/m$ (plots in the left). Again, the blue are represents the passive range of impedances, while the small green region represents the stable, but not passive impedances, and the red area the unstable impedances. Given this constant Z-width, it can be seen that the higher the valve bandwidth, the higher the closed-loop torque bandwidth (plots in the right) for both the hip (blue line) and knee (green line) joints. In (a), the closed-loop torque bandwidth is about 50 Hz, in (b) it is 130 Hz and in (c) 200 Hz.

6.3 Torque performance influence on compliance tracking

The active compliance controller of HyQ uses a cascade control architecture, as shown in Fig. 6.1. In this arrangement, the inner torque loop performance can influence both the passivity and stability as well as the performance of the outer compliance loop.

The previous section (Section 6.2.2) showed that the performance of the inner torque loop affects the passivity of the outer loop. In general, for a given system, the higher the torque controller gains the smaller the range of stable stiffness and damping (Z-width) that can be employed in the outer loop. In that section, the virtual model control approach was used as outer controller for the compliance loop.

This section, on the other hand, demonstrates experimentally that although the system stability might be benefited by a low-gain torque controller, to intentionally reduce the torque controller performance can significantly restrict the compliant behavior of the robot.

The experiments to assess the influence of the torque performance on the compliance control shown in this section were carried out with the HyL setup. And the force controller employed is the feedback linearization one.

	Hip	Knee
K_p	$1.3 \cdot 10^7$	$1.1 \cdot 10^7$
K_i	1.5	1.0
K_{vc}	0.65	0.65
K_{pc}	1.0	1.0

Table 6.2: Force feedback linearization controller gains defined in the control law Eq. 5.14

The first experiment consisted in performing a 2 Hz sinusoidal motion in the air with different gains for the inner force controller. In this experiment, the compliance control approach PD joint-space position control with inverse dynamics, described in Section 6.1.1, was employed. Initially, the motion was performed with the set of gains shown in Table 6.2. Then, gain K_{pc} was reduced to a quarter of its original value. This gain, as seen in Eq. 5.14, scales the outcome of the PI controller (function v)

and the nonlinear velocity compensation (function $f(x_p, \dot{x}_p, \ddot{x}_p)$). This is equivalent to the gain K_{PI} presented for the linear controller in Eq. 6.18. As seen in Fig. 6.12a and Fig. 6.12b, the force controller gains strongly affect also the position tracking. The relative position tracking error, plotted as a blue line in the last plot, highlights the importance of having a high-performance inner force controller in a cascade compliance control scheme.

The second experiment to evaluate the impact of the force controller performance in the compliant behavior of the robot used the virtual model control approach (Section 6.1.3). In this experiment, an exponential spring with a linear damping was used. The leg was put on the ground and then manually pushed down to verify the characteristics of the emulated compliant system. Fig. 6.13a shows the tracking of the desired compliant behavior with the nominal force gains presented in Table 6.2. Then, Fig. 6.13b and Fig. 6.13c demonstrate how the capability of mimicking virtual compliant behaviors is strongly limited when the force gains are reduced.

6.4 Procedure for designing a compliance controller

The two experimental results shown in the last section (Section 6.3) clearly demonstrate that, although a reduction in the torque performance might increase the stability ranges of the actively-compliant system, it can seriously hamper the compliant behavior of the robot. Therefore, several aspects must be considered in the controller design to reach the best trade-off between stability and performance. Based on these experimental results and on the passivity and stability analyses presented in Section 6.2.2, the following procedure can be defined to design a cascade compliance controller:

- The fist step should be the estimation of the range of impedances (Z-width) needed by the robot to satisfy all the requirements imposed by the tasks that it has to accomplish. For instance, a versatile robot as HyQ, which aims to perform many different tasks (e.g. walking, trotting, running, jumping), most likely requires a larger Z-width than a robot that is specific to a single application (e.g. walking or trotting).

(a) Force gain $K_{pc} = 1$

(b) Force gain $K_{pc} = 0.25$
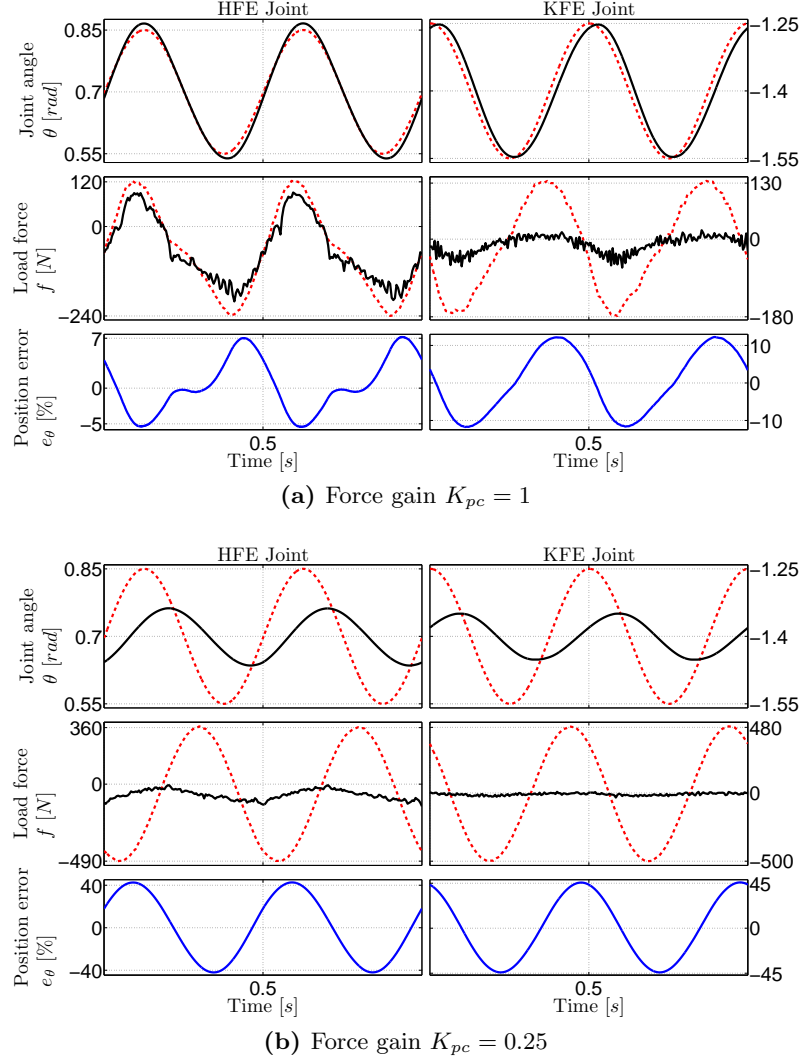
Figure 6.12: Position and force tracking performance for a 2 Hz sinusoidal motion with different force controller gains. In (a) the force gains have their nominal values ($K_{pc} = 1.0$), while in (b) the gains were reduced to a quarter of the nominal values ($K_{pc} = 0.25$). As seen, the reduction of the force control performance, emulated by reducing the gains, had a strong effect on the position tracking. The position gains were set as $K_p = 150 \ Nm/rad$ and $K_d = 5 \ Nms/rad$ in both experiments. The first two plots show the position and force tracking respectively, where the dashed red line represents the reference and the solid black line the actual value. The third plot of each figure shows the position tracking error relative to the reference amplitude, which is defined as $e_\theta = (\tau_{ref} - \theta)/(\theta_{ref_{max}} - \theta_{ref_{min}})$. As seen, the position tracking errors increase significantly when the force gains are reduced. This means, in other words, that the actually realized compliant behavior of the robot is very different from the expected one due to the low force control performance. In this experiment, the outer loop control approach used was the PD + inverse dynamics.
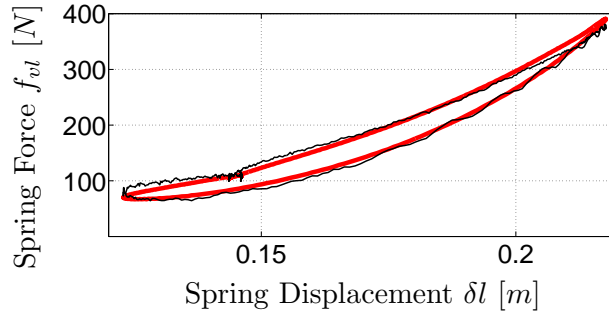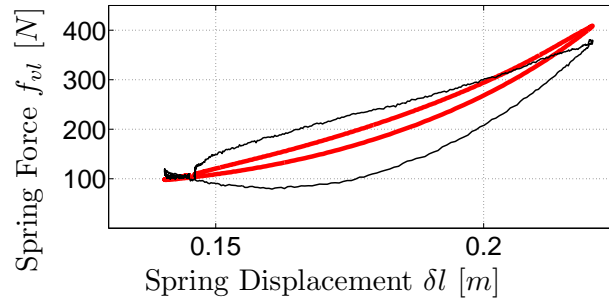
(a) Force gain $K_{pc} = 1$

(b) Force gain $K_{pc} = 0.5$
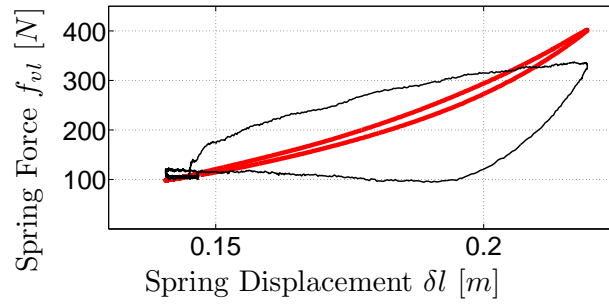
(c) Force gain $K_{pc} = 0.25$

Figure 6.13: Emulation of a virtual exponential spring-damper with different gains for the force controller. The leg was placed on the ground and pushed down by hand. The desired force profile is depicted in red, while the real behavior presented by the leg is shown in black.

- Once the Z-width is estimated, the inner torque controller should always be tuned to give the maximum stable closed-loop torque bandwidth which satisfies the limits imposed by the selected Z-width. This maximum closed-loop torque bandwidth will produce the best compliant performance possible for that Z-width, as shown in Fig. 6.13 where higher gains produce a better compliance tracking.

- Depending on the selected Z-width, this choice might limit the torque controller gains (Fig. 6.9) and consequently the compliant performance (Fig. 6.13. Therefore, in case the compliant performance does not satisfy the designer requirements, a faster actuator can be selected. As shown in Fig. 6.11, for a given Z-width, the higher the valve dynamics the higher the closed-loop torque bandwidth.

This is a simple procedure that might help robot controllers to find the most suitable trade-off between stability and performance. It gives some important practical insights to deal with instabilities in the compliance control loop. For instance, in case some instability appears when increasing the damping in the legs, a reduction in the torque controller gains can already solve the problem and increase the Z-width. According to Table 6.1, an increase in the sampling frequency or an averaging filtering in the velocity signal can also help in increasing the Z-width. Otherwise, changes in the hardware might also be necessary for increasing the closed-loop torque bandwidth and/or the Z-width.

As further discussed in Section 7.1, a limit in the torque performance will always exist, and it depends mainly on the load characteristics such as inertia and damping. Thus, depending on the load dynamics, it might be that in practice increasing the torque bandwidth does not necessarily improve the compliance tracking. In this cases, the only way to still improve the compliance control performance is by changing the load characteristics. For instance, especially for low-inertia links, viscous friction could be intentionally added to the robot joint to improve the torque tracking at the price of energy loss.

Chapter 7

Discussion

So far, this thesis presented the fundamentals of hydraulics that are important to robotics, as well as a new framework for representing the force dynamics transmitted to a load. In addition, the core of the thesis was presented in the last two chapters, where relevant hydraulic and rigid body model information was used to design high-performance force and compliance controllers.

Some immediate results regarding the performance of single controllers were already presented within the previous chapters. This chapter aims then to show more general results and applications of the designed controllers, as well as to present some practical issues that can strongly influence the performance of such controllers. Some limitations in force and compliance control are discussed and alternatives to overcome them suggested.

7.1 Torque control performance

The performance of force/torque controller can be influenced by several aspects. For instance, the load characteristics, such as inertia and damping, play an important role in the force dynamics.

Also, in practical applications, some hardware issues can limit the force control performance. In HyQ, the force sensor noise was one of these issues. Due to the big range of measurement of the load cell (± 5 kN), the relative small noise level of $\pm 1\%$ cause an absolute noise of ± 50 N. First, this noise limited the derivative gain magnitude of the force PID controller. Thus, in practice the influence of the

derivative term was not significant due to the low D gain, and therefore the PID was simplified to a PI. Furthermore, this 100 N of noise restricted the tracking performance for small force references that were in the range of the noise.

This section first discusses the influence of the load characteristics in the force control performance. Then, some relevant aspects regarding the hydraulic transmission stiffness and its influence on the force control are presented.

7.1.1 Load characteristics

The HyQ robot controls the joint torques through the control of the load force in the hydraulic cylinders. The load force f is a measurement of all the forces that oppose the motion. In other words, f expresses all the reaction forces acting on the cylinder rod. Thus, the load force can only be as high as the sum of these counter forces.

There are four main sources of counter forces:

- Friction forces: when surfaces in contact move relatively to each other, the friction between them converts kinetic energy into heat.

- Inertial forces: based on the Newton's first law, any physical object resists to a change in its state of motion or rest. Thus, inertial forces appear always when a body has to be accelerated or decelerated.

- Elastic forces: they are created when there is contact with some elastic element, such as a spring. This elastic element, which can be soft as a rubber or hard as a brick, produces a reaction force when compressed or extended.

- Gravitational forces: due to gravity, the weight of a mass produces a force on the actuator. This force can both oppose the motion as well as aid it, depending on the motion direction with respect to the gravity.

The friction forces are maybe the most important counter forces in force control. Nonlinear friction forces, such as static and Coulomb, are very disadvantageous and undesired in force control. Their discontinuities can cause stability problems. For instance, instability issues were already experienced with HyQ due to the bearings wear.

The viscous friction, on the other hand, can be very favorable to force control. It varies linearly with the velocity and introduces damping into the system, contributing for its stability.

As seen in Eq. 3.40 and Eq. 4.13, the load viscous friction B_l introduces a zero in the load force transfer function. The zero location is defined by the magnitude of B_l. The lower B_l, the lower the zero frequency. For low B_l, the load zero remains very close to the origin, and the effects of an integrator in the controller are practically eliminated. Thus, low load viscous friction can seriously limit the response performance of traditional force controllers.

In the HyQ legs, the main source of friction comes from the hydraulic cylinder. The tight sealing between the piston and cylinder body creates a considerable viscous friction of about $B = 1000 \ Ns/m$. This high B is very beneficial for controlling the hydraulic force f_h, since in this case the piston can be considered part of the load, as seen in the numerator of Eq. 4.12.

Nevertheless, the cylinder friction B cannot be considered part of the load friction in case the load force f is considered. The load viscous friction in this case, derives mainly from the joint bearings and thus is very small. This friction B_{l_θ} acts on the robot joints, affecting directly the actuators which are placed also in the joints, as the electric motors of the HAA joint of HyQ (Fig. 1.2b). As seen in Eq. 4.15, B_{l_θ} is the only friction present in the transfer function zero.

The hydraulic cylinders, however, do not directly actuate the HyQ HFE and KFE joints. A nonlinear lever arm l_{la} [Semini, 2010], depicted in Fig. 7.1, works as the Jacobian between the point where the cylinder is attached and the joint. It relates the cylinder force with joint torque ($\tau = l_{la} \ f$), and also the cylinder linear velocity with the joint angular velocity ($\dot{x}_p = l_{la} \ \dot{\theta}$). Based on the virtual work principle [Sciavicco and Siciliano, 2001], the joint viscous friction can be mapped into the cylinder space by the following relation:

$$B_{l_\theta} = J^T B_l \ J \ \Rightarrow \ B_l = \frac{1}{l_{la}^2} B_{l_\theta} \tag{7.1}$$

where,

B_{l_θ}: load viscous friction coefficient in joint space $[Nms/rad]$

B_l: load viscous friction coefficient in cylinder space $[Ns/m]$

The implication of the above relation in the load force control is very important. Considering the values for the lever arm l_{la} shown in Fig. 7.1, this means the bearing friction seen by the cylinder is at least 500 times bigger than the friction seen at the joint. The load force control is therefore benefited from this high B_l since the zero due to the natural load velocity feedback goes to higher frequencies, as seen in Eq. 4.13. Therefore, the limitation imposed by this zero in the closed-loop response is attenuated in the cylinder space with respect to the joint space. The fact that $B_l >> B_{l_\theta}$ is one of the reasons why, in HyQ, the torque tracking performance is higher with hydraulic actuators (HFE and KFE joints) than with electric ones (HAA joint).
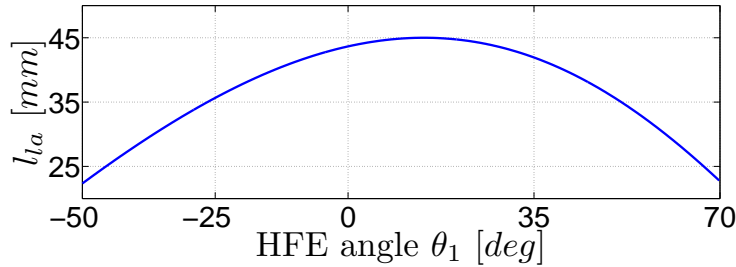
Figure 7.1: The effective lever arm length l_{la} varies according to the joint angle. This plot shows the l_{la} profile for the HFE joint of the left front leg of HyQ. It has a maximum value of 45 mm around the middle of the angular position range, and minimum of 22.5 mm at the extreme positions.

The inertia also plays an important role on the force control performance. Generally, properly designed robots have heavier links close to their base while the end-effector is as light as possible. In this case, considering that the friction is the same for all the joint, the robot's joints close to the base will always present better force control performance than the joints close to the end-effector. This is due to the negative gradient of the reflected inertia from the base to end-effector.

To illustrate the influence of the inertial forces into the load force control, a simulation was performed with different load masses M_l. The force controller employed in the simulation was a PID. The load mass slides on a horizontal surface (no gravitational forces) with low damping B_l, as depicted in Fig. 3.6. The closed-loop load

force response to a unit step input is shown in Fig. 7.2 for different M_l values. As seen, the heavier the load the smaller the error in steady state.
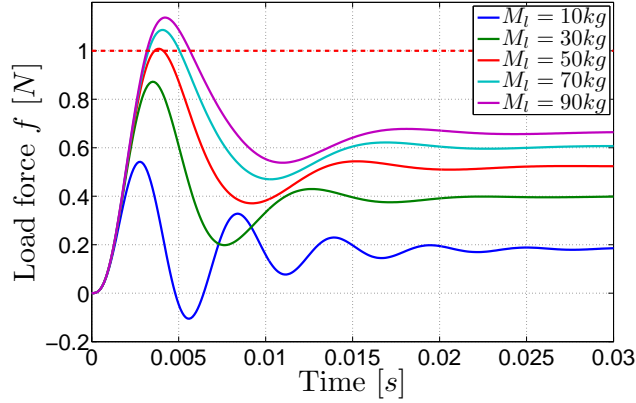
Figure 7.2: For a unit step input a PID force controller behaves as a PD controller when the load friction is low. The steady-state error depends on the inertia of the system: the heavier the load the smaller the error in steady state. The dashed red line represents the force reference.

The results presented in Fig. 7.2 suggest that a PID controller is not suitable for controlling the load force of a load with low inertia and low damping. These are the worst load characteristics for performing force control due to the low counter forces produced by the load. These characteristics are found in the HyQ leg when it is in the air, especially for the KFE joint that has a very light (about 800 g) link attached to it.

However, when the leg touches the ground, things change significantly. The joints start to be loaded not only by the mass of the links supported by it, but by the whole robot weight and inertia that supports the joint. For instance, considering all the four HyQ legs are on the ground, each leg would see a quarter of the robot weight. In this case, when the leg is partially loaded with the robot weight, the performance of a PID controller increases significantly considering no force saturation occurs.

For the velocity compensation force control approach, the changes in inertia do not cause considerable variation in the load force closed-loop response, as shown in Fig. 7.3. However, in this approach, to achieve the desired force set point with low inertia and damping, big accelerations have to be provided by the actuation system, and velocity (flow, in hydraulics) saturations might occur. This would reduce the effectiveness of the velocity compensation approach. In hydraulics, to ensure the

delivery of the demanded flow, the pump must be properly dimensioned and an accumulator employed.
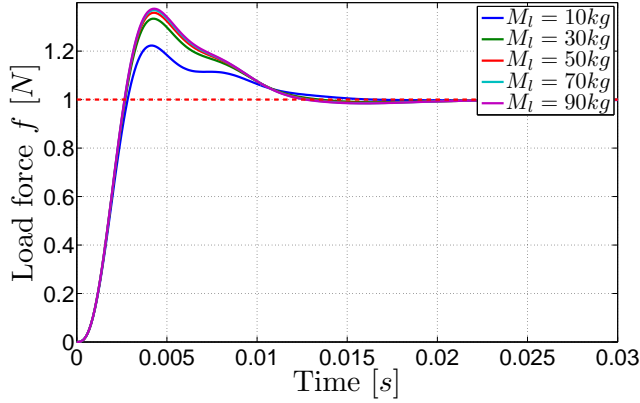
Figure 7.3: For an unit load force step, when velocity compensation is used the response is not significantly affected by a change in the load inertia. All the responses present essentially the same settling time and zero steady-state error.

The influence of the inertia on the force tracking capabilities of the HyQ leg was also verified through two experiments with the HyL setup. While in the first experiment no additional weight was added to the leg, for the second experiment a 2 kg weight was added to the foot. For both cases, a 2 Hz sinusoidal motion was performed with the leg in the air. For the compliance control loop, the joint-space PD position controller with inverse dynamics was used, and for the force loop the feedback linearization approach. The force tracking for the HFE and KFE joints and also the respective force tracking errors are shown in Fig. 7.4a for the no additional weight case, and in Fig. 7.4b for the case with 2 kg attached to the foot. The dashed red line depicts the force reference, the solid black line the actual force, and the blue line the force tracking error e_f relative to the force reference amplitude $f_{ref_{amp}}$ ($e_f = 100 \ (f_{ref} - f)/f_{ref_{amp}}$).

As discussed previously, distal links have always smaller reflected inertia with respect to proximal links. Therefore, proximal joints tend to present a more satisfactory force response than distal joints. This characteristic can be noticed in both Fig. 7.4a and Fig. 7.4b, where the HFE joint clearly demonstrates better force tracking capabilities than the KFE joint.

The extra 2 kg added to the foot improved the force tracking for both HFE and
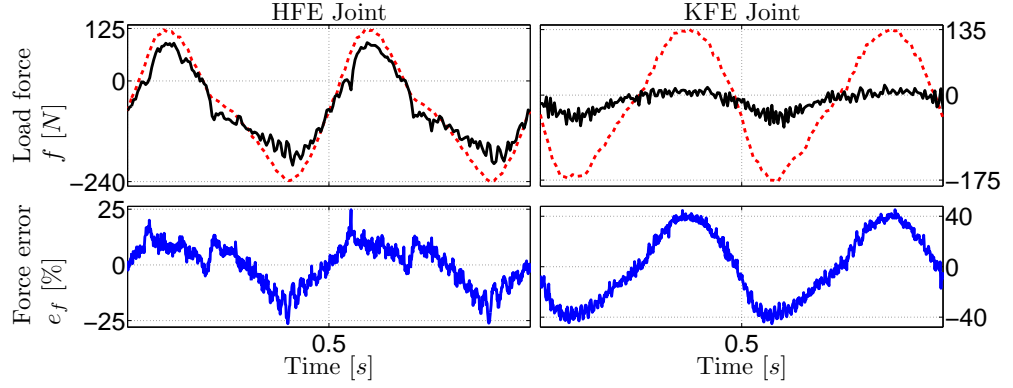
(a) Leg with no extra weights
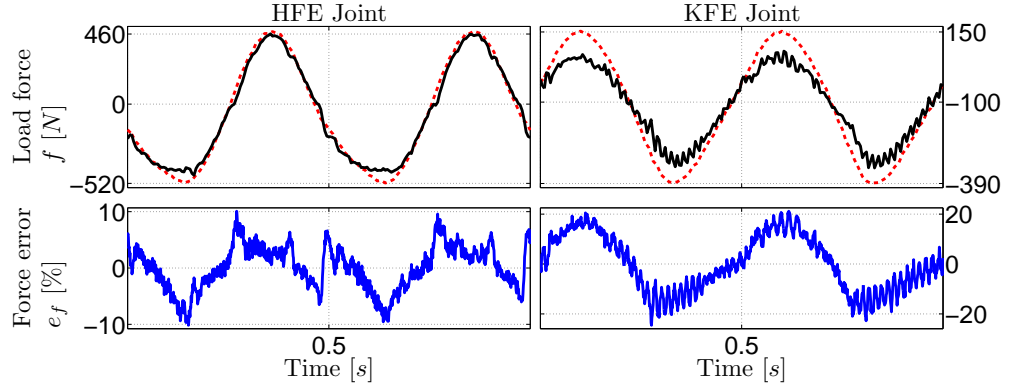
(b) Leg with 2 *kg* extra weight at the foot

Figure 7.4: Experimental results which show the force tracking, and respective force tracking errors, for a 2 *Hz* sinusoidal motion and *different weights* at the foot. In each figure, the first plot shows the force tracking, where the dashed red line represents the force reference created by the position control and the solid black line the actual force. The second plot shows the force tracking error relative to the force reference amplitude (e.g., in (a) the force reference amplitude is $f_{ref_{amp}} = 365$ *N* for the hip and $f_{ref_{amp}} = 310$ *N* for the knee). As seen, the HFE joint has always a better force tracking performance than the KFE. However, the additional weight had a greater impact in the KFE force tracking performance due to the substantial increase in inertia.

KFE joints. As seen in Fig. 7.4b, this additional inertia reduced the force tracking error to about $e_f = \pm 10\%$ for the HFE joint and $e_f = \pm 20\%$ for the knee joint. However, looking at the force tracking plots, it can be seen that the improvement of the KFE joint is more effective than the HFE one.

7.1.2 Velocity Compensation

If no velocity compensation is used, the force closed-loop performance is limited by the zero due to the load dynamics, as discussed in Section 5.2.2. Considering a PID controller, this load zero attracts the pole of the controller integrator and prevents it from going to higher frequencies. For a non-oscillatory response, this low-frequency pole is the dominant one and it limits the system velocity in closed-loop.

As explained in Section 5.2.2, the velocity compensation cancels the zero present in the force dynamics. This cancellation allows us to increase the controller gains and put the dominant pole at high frequencies without making the system unstable. However, the velocity compensation is a model-based compensation, therefore it is susceptible to parameter uncertainties. This means that a perfect zero/pole cancellation is as challenging as creating a perfect model. In practice, the velocity is either under or over compensated.

The zero-pole map of Fig. 7.5 shows the dominant open-loop poles for different levels of under and over compensations. An under compensation places both dominant open-loop poles at the left side of the zero, and an over compensation places one at its left and one at its right.

It can be demonstrated that, by closing a loop with a PID controller, the dominant closed-loop pole of the under-compensated system is still limited by the frequency of the zero. For the over-compensated case, the dominant pole can go beyond the zero frequency, increasing the system bandwidth. However, a slight over-compensation can make the system unstable for certain controller gains, reducing the robustness.

Another possible practical issue of the velocity compensation approach is the velocity data acquisition. Usually, it is obtained by numerical differentiation of the position signal, which can be noisy. HyQ uses high-resolution digital encoder ($80,000$ *counts/revolution*), which provides a position signal with only a low level of quantization noise and consequently a reasonable velocity signal can be obtained.
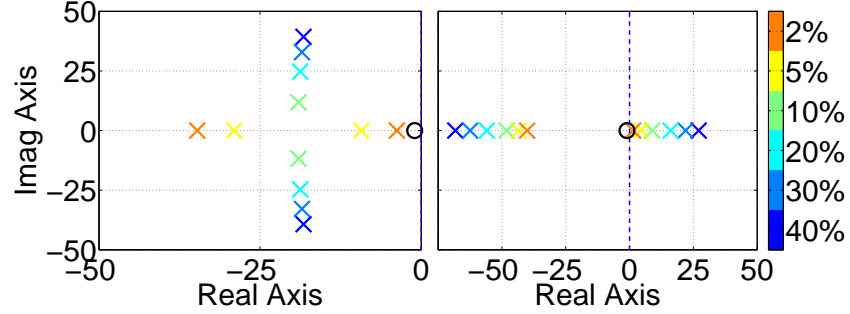
Figure 7.5: Root locus of the open-loop poles of the load force dynamics: The left plot shows the under-compensation case, and the right side the over-compensation one. The color bar illustrates different percentages of under/over compensations. The zero introduced by the load is marked as a black circle close to the origin. A small over-compensation can already place some open-loop poles at the right-side of the imaginary axis, making the closed-loop system more susceptible to instability.

7.2 Hydraulic Transmission stiffness

Force control is always done through a compliant transmission element. For instance, in series elastic actuators (SEA) the spring works also as a low-pass filter, lowering the transmission stiffness. This reduced overall stiffness matches the available actuator bandwidth, reducing the difficulty of the torque control issue. However, in this approach the achievable load force bandwidth is limited by the stiffness of the spring: the softer the spring, the slower the load force dynamics. The most appropriate spring stiffness is certainly a very difficult parameter to select and this choice can seriously limit the robot's dynamic performance and versatility.

To illustrate the importance of the hydraulic transmission K_{th} in the load force dynamics, Fig. 7.6 presents the bode plot of the open-loop load force transfer function. As seen, the higher K_{th} the higher the crossover frequency. Also, the higher K_{th} the higher the frequency where phase delay is introduced. Thus, when closing the loop, bigger phase margins can be obtained and possibly also better tracking performances [Franklin, 1993].

The very low fluid compressibility makes the hydraulic transmission intrinsically stiff. Some design aspects, such as the flexibility of the pipes, can reduce this high hydraulic stiffness. All these aspects define the *effective bulk modulus* of the hydraulic system, as mentioned in Section 3.1.1.

In addition, as seen in the definition of K_{th} in Eq. 4.4, the hydraulic transmission
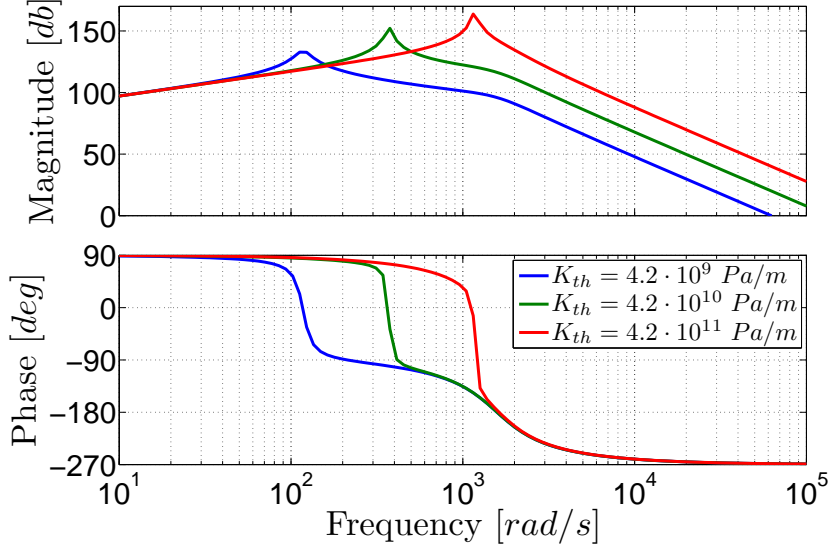
Figure 7.6: Bode plot for the load force transfer function (Eq. 4.13), which considers the valve dynamics. As it can be seen, changes in the hydraulic stiffness K_{th} significantly influence the natural frequency of the open-loop load force dynamics. Also, the higher K_{th} the higher the frequency where phase lag started to increase.

stiffness depends also on the chamber volumes. Differently from real springs, which transform a certain displacement into force, the hydraulic stiffness transforms a certain piston displacement into pressure. That is, the hydraulic stiffness has unity Pa/m. To obtain a stiffness in N/m, which has a more intuitive meaning, the stiffness K_{th} has to be multiplied by the equivalent actuator area A_e. The result of this multiplication, considering HyQ's parameters, is plotted in Fig. 7.7.

Since the stiffness is higher at the minimum and maximum cylinder positions, the system is more reactive at these positions, and the force control more challenging. Also, if the gains of a linear controller are tuned based on an equilibrium point where the stiffness is low, it might become unstable at these extreme positions.

The stiffness magnitude at the minimum and maximum positions depends directly on the pipe line volume that connects the valve to the cylinder chamber. When the pipe volume approaches zero, the stiffness tends to infinity. Thus, the pipe volume plays an important role in the robot design and it must be taken into account when matching the transmission stiffness to the actuator bandwidth, which is defined by the valve dynamics. HyQ uses valves with a bandwidth of 250 Hz. These fast valves are able to cope with the high stiffness plotted in Fig. 7.7, which
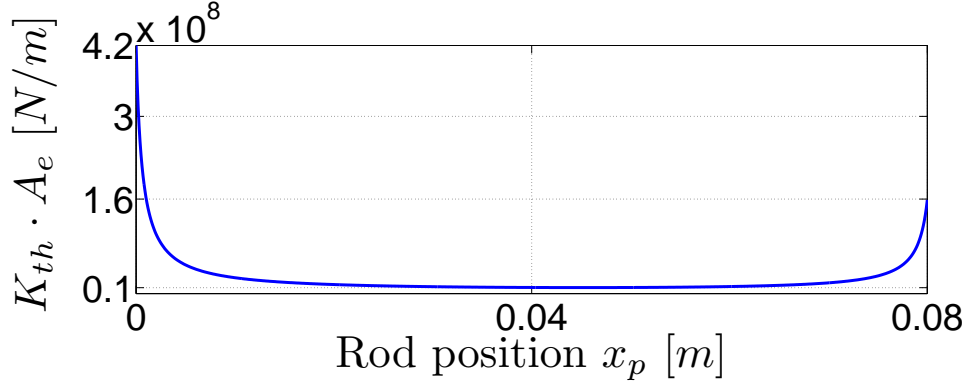
Figure 7.7: Hydraulic stiffness of the asymmetric cylinder of HyQ for a rigid pipe of length $L_{pl} = 10\ cm$ and internal diameter $D_{pl} = 4\ mm$. The hydraulic stiffness depends on the fluid properties, on the cylinder areas, on the pipe length and flexibility, and on the cylinder rod position x_p.

has a minimum value of $K_{th} = 1 \cdot 10^7\ N/m$.

The hydraulic equivalent stiffness shown in Fig. 7.7 is for a hydraulic cylinder with a pipe of length $L_{pl} = 10\ cm$ and internal diameter $D_{pl} = 4\ mm$ connected to its ports. Considering the valve is closed, this stiffness represents how much force is produced when the cylinder rod is pulled or pushed. This linear stiffness of the cylinder can be mapped into a rotational stiffness K_{th_θ} at the joints through the nonlinear lever arm l_{la} shown in Fig. 7.1. The virtual work principle, used in Eq. 7.1 to derive the relation between the damping at the cylinder and joint spaces, is also valid for the stiffness, that is:

$$K_{th_\theta} = J^T K_{th}\ J\ =\ l_{la}^2 K_{th} \tag{7.2}$$

where,

K_{th_θ}: rotational hydraulic stiffness in joint space $[Nm/rad]$

K_{th}: linear hydraulic stiffness in cylinder space $[N/m]$

In Fig. 7.8, the rotational stiffness K_{th_θ} at the HFE joint is shown for different pipe line lengths. For the HyQ case ($L_{pl} = 10\ cm$, depicted in green), this stiffness goes from $K_{th_{\theta_1}} = 4 \cdot 10^4\ Nm/rad$ to about $K_{th_{\theta_1}} = 8 \cdot 10^4\ Nm/rad$. However, in most of the range all the stiffnesses remain around $K_{th_{\theta_1}} = 2 \cdot 10^4\ Nm/rad$. This value is comparable to the one found in the harmonic drives used in the HyQ

electric motors, which is around $K_{te} = 2.7 \cdot 10^4$ [Focchi et al., 2012]. Thus, although the pipe line length L_{pl} changes significantly the stiffness values at the initial and final positions of the cylinder, in most of the range $(-25° < \theta_1 < 35°)$ it does not influence too much the stiffness in the joint space.
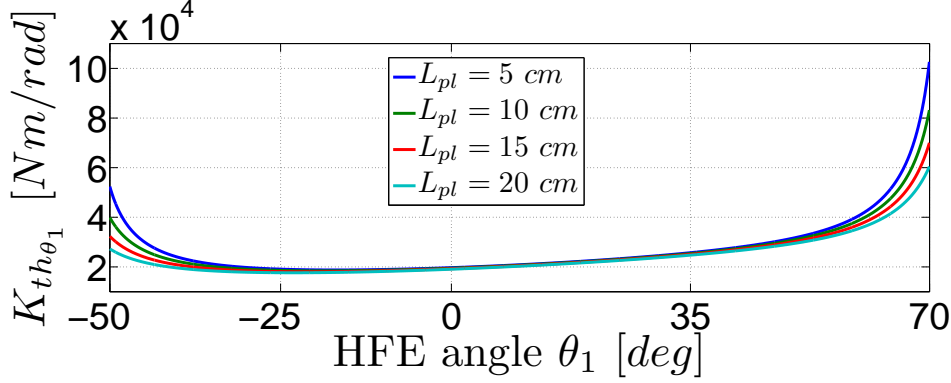
Figure 7.8: Mapping of the hydraulic stiffness K_{th} into the rotational space of the HFE joint. The variable stiffness $K_{th_{\theta_1}}$ defines how much torque is created when the HFE joint is moved with the valve blocked. This is equivalent to the stiffness of a rotational spring placed in the joint. The influence of the pipe line lengths is also shown. HyQ uses a rigid tube length of about 10 cm between the valve and cylinder, thus the green line is the one that currently represents the rotational stiffness of the HFE joint. The tube internal diameter is the same for all the plots ($D_{pl} = 4 \ mm$).

The fact that at the joint level both hydraulic and electric actuation have similar transmission stiffness cannot be used for comparing their force control capabilities though. The control of the hydraulic force is not performed at the joint space, but in the cylinder space, where the hydraulic transmission stiffness (Fig. 7.7) is at least 400 times stiffer than the electric transmission stiffness ($K_{te} = 2.7 \cdot 10^4$). Therefore, since the transmission stiffness defines the open-loop gain of the load force (Eq. 4.13) and torque (Eq. 4.15) dynamics, the hydraulic actuation has a higher open-loop gain which also permits to obtain faster stable closed-loop responses.

7.3 Active Compliance

HyQ is an actively-compliant robot that does not have any spring in it. Nevertheless, it can perform very dynamical motions such as running trot and squat jumps.

The key aspect on achieving a high-fidelity compliance control is the torque loop. The performance obtained with the inner force loop permits to track in a

very satisfactory manner the desired torques created by the compliance controller, as shown in Chapter 5 and Section 7.1.

A very intuitive way of designing a compliance controller is through virtual elements. As described in Section 6.1.3, the HyQ leg is able to mimic the behavior of a virtual telescopic leg by using different types of stiffness. For instance, Fig. 6.7 shows how well HyQ is able to emulate two different springs: a linear and an exponential. Fig. 6.13a also demonstrates that HyQ can behave as a nonlinear spring-damper.

This section aims to present other features, applications, and also limitations in the HyQ active compliance. Firstly, the capability of varying the leg stiffness on-the-fly is presented, which is a very important feature that enhances the robot's versatility. Then, the performance of the HyQ actively-compliant leg is compared with a special passively-compliant version of the leg. Finally, some highly-dynamic applications with the whole robot are shown to demonstrate the suitability of the compliance controller for such versatile legged machines.

7.3.1 Leg stiffness variation

One of the big motivations behind the use of active compliance is its versatility. An actively-compliant robot can change its stiffness and damping coefficients on-the-fly, during the execution of a particular task. This versatility can improve the robot capabilities in dealing with many kinds of terrain, in accomplishing different tasks such as running, jumping, and walking, and in interacting with objects and humans.

The following two examples demonstrate that HyQ can change the compliance parameters on-the-fly. The feedback linearization approach was used for the force controller and the virtual model shown in Fig. 6.6 for the compliance controller.

The first example uses the HyL setup presented in Section 1.2.1. It consists of a hopping-in-place experiment. To implement it, the initial length of the virtual leg $l_{vl_0} = 0.55$ was varied sinusoidally ($\delta l_{vl_0} = 0.04\ m$) at a constant frequency of 1.6 Hz. Then, the virtual leg stiffness K_{vl} was ramped up from $K_{vl} = 800$ to $K_{vl} = 3000$ N/m.

As shown in Fig. 7.9, during the first second the leg height h_l is oscillating with a constant amplitude due to the sinusoidal variation in the length l_{vl_0} of the virtual spring. After 1 s, the spring stiffness starts to increase and, consequently,
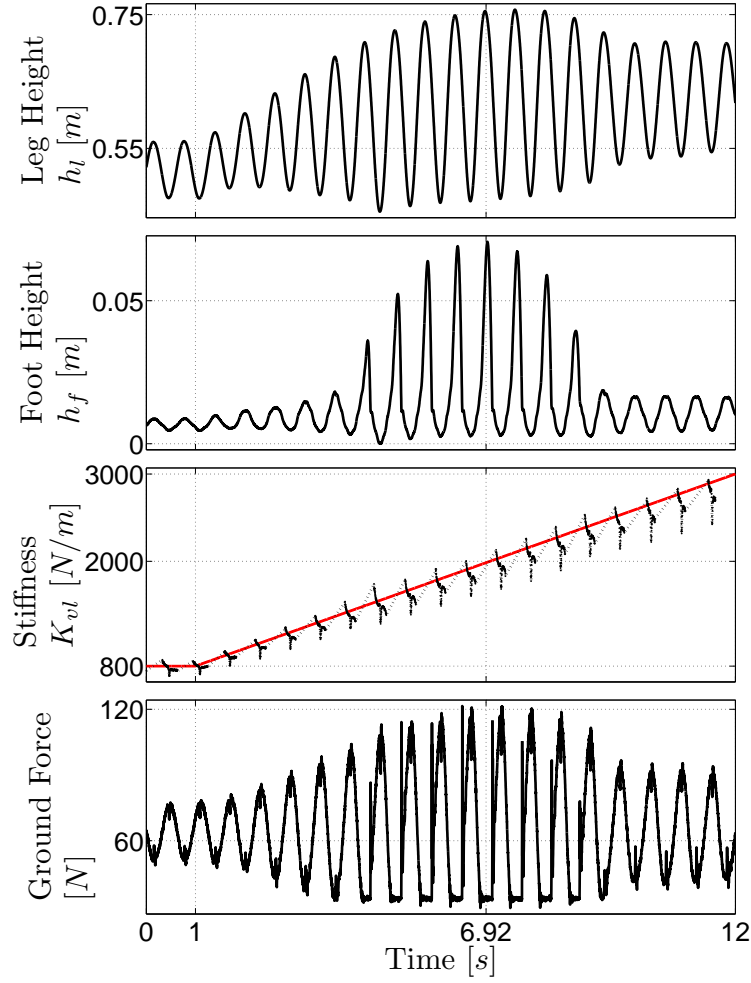
Figure 7.9: A sinusoidal excitation is applied to the virtual spring length l_{vl_0}, and the stiffness K_{vl} is linearly increased at a rate of 200 N/ms. The change in stiffness alters the resonance frequency of the leg, which behaves as a spring-mass system. Within a range of stiffness, a resonance occurs and starts the leg hopping-in-place, as seen in the foot height h_f plot. The vertical ground reaction forces are plotted in the last plot.

the amplitude of the leg height h_l oscillation grows due to resonant effects. The leg starts to hop when the stiffness, and thus the natural frequency of the own leg, resonates with the sinusoidal spring length excitation frequency, as seen in the foot height h_f plot. The resonance peak occurs at 6.92 s, when the stiffness is around 2000 N/m. The vertical ground contact forces were measured by a force plate. During the hopping they reach a peak value of 120 N, going to zero during flight phase. The stiffness created by the virtual linear spring was plotted only for the stance phase and interpolated during the flight phase (dashed black line).

The second example which demonstrates HyQ's ability to change its legs stiffnesses uses the whole quadruped robot. It extends the previous example, which was done for a single leg on a slider, to all the four HyQ legs. In this example, the robot was free to move. The excitation applied to the virtual spring length had the same frequency (1.6 Hz), the variation magnitude was $\delta l_{vl_0} = 0.04$ m, and the stiffness ranged from $K_{vl} = 2000$ to $K_{vl} = 5000$ N/m.

As presented in Fig. 7.10, after 1 s the springs stiffness start to increase. Again, due to resonant effects the amplitude of the motions grows and HyQ, which weighs about 75 kg, starts to hop. The first plot shows the ground reaction force for just one of the HyQ legs: the left front leg. The resonance peak occurs at about 10 s, when the stiffness is around $K_{vl} = 3800$ N/m.

7.3.2 Comparison with a real spring

As discussed previously, active compliance has been so far employed essentially in low-velocity tasks, such as assembly systems. The practical reason for that was the poor torque bandwidth reached by such manipulators and also the weakness of mechanical parts such as gear boxes, which cannot resist to high impact forces.

For experimentally assessing the active compliance controller performance for high-frequency perturbations, the actively-compliant leg of the HyL setup was dropped from a height of $h_f = 25$ cm onto a force plate, where the ground reaction forces were measured. Then, the knee hydraulic cylinder, which has been used till now to emulate the virtual elements, was removed. In its place a physical spring-damper was inserted, as shown in Fig. 7.11. Due to mechanical constraints, the real spring-damper could not be attached to the foot. It was then attached about 6 cm away from the foot along the lower link axis.
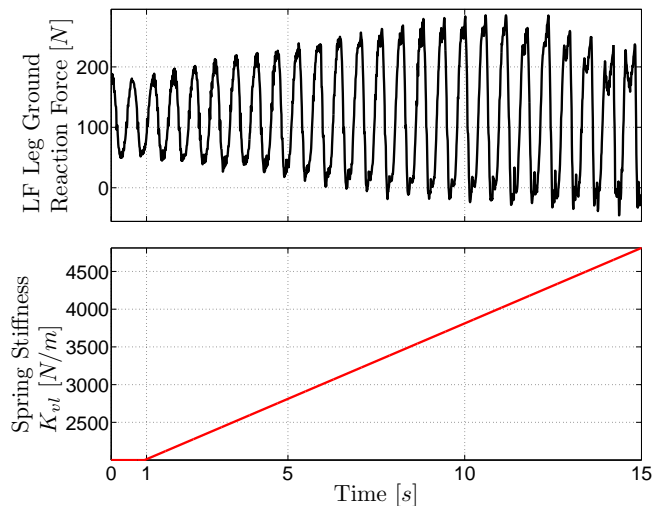
Figure 7.10: A hopping motion was implemented by exciting the HyQ robot in a resonant way by varying the virtual legs stiffness. The first plot shows the ground reaction force for the left front (LF) leg, which was calculated based on the joint measurements using the Jacobian transpose method. It is zero after 6 s evidencing a presence of a flight phase. The second plot presents the linear change in stiffness applied to all the HyQ legs.
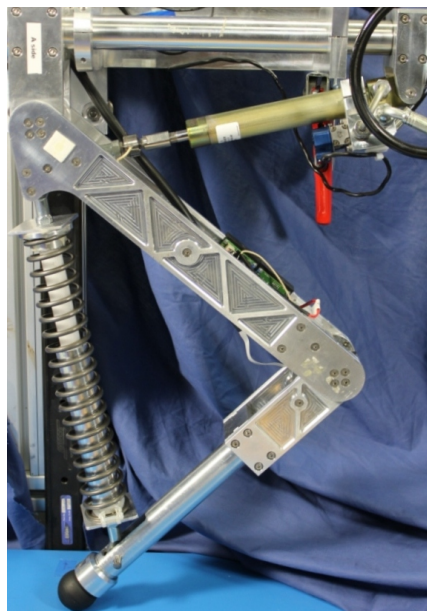
Figure 7.11: HyL leg using a real spring-damper between the hip and the foot. The behavior of this *passively-compliant* version of the leg was used to validate the *actively-compliant* behavior obtained with virtual model control.

Then, the dropping experiment was repeated with this passively-compliant leg. The leg weight was not relevantly affected with this change. To be coherent with the physical spring assembly shown in Fig. 7.11, only for this experiment the attachment point of the virtual spring shown in Fig. 6.6 was also moved 6 cm so that real and virtual springs were attached to the same point. The virtual stiffness ($K_{vl} = 5250$ N/m), damping ($B_{vl} = 10$ Ns/m), and spring length ($l_{vl_0} = 0.3$ m) were also set to match the physical counterpart.
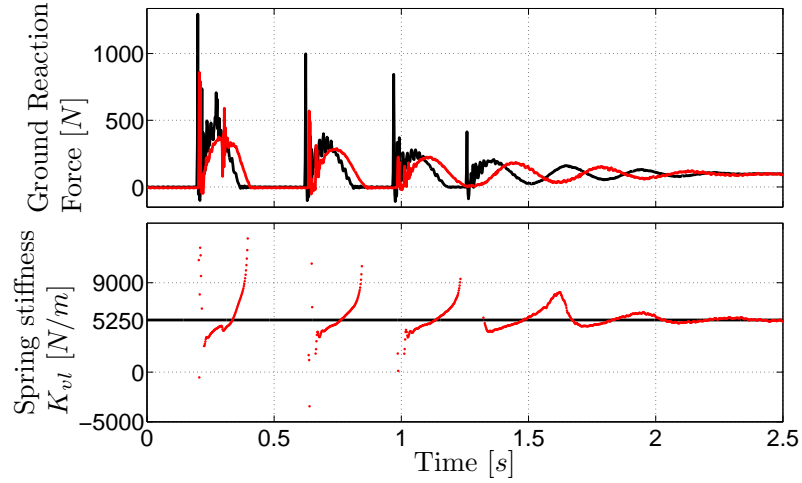
Figure 7.12: Comparison of the leg dynamics when dropping it from 25 cm using two different compliance approaches: active compliance by using a virtual spring-damper (red line), and passive compliance by using a real spring-damper (black line). In the first plot, the ground reaction forces show that both systems bounces with similar dynamics, being the impact forces smaller for the actively-compliant leg. In the second plot, it is shown how the virtual leg tracks the desired stiffness of the real spring ($K_{vl} = 5250$ N/m) during stance phase.

The impact forces and leg dynamics for both active and passive case are compared in the first plot of Fig. 7.12. It shows that the emulated spring-damper was able to qualitatively mimic the passive system. Small differences in the stance period suggest that the virtual spring (red line) had a smaller stiffness value than the real spring (black line). The smaller the stiffness the longer the stance phase. That hypothesis can be verified in the second plot, which shows the stiffness tracking. It evidences that during stance phase the stiffness is not constant, but it varies from about $K_{vl} = 4000$ N/m to $K_{vl} = 8000$ N/m. This imprecise stiffness tracking during

the impact, together with a possible non-ideal behavior of the real spring, can justify the slightly different dynamical behavior.

In addition, the real spring (black line) has a higher impact force (around 1300 N) than the virtual spring (about 800 N). This is a surprising result, since it was expected that factors such as actuator dynamics and sampling would delay the virtual spring reaction, thus increasing the impact forces. Nevertheless, the lower impact forces of the virtual stiffness demonstrated once again that HyQ compliance controller can be safely used in highly-dynamic applications. It evidences that it is possible to handle impact forces with no real springs or other compliant elements. The smaller impact force of the virtual spring can also be explained by its smaller stiffness at the moment of touch-down.

7.3.3   Active vs. Passive compliance

After presenting an experimental comparison between an active and a passive legged system, this section discusses some important aspects in the use of compliance in robotics and underlines the *pros & cons* of both passive and active compliance. Such analysis is of fundamental importance for robot designers which have to decide in favor of one or the other, or even in a mix of both.

First of all, it should be clear that active compliance uses energy for producing the desired impedance behavior. Thus, this energy consumption can be a limiting factor for employing active compliance on robots that aim to be energy efficient.

On the other hand, energy efficiency is one of the hallmarks of passive compliance. Components such as springs can store energy while being compressed (or extended). In springs, the stored energy is proportional to the stiffness and to the square of the spring displacement. Hence, to maximize this stored energy, it is interesting to prioritize the spring compression over its stiffness. For a given constant force, to increase the spring displacement it is necessary to reduce its stiffness.

However, small stiffness reduces the joint controllability, leading usually to poor position tracking and maybe to dangerous situations in the worst case. For this reason and also due to design constraints, higher stiffness configurations are often preferred even though the energy storage capability is reduced. In this case, the backdrivability and safety of the passive system is almost lost.

Also, when the energy stored in the spring is suddenly released, it can result in high speed motions of the robot, and correspondingly in a high risk for humans in case of collision [Vanderborght, 2010].

The application of passive compliance on a robot can be very cheap and simple. It can consist, for instance, of a simple layer of rubber at the end-effector or of a linear spring in series with it. However, more complex designs, as the VSAs, can substantially increase the costs and complexity of passive compliance.

Active compliance is usually more expensive to be employed than traditional passive compliance. It commonly requires more hardware expenses, such as force/torque sensors and data acquisition interfaces. Moreover, if the actively-compliant robot intends to perform highly-dynamic tasks, high-performance (and normally high-priced) hardware is needed, such as high-bandwidth actuators and fast computers.

Although active compliance can be energy inefficient and sometimes expensive, its use relies on a fundamental motivation: *versatility*. An actively-compliant robot can take advantage of any programmable type of impedance (e.g. exponential springs, nonlinear dampers, muscle-model-based springs, etc.). In this way, it is possible to considerably vary the dynamical robot behavior with no physical changes on it. For instance, the CoG dynamics could be set [Hyon, 2009] instead of the leg dynamics.

Section 6.2 showed that the higher the torque bandwidth, the smaller the achievable range of passive impedances. So, if a robot aims to enlarge its Z-width rather than achieving high impedance tracking performances, slower and usually cheaper actuators can be used for doing active compliance. However, if the physical similarity of the mimicked virtual elements has higher priority, then high-bandwidth closed-loop control should be used, as discussed in Section 6.3.

Even though the closed-loop bandwidth can be increased by the controller (within stability limits), fast actuators are essential for reaching good torque/force control performance. How good this performance has to be is defined by the requirements of the robot. In general, the faster the tasks that the robot has to accomplish, the better the tracking performance has to be. However, for many legged robots it is still not fully clear what this required performance is, and because of that many times "as fast as possible" becomes the answer for the actuator requirements.

The HyQ robot uses fast valves, with a bandwidth of about 250 Hz, for controlling the hydraulic flow [MOOG Inc., 2003]. Such valves are expensive but they allow to reach the force control performance shown in Fig. 5.9. HyQ also uses rubber feet, which are used to increase the traction and are the only compliant elements on the robot. Even though these compliant elements are not necessary, this minimum compliance gives the advantage of filtering high-frequency disturbance forces due to impacts during dynamic tasks (e.g. jumping and trotting).

A comparison between active and passive compliance was presented in Wang et al [Wang et al., 1998]. Extending his results, the main advantages and limitations of both ways of achieving compliance are summarize in Table 7.1.

Table 7.1: Passive vs. Active compliance

Passive Compliance	Active Compliance
Obtained by hardware	Obtained by software
Added inertia to the structure	No weight added to the structure
Unlimited range of passive impedances	Limited range of passive impedances
Unlimited bandwidth	Bandwidth limited by the closed-loop torque control
Possible to vary stiffness (with VSA's),but still slow	Fast change of apparent stiffness (minimum of 1 sampling time)
Possible to store energy	Active elements only consume energy
Hard to physically realize complex impedances profiles	Any programmable impedance can be easily realized
Usually cheap	Usually expensive

7.4 HyQ experiments

The high-performance compliance control presented in this work permitted other HyQ collaborators to perform several experiments with the robot to assess its capability to execute highly dynamic motions, its strength, and its mechanical robustness. For the sake of completeness, this section presents some of the works done by other HyQ collaborators which emphasize the usefulness of the compliance controller for legged locomotion. The implementation of a trot and a squat jump is briefly described and some experimental results are shown.

In these experiments, the force control approach is still the feedback linearization, but the compliance control uses only a PD with the inverse rigid body dynamics, as described in Section 6.1.1.

To overcome the intrinsic complexity related to floating-base robots such as under-actuation, dynamically changing contact states, and contact forces that may not be known, HyQ employs an orthogonal decomposition [Mistry et al., 2010] to calculate the floating base inverse dynamics.

7.4.1   Trot

A trot is characterized by synchronously moving diagonal leg pairs. The implementation of HyQ's trot is based on the desired end-effector position trajectories, which are then mapped into joint position reference trajectories by use of inverse kinematics. The foot follows a half-ellipsoid trajectory during the flight phase and a flat trajectory during the stance phase, as shown in the very right of Fig. 1.2b. The used trot frequency of $2Hz$ also matches values found in studies on running quadrupedal animals of comparable size [Heglund and Taylor, 1988].

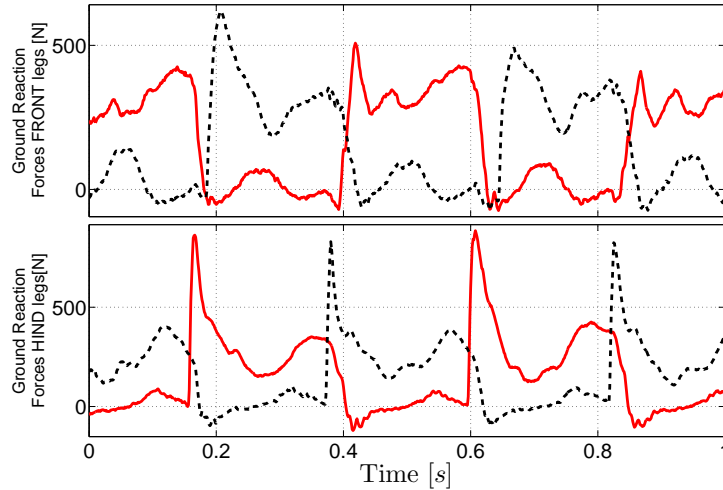**Figure 7.13:** Vertical ground reaction forces at the robot's feet during one second of a 2.25 Hz trot. The forces are obtained through the projection of the measured joint torques into Cartesian coordinates at the foot. Top: Front Left (red solid), Front Right (black dashed). Bottom: Hind Left (red solid) and Hind Right (black dashed) leg.

Fig. 7.13 shows vertical ground reaction forces at the four feet obtained from a

2.25 *Hz walking trot* at 1.7 *m/s* with a duty factor of 53%. The data is based on the joint torque measurements of the two hydraulic joints that are projected into Cartesian coordinates at the foot via the leg Jacobian matrix [Semini et al., 2011b]. The ground reaction forces at the feet of a running robot give important insights into each leg's contribution to the robot propulsion and the stress that the mechanical structure has to deal with.

The peak forward velocity of 1.7 *m/s* corresponds to a Froude number of 0.5, using the distance between the ground and the hip axis as characteristic leg length [Alexander, 2002]. As the robot is currently moving on a relatively narrow treadmill with respect to its size, faster velocities are dangerous to test. More recent outdoor running experiments, without the treadmill, reached 2 *m/s* [Barasuol et al., 2013].

During the experiments, for safety, two *robot wranglers* use laterally fixed ropes to monitor, and if needed, correct the robot's direction of motion to keep it on the treadmill. Experimental results with HyQ of a *running trot* with 36% duty factor are presented in [Semini et al., 2011a]. The on-board IMU is currently used for robot body state estimation, and also for active control of roll, pitch and yaw [Barasuol et al., 2013].

7.4.2 Squat jump

The next experiment demonstrates the speed and force of HyQ's legs, as well as the robots ability to cope with impacts during landing. Additionally, it shows the capabilities and benefits of torque controlled joints and rigid body model-based control and their importance for highly dynamic robots. More details about this experiment can be found in [Semini et al., 2012].

Starting from a squat posture, the robot pushes its body 0.36 *m* upward vertically to the ground plane until it lifts off the ground after about 0.35 *s*. Once the robot is in its parabolic flight phase the legs are repositioned to prepare for the landing. To achieve compliant behavior during the impact of the landing low knee position gains of $K_p = 200 \ Nm/rad$ were used.

To demonstrate the contribution of the feed-forward torques $\boldsymbol{\tau_{ff}}$ obtained by the inverse dynamics (see Section 6.1.1), the same jump was performed with and without inverse dynamics during the acceleration phase. Fig. 7.14a shows the resulting position and force tracking performance with the inverse dynamics control switched

on, and Fig. 7.14b shows the results with the same controller switched off. These two plots show how the inverse dynamics' contribution improved position tracking before the jump (0 to 0.2 s in the plot) and especially during the vertical acceleration (0.2 to 0.55 s), even though the position gains K_p were low.

(a) Inverse dynamics *on*   **(b)** Inverse dynamics *off*
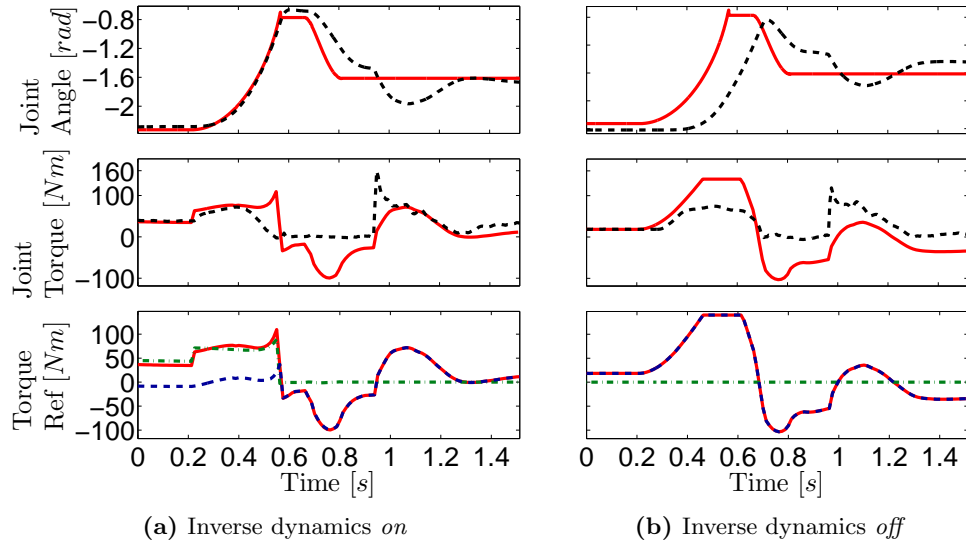
Figure 7.14: Position and force tracking of the right hind knee joint during a squat jump. (a) inverse dynamics switched on during the acceleration phase. (b): inverse dynamics switched off. The first plot shows the acceleration phase (from $t = 0.2s$ to $0.55s$) with consecutive landing preparation. The parabolic flight phase lasts from $0.55s$ to $0.95s$. In the first two plots, the red solid lines indicate the reference command and the black dashed ones the actual value. The last plot shows how the reference torque τ_{ref} is generated (as in the last plot of Fig. 6.3)

The resulting jump lifts the robot's CoG about 0.2 m from its position when the robot loses contact with the ground. Peak knee joint velocity reaches 11 rad/s at the end of the acceleration phase. The low position gains act as virtual rotational springs that create a compliant landing. The impact torque peaks are kept at safe levels ($< 160\ Nm$) and thus protect the mechanical structure of the robot. Note that no mechanical springs are present anywhere on the legs, but only a layer of 5 mm visco-elastic rubber at the feet to increase traction. Only a high-performance active compliance control in combination with the mechanical robustness of the actuators make this kind of tasks possible to be accomplished by a robot with no springs in it!

Chapter 8

Conclusion and Future Work

This thesis showed that there is no mystery behind high-performance compliance control, but that through appropriate modeling and model-based control techniques such high performance can be achieved. Many relevant aspects regarding the control and design of suitable force and compliance control architectures for robotics applications were presented. This section summarizes the most important issues discussed throughout the thesis.

The main goal of this thesis was to develop a model-based controller for the torque and compliance of the hydraulically-actuated quadruped robot HyQ (Fig. 1.2a). Before presenting the controllers, however, this thesis explained, in Chapter 3, important details about the hydraulic actuation. It is essential to understand the dynamics, advantages, and limitations of the selected actuation system before attempting to control it.

The hydraulic actuation was chosen for driving HyQ mainly because it is strong and fast. In addition, it is mechanically very simple and robust. No gearboxes are necessary for increasing the torque capabilities. Hydraulic actuators can handle high impact forces at the foot more robustly than geared electric motors.

The main drawback of the hydraulic actuation is the low energy efficiency. To guarantee fast responses, HyQ employs high-bandwidth valves. This high-bandwidth comes at a price of a high internal leakage inside the valve, which results in a power loss of about $0.8\ kW$ for the whole robot. However, due to the significant advantages of this actuation, the low energy efficiency is tolerable for HyQ. To improve the energy efficiency is a further work in the development of the robot.

As discussed in Section 7.2, in hydraulics the oil is the element which transmits pressure, and consequently force, to the load. Due to the very low compressibility of the oil, this transmission can be very stiff. The stiffness of the hydraulic transmission depends mainly on the amount of oil that connects the servovalve to the actuator chambers. The more oil, the softer the transmission. Furthermore, this stiffness varies nonlinearly according to the piston position, as depicted in Fig. 7.7. The pipeline also plays an important role on the transmission stiffness. Rigid tubes keep the system stiffer, while flexible hoses tend to reduce the transmission stiffness.

For any actuation system, the stiffer the transmission element the faster the open-loop force dynamics. Therefore, when closing a force control loop, systems with stiffer transmissions tend to obtain better closed-loop performances. For instance, the electric motors used in the HyQ HAA joint (see Fig. 1.2b) employ harmonic drives with stiffness of about $K_{te} = 2.7 \cdot 10^4 \ Nm/rad$, while the hydraulic cylinders of the HFE and KFE have a minimum stiffness of around $K_{th} = 1.0 \cdot 10^7 \ N/m$. This higher hydraulic transmission stiffness is one of the reasons for obtaining a faster closed-loop force response with hydraulic actuators than electric ones.

This thesis also showed in Chapter 4 that, due to causality reasons, force is always transmitted over a transmission that is deformable, that is, an element with finite stiffness. The compression of this transmission, and consequently the creation of the force, depends not only on the actuator dynamics but also on the load dynamics. The influence of the load on the force dynamics is a physical property that has to do with the application of forces to bodies, regardless of the source of these forces. Even though this concept is very important in force control, there is not much information on the literature about it. This thesis aimed to cover this lack by proposing a novel and generic framework for representing and modeling the force dynamics. This framework was applied to both the hydraulic and electric actuation system of HyQ, highlighting that the framework is generic and does not depend on the actuation system. This framework emphasizes both the transmission stiffness as well as the natural feedback of the load velocity in the force modeling. This intrinsic load velocity feedback introduces a low-frequency zero in the open-loop force transfer function which can seriously limit the performance of a closed-loop force control.

A force sensor measures the reaction forces applied to it, as discussed in Section 7.1.1. These reaction forces can derive for instance from friction, gravity, or inertia.

These elements create counter forces that oppose the motion of the actuator, creating then a reaction force that is measured by the force sensor. The higher the total counter forces acting on a system, the bigger the range of forces this system can achieve. Practically, the robot's joints close to the base will always present better force control performance than the joints close to the end-effector. This is due to the negative gradient of the reflected inertia from the base to end-effector.

As for the inertia, the higher the viscous friction the better the force control performance. To intentionally increase the viscous friction of the low-inertia links of a robot, especially the ones close to the end-effector, might be an interesting solution for increasing the force control performance of those links at the price of energy loss.

Based on the information about the hydraulic actuation and about important physical properties in force dynamics, such as the load velocity feedback, a series of force controllers were proposed in Chapter 5. It was shown that a traditional feedback-based PID behaves similarly to a PD due to the low-frequency zero introduced by the load dynamics. This effect is accentuated in low-inertia and low-damping cases. A model-based feed forward controller which compensates for the load velocity feedback was then proposed to eliminate the influence of this inconvenient zero in the transfer function and consequently increase the force tracking capabilities. A nonlinear model-based feedback linearization controller was also designed to compensate not only for the load velocity feedback but also for the pressure nonlinearities.

The design of a high-performance force controller permitted to transform HyQ's joints into high-fidelity torque sources. This was a key step to implement a compliance controller that was able to provide a desired dynamic behavior to the robot. Four different approaches for controlling the robot compliance were designed, as shown in Chapter 6, and implemented on HyQ. A feedback-based position PD controller, together with a rigid body inverse dynamics feed forward term, is a simple and elegant solution which permits the robot to simultaneously track reference trajectories and be compliant to external perturbations. This model-based compliance control approach is very effective and has been used in the HyQ robot in most of the tasks.

A virtual model controller was used to set a desired dynamic behavior to the robot through the emulation of virtual components. These virtual components al-

low to easily vary the dynamical behavior of the system on-the-fly, using physical intuition and without changing the mechanical characteristics of the robot.

To ensure stable interactions with passive environments, an actively-compliant legged robot should always behave passively at the contact point. The range of achievable impedances that can be passively emulated at the contact point (Z-width) depends on many aspects, such as sampling frequency and signal filtering. This thesis showed, in Section 6.2, that also the inner torque controller has a strong effect on the Z-width: the higher the torque gains, the smaller the Z-width. Thus, the highest possible closed-loop torque bandwidth might not be the best solution for all situations, since it can limit the achievable range of impedances and consequently the versatility of the robot. However, to enhance the robot's capability of tracking a desired compliant behavior, high-bandwidth torque controllers should be preferred. In this case, the Z-width could be enlarged for instance by using a faster actuator or by intentionally increasing the damping at the robot joints. All these aspects highlight that both the hardware and the controllers have to be carefully designed to balance performance with stability issues.

Last but not least, having such torque-controlled machines will lead to a better understanding of how to build future robots, which might be more application-specific instead of versatile and and make use of passive elements to gain energy efficiency.

8.1 Future Work

The work presented in this thesis is only a small part of larger research effort that is being performed by the HyQ group to evolve the robot as a whole.

This section suggests a list of future works that should be carried out mainly in the area of actuation and control to improve the robot performance and capabilities:

- Establish a method for choosing the most suitable stiffness for the robot according to the task requirements. An adaptive compliance controller could be developed.

- Design a gain scheduling according to the load status of the leg. For instance, during stance phase, when the leg is loaded with the robot weight, the force

gains could be set higher than when the leg is in the air and the low inertia of the link restricts the force control performance.

- Design a robust and adaptive control for the low-level hydraulic force control since some parameters are difficult to estimate or even change during the robot task, like the viscosity of the oil that is highly dependent on its temperature. These controllers could increase the stability margins and consequently the robustness and performance of the system.

- Increase the sampling frequency (oversampling) of the force signal. With a higher sampling frequency an averaging (or more sophisticated) filter could be used to reduce the load cell noise with no significant time delays.

- Linearize the torque dynamics instead of the load force dynamics. The nonlinearity of the lever arm could be fully compensated for in the low-level control.

- Develop an accurate model for the viscous friction in the hydraulic cylinders. A more detailed model could be used in the model-based controller.

- In case pressure sensors are available at the cylinder chambers, to close an inner pressure control loop inside the torque loop.

- Extend the model-based force controllers for rotary hydraulic actuators.

- Implement the virtual model control approach for the robot CoG. It might be easier and more intuitive to set the robot behavior as a whole using the abstraction of having virtual components attached to the robot CoG instead of the legs.

- Analyze deeply the influence of the load velocity compensation in the outer compliance loop, the influence when stiffness is added to the load, the influence of the stiffness of the force sensor, and also extend the framework to MIMO systems.

- Implement the full impedance control for the HyQ legs, where also a desired mass can be set to the end-effector.

8. CONCLUSION AND FUTURE WORK

- Investigate the influence of different actuator bandwidths on the force and compliance control performance and stability.

- Evaluate valves that are more energy efficient, but have a lower bandwidth.

- Generalizing some of the results to floating-base systems.

Appendix A

Curriculum Vitae

Thiago Boaventura Cunha

Istituto Italiano di Tecnologia (IIT)

Advanced Robotics Department

Brazilian, September 14th, 1985

thiago.boaventura@iit.it

Education

2010–today	**PhD Candidate in Robotics, Cognition and Interaction Technologies**
	Italian Institute of Technology (IIT) and University of Genoa, Italy
2004–2009	Bachelor and Master Degree in Control and Automation Engineering
	Federal University of Santa Catarina (UFSC), Brazil

Summer Schools

2012	Soft Robotics (40 hours) @ ETH Zurich, Switzerland
	Screw-Theory Based Methods in Robotics (50 hours) @ University of Genoa, Italy
2011	Dynamic Walking & Running with Robots (40 hours) @ ETH Zurich, Switzerland

Research experience

2010–today	**HyQ Project: PhD candidate and researcher** Focus on the low-level control of the hydraulic quadruped robot HyQ. The main activities involve the actuation modeling and control design. Hands-on experience in the robot assembly, maintenance, and experiments. Linear and non-linear approaches have been investigated for both position and torque control on hydraulic actuators. Other control approaches such as virtual model control, impedance control, and operational space control have also been implemented.
2009–2010	**Master Thesis: Modelling and Control of a Hydraulic Quadruped Robot Leg** Modelling of linear hydraulic actuation and linear position control design (PID, LQR, Gain Scheduling) of the first version of the HyQ leg. Supervisors: Dr. Emanuele Guglielmino, Prof. Dr. Victor Juliano De Negri, Dr. Claudio Semini Department of Advanced Robotics, Italian Institute of Technology, Genoa, Italy and Federal University of Santa Catarina, Brazil
2006–2009	**Laboratory of Hydraulic and Pneumatic Systems (LA-SHIP): undergraduate research** Redesign and automation of a hydraulic power and conditioning unit, CAD design of a didactic equipment set for pneumatic circuits sizing and automation. Practical experience with hydraulic circuits assembly, tunning and testing, PLC programming. Supervisor: Dr. Victor Juliano De Negri LASHIP, Federal University of Santa Catarina, Brazil

Publications

2013	**T. Boaventura**, C. Semini, J. Buchli, and D. G. Caldwell, "Practical issues in hydraulic compliance control," in *Workshop in Design and Control of High- Performance Hydraulic Robots: Recent Advances and Perspectives, IEEE International Conference in Robotics and Automation (ICRA)*, 2013 (accepted for pubblication)

2012   **T. Boaventura**, M. Focchi, M. Frigerio, J. Buchli, C. Semini, G. Medrano-Cerda, and D. Caldwell, "On the role of load motion compensation in high-performance force control," in *Intelligent Robots and Systems (IROS), 2012 IEEE/RSJ International Conference on*, oct. 2012, pp. 4066–4071 , [full article]

T. Boaventura, C. Semini, J. Buchli, M. Frigerio, M. Focchi, and D. G. Caldwell, "*Dynamic torque control of a hydraulic quadruped robot*," in IEEE International Conference in Robotics and Automation (ICRA), 2012, pp. 1889–1894 , [full article]

M. Focchi, **T. Boaventura**, C. Semini, M. Frigerio, J. Buchli, and D. G. Caldwell, "Torque-control based compliant actuation of a quadruped robot," in *Proc. of the 12th IEEE Int. Workshop on Advanced Motion Control (AMC)*, 2012 , [full article]

C. Semini, H. Khan, M. Frigerio, **T. Boaventura**, M. Focchi, J. Buchli, and D. G. Caldwell, "Design and scaling of versatile quadruped robots," in *Int. Conf. on Climbing and Walking Robots (CLAWAR)*, 2012 , [full article]

S. Peng, D. T. Branson, E. Guglielmino, **T. Boaventura**, and D. G. Caldwell, "Performance assessment of digital hydraulics in a quadruped robot leg," in *Proceedings of the 11th Biennial Conference on Engineering Systems design and Analysis (ESDA11)*, 2012, [full article]

2011   **T. Boaventura**, C. Semini, J. Buchli, and D. G. Caldwell, "Actively-compliant leg for dynamic locomotion," in *Int. Symp. Adaptive Motion of Animals and Machines (AMAM)*, 2011, [full article]

C. Semini, J. Buchli, M. Frigerio, **T. Boaventura**, M. Focchi, E. Guglielmino, F. Cannella, N. G. Tsagarakis, and D. G. Caldwell, "HyQ – a dynamic locomotion research platform," in *Int. Workshop on Bio-Inspired Robots, Nantes (France)*, 2011, [full article]

2010 | M. Focchi, E. Guglielmino, C. Semini, **T. Boaventura**, Y. Yang, and D. G. Caldwell, "Control of a hydraulically-actuated quadruped robot leg," in *Proceedings of the IEEE International Conference on Robotics and Automation (ICRA)*, 2010, [full article]

Y. Yang, E. Guglielmino, J. S. Dai, **T. Boaventura**, and D. G. Caldwell, "Modeling of a novel 3-way rotary type electro-hydraulic valve," in *Proc. IEEE Int Information and Automation (ICIA) Conference*, 2010, pp. 1463–1468, [full article]

T. Boaventura, C. Semini, E. Guglielmino, V. J. De Negri, Y. Yang, and D. G. Caldwell, "Gain scheduling control for the hydraulic actuation of the hyq robot leg," in *ABCM Symposium Series in Mechatronics*, Rio de Janeiro, RJ, Brazil, 2010, vol. 4, pp. 673–682, iSBN 978-85-85769-47-5, [full article]

Y. E. A. Mendonza, M. Hen, **T. Boaventura**, and D. Negri, "Development of a didactic equipment for pneumatic component sizing," in *ABCM Symposium Series in Mechatronics*, Rio de Janeiro, RJ, Brazil, 2010, vol. 4, pp. 934–943, iSBN 978-85-85769-47-5, [full article]

Appendix B

Force feedback linearization using Lie derivative

This appendix presents the design of a force feedback linearization controller based on the traditional Lie derivatives approach.

The load force model, presented in Eq. 3.19 can be rewritten as:

$$\begin{cases} \dot{x} = f(x) + g(x)u_v \\ y = h(x) \end{cases} \tag{B.1}$$

where x is the following state vector:

$$x = \begin{bmatrix} x_p \\ \dot{x}_p \\ p_a \\ p_b \end{bmatrix} \tag{B.2}$$

Considering $u_v > 0$, the system in Eq. B.1 can be written as:

$$\begin{cases} \dot{x} = \begin{bmatrix} \dot{x}_p \\ \ddot{x}_p \\ -\frac{\beta_e A_p \dot{x}_p}{v_a} \\ \frac{\alpha \beta_e A_p \dot{x}_p}{v_b} \end{bmatrix} + \begin{bmatrix} 0 \\ 0 \\ \frac{\beta_e K_v \sqrt{p_s - p_a}}{v_a} \\ -\frac{\beta_e K_v \sqrt{p_b - p_t}}{v_b} \end{bmatrix} u_v \\ y = A_p p_a - \alpha A_p p_b - B \dot{x}_p \end{cases} \tag{B.3}$$

Then, the following Lie derivatives can be obtained:

B. FORCE FEEDBACK LINEARIZATION USING LIE DERIVATIVE

$$L_g h(x) = \frac{\partial h(x)}{\partial x} g(x) = \begin{bmatrix} 0 & -B & A_p & -\alpha A_p \end{bmatrix} \begin{bmatrix} 0 \\ 0 \\ \frac{\beta_e K_v \sqrt{p_s - p_a}}{v_a} \\ -\frac{\beta_e K_v \sqrt{p_b - p_t}}{v_b} \end{bmatrix} =$$
$$= A_p \frac{\beta_e K_v \sqrt{p_s - p_a}}{v_a} + \alpha A_p \frac{\beta_e K_v \sqrt{p_b - p_t}}{v_b} \tag{B.4}$$

$$L_f h(x) = \frac{\partial h(x)}{\partial x} f(x) = \begin{bmatrix} 0 & -B & A_p & -\alpha A_p \end{bmatrix} \begin{bmatrix} \dot{x}_p \\ \ddot{x}_p \\ -\frac{\beta_e A_p \dot{x}_p}{v_a} \\ \frac{\alpha \beta_e A_p \dot{x}_p}{v_b} \end{bmatrix} =$$
$$= -B\ddot{x}_p - A_p \frac{\beta_e A_p \dot{x}_p}{v_a} - \alpha A_p \frac{\alpha \beta_e A_p \dot{x}_p}{v_b} \tag{B.5}$$

It is possible to verify that the system has relative degree of $r = 1$ by doing the following checking:

$$L_g L_f h(x) = \frac{\partial L_f h(x)}{\partial x} g(x) = 0 \tag{B.6}$$

Finally, the control output u_{FL} can be defined as:

$$u_{FL} = \frac{1}{L_g L_f{}^{r-1} h(x)} (-L_f h^r(x) + v) \tag{B.7}$$

It can be noticed that $L_g h(x)$ is identical to $g(P, x_p)$ in Eq. 5.10, and that $L_f h(x)$ is identical to $f(x_p, \dot{x}_p, \ddot{x}_p)$ in Eq. 5.9. Thus, it becomes clear that Eq. B.7 is exactly identical to Eq. 5.11.

Appendix C

Virtual leg stiffness represented at Cartesian space

This appendix presents the representation of the virtual spring stiffness K_{vl} at the end-effector space. By default, the stiffness K_{vl}, and consequently the force f_{vl}, are defined always in the direction of the virtual leg, depicted by a green bar in Fig. C.1.
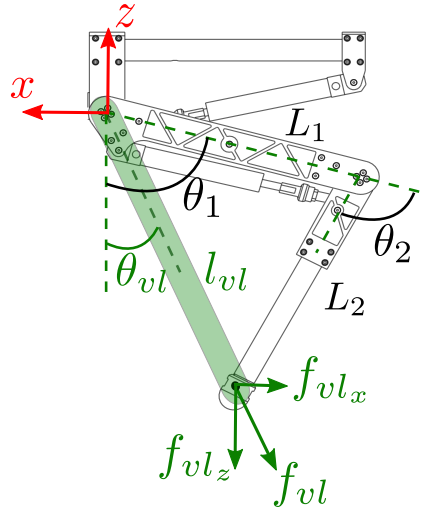
Figure C.1: This figure shows the abstraction of a *virtual leg*, depicted by a green bar, which has virtual characteristics such as stiffness K_{vl}, damping B_{vl}, and length l_{vl}. The virtual leg angle θ_{vl} is defined with respect to a vertical line. The joint angles θ_1 and θ_2, as well as the link lengths L_1 and L_2 are depicted in black. The reference axis is shown in red.

The virtual force vector $\vec{f_{vl}}$ can be decomposed in the axis frame as follows:

C. VIRTUAL LEG STIFFNESS REPRESENTED AT CARTESIAN SPACE

$$\vec{f}_{vl} = K_{vl}\delta\vec{l}_{vl} \ \Rightarrow \ \begin{array}{rcl} \vec{f_{vl_x}} = K_{vl} \ sin(\theta_{vl}) \ \delta\vec{l_{vl_x}} & = & k_{vlx} \ \delta\vec{l_{vl_x}} \\ \vec{f_{vl_z}} = K_{vl} \ cos(\theta_{vl}) \ \delta\vec{l_{vl_z}} & = & k_{vlz} \ \delta\vec{l_{vl_z}} \end{array} \tag{C.1}$$

where,

k_{vlx}: equivalent virtual leg stiffness in the x axis ($k_{vlx} = K_{vl} \ sin(\theta_{vl})$) $[N/m]$

k_{vlz}: equivalent virtual leg stiffness in the z axis ($k_{vlz} = K_{vl} \ cos(\theta_{vl})$) $[N/m]$

$\delta\vec{l_{vl_x}}$: equivalent virtual leg displacement vector in the x axis $[m]$

$\delta\vec{l_{vl_z}}$: equivalent virtual leg displacement vector in the z axis $[m]$

As seen in Eq. C.1, the constant virtual leg stiffness K_{vl} is equivalent, in Cartesian space, to a stiffness that is not constant but dependent on the virtual leg angle θ_{vl}.

To obtain θ_{vl} as a function of the joint angles θ_1 and θ_2, the coordinates of the end-effector represented in the axis frame are needed:

$$\begin{array}{l} x = -L_1 sin(\theta_1) - L_2 sin(\theta_1 + \theta_2) \\ z = -L_1 cos(\theta_1) - L_2 cos(\theta_1 + \theta_2) \end{array} \tag{C.2}$$

Then, according to Fig. C.1 and considering Eq. C.2, the angle θ_{vl} can be easily represented as:

$$tan(\theta_{vl}) \ = \ \frac{x}{z} \ \Rightarrow \ \theta_{vl} = tan^{-1}\left(\frac{-L_1 sin(\theta_1) - L_2 sin(\theta_1 + \theta_2)}{-L_1 cos(\theta_1) - L_2 cos(\theta_1 + \theta_2)}\right) \tag{C.3}$$

With the definition of the virtual leg angle θ_{vl} in terms of the joints angles θ_1 and θ_2, it is possible to compute the equivalent stiffnesses k_{vlx} and k_{vlz}:

$$\begin{array}{l} k_{vlx} = K_{vl} \ sin\left(tan^{-1}\left(\frac{-L_1 sin(\theta_1) - L_2 sin(\theta_1+\theta_2)}{-L_1 cos(\theta_1) - L_2 cos(\theta_1+\theta_2)}\right)\right) \\ k_{vlz} = K_{vl} \ cos\left(tan^{-1}\left(\frac{-L_1 sin(\theta_1) - L_2 sin(\theta_1+\theta_2)}{-L_1 cos(\theta_1) - L_2 cos(\theta_1+\theta_2)}\right)\right) \end{array} \tag{C.4}$$

References

Albu-Schäffer, A. and Hirzinger, G. (2002). Cartesian impedance control techniques for torque controlled light-weight robots. In *Proceedings IEEE International Conference on Robotics and Automation (ICRA)*, volume 1, pages 657 – 663. 16, 85

Alexander, R. M. (2002). *Principles of Animal Locomotion*. Princeton University Press. 126

Alleyne, A. and Hedrick, J. (1995). Nonlinear adaptive control of active suspensions. *IEEE Transactions on Control Systems Technology*, 3(1):94 –101. 20

Alleyne, A., Liu, R., and Wright, H. (1998). On the limitations of force tracking control for hydraulic active suspensions. In *Proceedings of the American Control Conference*, volume 1, pages 43 –47 vol.1. 19, 63

Anderson, B. D. O. and Vongpanitlerd, S. (1973). *Network Analysis and Synthesis – A Modern Systems Theory Approach*. Prentice-Hall, Englewood Cliffs, NJ. p. 548. 90

Armstrong-Hélouvry, B., Dupont, P., and Canudas de Wit, C. (1994). A survey of models, analysis tools and compensation methods for the control of machines with friction. *Automatica*, 30(7):1083–1138. 38

Ayalew, B. and Kulakowski, B. (2006). Cascade tuning for nonlinear position control of an electrohydraulic actuator. In *American Control Conference*, page 6 pp. 20

Barasuol, V., Buchli, J., Semini, C., Frigerio, M., De Pieri, E., and Caldwell, D. (2013). A reactive controller framework for quadrupedal locomotion on challenging

REFERENCES

terrain. *IEEE International Conference in Robotics and Automation (ICRA)*. [Accepted for publication]. 126

Blickhan, R. (1989). The spring-mass model for running and hopping. *Journal of Biomechanics*, 22(11–12):1217–1227. 84

Boaventura, T., Focchi, M., Frigerio, M., Buchli, J., Semini, C., Medrano-Cerda, G., and Caldwell, D. (2012a). On the role of load motion compensation in high-performance force control. In *IEEE/RSJ International Conference on Intelligent Robots and Systems (IROS)*, pages 4066 –4071. 19, 49, 69

Boaventura, T., Semini, C., Buchli, J., and Caldwell, D. G. (2011). Actively-compliant leg for dynamic locomotion. In *Int. Symp. Adaptive Motion of Animals and Machines (AMAM)*. 84

Boaventura, T., Semini, C., Buchli, J., Frigerio, M., Focchi, M., and Caldwell, D. G. (2012b). Dynamic torque control of a hydraulic quadruped robot. In *IEEE International Conference in Robotics and Automation (ICRA)*, pages 1889–1894. 13, 17, 21, 56, 60, 74

BostonDynamics, C. (2011). PETMAN. Accessed March 2013. Press release information. 13

Buchli, J., Kalakrishnan, M., Mistry, M., Pastor, P., and Schaal, S. (2009). Compliant quadruped locomotion over rough terrain. In *Proceedings of IEEE/RSJ International Conference on Intelligent Robots and Systems (IROS)*, pages 814–820. 17, 59, 79

Cannon, R. H. J. and Schmitz, E. (1984). Initial experiments on the end-point control of a flexible one-link robot. *International Journal of Robotics Research*, 3 No. 3:62–75. 18

Clark, D. (1969). Selection and performance criteria for electrohydraulic servodrives. In *Proceedings of the 25th annual meeting of the national Conference on Fluid Power*. Reprint in Moog technical bulletin #122. 7

Colgate, E. and Hogan, N. (1989). An analysis of contact instability in terms of passive physical equivalents. In *IEEE International Conference on Robotics and Automation (ICRA)*, pages 404–409 vol.1. 89

Colgate, J. E. (1994). Coupled stability of multiport systems – theory and experiments. *Transactions of ASME, Journal of Dynamic Systems, Measurement , and Control*, 116:419–428. 90

Colgate, J. E. and Brown, J. M. (1994). Factors affecting the z-width of a haptic display. In *IEEE International Conference on Robotics and Automation (ICRA)*, pages 3205–3210. 22, 91

Colgate, J. E. and Schenkel, G. G. (1997). Passivity of a class of sampled-data systems: Application to haptic interfaces. *Journal of Robotic Systems*, 14(1):37–47. 22, 91, 92

Conrad, F. and Jensen, C. (1987). Design of hydraulic force control systems with state estimate feedback. In *IFAC 10th Triennial Congress*, pages 307–31, Munich, Germany. 19

Davliakos, I. and Papadopoulos, E. (2007). Model-based position tracking control for a 6-dof electrohydraulic stewart platform. In *Mediterranean Conference on Control Automation*, pages 1 –6. 20

De Negri, V., Ramos Filho, J., and Souza, A. (2008). A design method for hydraulic positioning systems. In *Proceedings of the 51th National Conference on Fluid Power (NCFP) in conjunction with IFPE, Las Vegas, USA.*, pages 669–679. 31

Dhaouadi, R., Kubo, K., and Tobise, M. (1993). Analysis and compensation of speed drive systems with torsional loads. In *Proceedings of the Power Conversion Conference*, pages 271–277. Yokohama. 20

Dimig, J., Shield, C., French, C., Bailey, F., and Clark, A. (1999). Effective force testing: A method of seismic simulation for structural testing. *Journal of Structural Engineering*, 125(9):1028–1037. 19

REFERENCES

Dyke, S., Spencer Jr., B., Quast, P., and Sain, M. (1995). Role of control-structure interaction in protective system design. *Journal of Engineering Mechanics, ASCE*, 121 No.2:322–38. 19, 51

Estremera, J. and Waldron, K. J. (2008). Thrust control, stabilization and energetics of a quadruped running robot. *International Journal of Robotics Research*, 27:1135–1151. 15

Farley, C. and Taylor, C. (1991). A mechanical trigger for the trot-gallop transition in horses. *Science*, 253:306–308. 22

Featherstone, R. and Orin, D. (2000). Robot dynamics: equations and algorithms. In *IEEE International Conference on Robotics and Automation (ICRA)*, volume 1, pages 826 –834 vol.1. 58, 59

Ferris, D. P., Louie, M., and Farley, C. T. (1998). Running in the real world: adjusting leg stiffness for different surfaces. *Proc. R. Soc. Lond. B*, 265:989–994. 21

Focchi, M., Boaventura, T., Semini, C., Frigerio, M., Buchli, J., and Caldwell, D. G. (2012). Torque-control based compliant actuation of a quadruped robot. In *Proceedings of the 12th IEEE Int. Workshop on Advanced Motion Control (AMC)*. 55, 74, 85, 87, 116

Franklin, G. (1993). *Feedback Control of Dynamic Systems*. Addison-Wesley Longman Publishing, Boston, 3rd edition. 113

Garry W. Krutz, P. S. K. C. (2004). Water hydraulics – theory and applications. In *Workshop on Water Hydraulics, Agricultural Equipment Technology Conference (AETC'04)*, pages 1–33. 24

Grebenstein, M., Albu-Schaffer, A., Bahls, T., Chalon, M., Eiberger, O., Friedl, W., Gruber, R., Haddadin, S., Hagn, U., Haslinger, R., Hoppner, H., Jorg, S., Nickl, M., Nothhelfer, A., Petit, F., Reill, J., Seitz, N., Wimbock, T., Wolf, S., Wusthoff, T., and Hirzinger, G. (2011). The dlr hand arm system. In *IEEE International Conference on Robotics and Automation (ICRA)*, pages 3175 –3182. 18

Hahn, H., Piepenbrink, A., and Leimbach, K.-D. (1994). Input/output linearization control of an electro servo-hydraulic actuator. In *Proceedings of the Third IEEE Conference on Control Applications*, pages 995 –1000 vol.2. 20

Ham, R., Sugar, T., Vanderborght, B., Hollander, K., and Lefeber, D. (2009). Compliant actuator designs. *Robotics Automation Magazine, IEEE*, 16(3):81–94. 18

Hawker, G. and Buehler, M. (2000). Quadruped trotting with passive knees - design, control, and experiments. In *Proceedings of the International Conference on Robotics and Automation (ICRA)*. 15

Heglund, N. and Taylor, C. (1988). Speed, stride frequency and energy cost per stride: how do they change with body size and gait? *Journal of Experimental Biology*, 138(1):301–318. 125

Hirai, K., Hirose, M., Haikawa, Y., and Takenaka, T. (1998). The development of honda humanoid robot. In *Proceedings of the IEEE International Conference on Robotics and Automation (ICRA)*, volume 2, pages 1321 –1326 vol.2. 15

Hogan, N. (1985a). Impedance control - an approach to manipulation. i - theory. ii - implementation. iii - applications. *ASME, Transactions, Journal of Dynamic Systems, Measurement, and Control*, 107:1–24. 57

Hogan, N. (1985b). Impedance control: An approach to manipulation: Part I – Theory. *ASME, Transactions, Journal of Dynamic Systems, Measurement, and Control*, 107:1–7. 16, 50

Hogan, N. (1985c). Impedance control: An approach to manipulation: Part II – Implementation. *ASME, Transactions, Journal of Dynamic Systems, Measurement, and Control*, 107:8–16. 16, 21, 57, 85, 86, 87, 88

Hollerbach, J., Hunter, I., and Ballantyne, J. (1992). *The Robotics Review 2*, chapter A comparative analysis of actuator technologies for robotics, pages 299–342. MIT Press. 7

Hori, Y., Iseki, H., and Sugiura, K. (1994). Basic consideration of vibration suppression and disturbance rejection control of multi-inertia system using sflac (state

REFERENCES

feedback and load acceleration control). *IEEE Transactions on Industry Applications*, 30(4):889–896. 20

Hoyt, D. and Taylor, R. (1981). Gait and the energetics of locomotion in horses. *Nature*, 292:239–240. 73

Hurst, J. W. (2011). The electric cable differential leg: a novel design approach for walking and running. *International Journal of Humanoid Robotics*, 8(2):301–321. 7

Hurst, J. W., Hobbelen, D., and Rizzi, A. (2004). Series elastic actuation: Potential and pitfalls. In *Proceedings of the International Conference on Climbing and Walking Robots (CLAWAR)*. 19

Hutter, M., Gehring, C., Bloesch, M., Hoepflinger, M., Remy, C. D., and R., S. (2012). Starleth: A compliant quadrupedal robot for fast, efficient, and versatile locomotion. In *Proc. of the International Conference on Climbing and Walking Robots (CLAWAR)*. 15

Hutter, M., Remy, C., Hopflinger, M., and Siegwart, R. (2010). Slip running with an articulated robotic leg. In *IEEE/RSJ International Conference on Intelligent Robots and Systems (IROS)*, pages 4934 –4939. 84

Hyon, S. (2009). Compliant terrain adaptation for biped humanoids without measuring ground surface and contact forces. *IEEE Transactions on Robotics*, 25(1):171–178. 123

Janabi-Sharifi, F., Hayward, V., and Chen, C.-S. (2000). Discrete-time adaptive windowing for velocity estimation. *IEEE Transactions on Control Systems Technology*, 8(6):1003 –1009. 22, 91, 92, 97

Jelali, M. and Kroll, A. (2003). *Hydraulic Servo-systems. Modelling, Identification and Control.* Springer. 25, 36, 41

Kalakrishnan, M., Buchli, J., Pastor, P., Mistry, M., and Schaal, S. (2011). Learning, Planning, and Control for Quadruped Locomotion over Challenging Terrain. *International Journal of Robotics Research*, 30:236–258. 15

Kaneko, K., Suzuki, N., Ohnishi, K., and Tanie, K. (1991). High stiffness torque control for a geared dc motor based on acceleration controller. In *Proc. IECON '91. Conf. Int Industrial Electronics, Control and Instrumentation*, pages 849–854. 20

Kazerooni, H., Houpt, P., and Sheridan, T. (1986a). Robust compliant motion for manipulators, part ii: Design method. *IEEE Journal of Robotics and Automation*, 2(2):93–105. 16

Kazerooni, H., Sheridan, T., and Houpt, P. (1986b). Robust compliant motion for manipulators, part i: The fundamental concepts of compliant motion. *IEEE Journal of Robotics and Automation*, 2(2):83–92. 16

Khatib, O. (1987). A unified approach for motion and force control of robot manipulators: The operational space formulation. *IEEE Journal of Robotics and Automation*, 3(1):43–53. 17, 21, 57

Klein, C. and Briggs, R. (1980). Use of active compliance in the control of legged vehicles. *IEEE Trans SMC*, 10(7):393–400. 21

Korn, J. and of Technology, E. C. (1969). *Hydrostatic transmission systems*. Intertext Books, London. 26

Kurfess, T. R. (2004). *Robotics and Automation Handbook*. CRC Press. 89

Levine, W. (1996). *The Control Handbook*. The Electrical Engineering Handbook Series. CRC Press. 61

Liu, R. and Alleyne, A. (2000). Nonlinear force/pressure tracking of an electrohydraulic actuator. *Journal of Dynamic Systems, Measurement, and Control*, 122(1):232–236. 20

Luca, A. D., Albu-Schaffer, A., Haddadin, S., and Hirzinger, G. (2006). Collision detection and safe reaction with the dlr-iii lightweight manipulator arm. In *IEEE/RSJ International Conference on Intelligent Robots and Systems*, pages 1623 –1630. 21

REFERENCES

Mason, M. T. (1981). Compliance and force control for computer controlled manipulators. *IEEE Transactions on Systems, Man and Cybernetics*, 11(6):418 –432. 21

McGeer, T. (1990). Passive dynamic walking. *International Journal of Robotics Research*, 9(2):62–82. 15

Merritt, H. E. (1967). *Hydraulic control systems*. Wiley-Interscience. 24, 26, 29, 31, 35, 41, 42

Mistry, M., Buchli, J., and Schaal, S. (2010). Inverse dynamics control of floating base systems using orthogonal decomposition. *IEEE Int. Conference on Robotics and Automation (ICRA)*, pages 3406–3412. 17, 125

MOOG Inc. (2003). *Data Sheet of E024 Series Microvalve*. 24, 28, 124

Neal, T. (1974). Performance estimation for electrohydraulic control systems. In *Proceedings of the National Conference on Fluid Power*. Reprint in Moog technical bulletin #126. 60

Poulakakis, I., Smith, J. A., and Buehler, M. (2005). Modeling and experiments of untethered quadrupedal running with a bounding gait: The scout II robot. *International Journal of Robotics Research*, 24:239–256. 15

Pratt, G. and Williamson, M. (1995). Series elastic actuators. In *IEEE International Conference on Intelligent Robots and Systems (IROS)*. 18

Pratt, J., Chew, C., Torres, A., Dilworth, P., and Pratt, G. (2001). Virtual model control: An intuitive approach for bipedal locomotion. *The International Journal of Robotics Research*, 20(2):129–143. 17, 21, 81

Raibert, M. (1986). *Legged Robots that Balance*. MIT Press, Cambridge. 13, 84

Raibert, M., Blankespoor, K., Nelson, G., Playter, R., and the BigDog Team (2008). Bigdog, the rough-terrain quadruped robot. In *Proceedings of the 17th World Congress The International Federation of Automatic Control (IFAC)*. 13

Robinson, D. and Pratt, G. (2000). Force controllable hydro-elastic actuator. In *IEEE International Conference on Robotics and Automation (ICRA)*, volume 2, pages 1321 –1327 vol.2. 7

Schaal, S. (2006). The SL simulation and real-time control software package. Technical Report, (Online) Accessed March 2013 at *http://www-clmc.usc.edu/publications/S/schaal-TRSL.pdf*. 6

Sciavicco, L. and Siciliano, B. (2001). *Modelling And Control Of Robot Manipulators*. Springer. 58, 86, 107

Seering, W. P. (1987). Understanding bandwidth limitations in robot force control. In *IEEE Conference on Robotics and Automation (ICRA)*, pages 904–909. 21

Semini, C. (2010). *HyQ – Design and Development of a Hydraulically Actuated Quadruped Robot*. PhD thesis, Italian Institute of Technology and University of Genoa. 3, 5, 58, 61, 74, 76, 107

Semini, C., Buchli, J., Frigerio, M., Boaventura, T., Focchi, M., Guglielmino, E., Cannella, F., Tsagarakis, N. G., and Caldwell, D. G. (2011a). HyQ – a dynamic locomotion research platform. In *Int.l Workshop on Bio-Inspired Robots*. Nantes (France). 126

Semini, C., Khan, H., Frigerio, M., Boaventura, T., Focchi, M., Buchli, J., and Caldwell, D. G. (2012). Design and scaling of versatile quadruped robots. In *Int. Conf. on Climbing and Walking Robots (CLAWAR)*. 126

Semini, C., Tsagarakis, N. G., Guglielmino, E., Focchi, M., Cannella, F., and Caldwell, D. G. (2011b). Design of HyQ - a hydraulically and electrically actuated quadruped robot. *IMechE Part I: J. of Systems and Control Engineering*, 225(6):831–849. 5, 126

Sentis, L. and Khatib, O. (2006). A whole-body control framework for humanoids operating in human environments. In *IEEE International Conference on Robotics and Automation (ICRA)*, pages 2641 –2648. 85

REFERENCES

Sentis, L., Park, J., and Khatib, O. (2010). Compliant control of multi-contact and center of mass behaviors in humanoid robots. *IEEE Transactions on Robotics*, 26(3):483–501. 15

Seok, S., Wang, A., Otten, D., and Kim, S. (2012). Actuator design for high force proprioceptive control in fast legged locomotion. In *IEEE/RSJ International Conference on Intelligent Robots and Systems (IROS)*, pages 1970 –1975. 7

Sirouspour, M. and Salcudean, S. (2000). On the nonlinear control of hydraulic servo-systems. In *IEEE International Conference on Robotics and Automation (ICRA)*, volume 2, pages 1276 –1282 vol.2. 20

Skinner, S. and Long, R. (1998). *Closed Loop Electrohydraulic Systems Manual.* Vickers, Rochester Hills, MI, 2nd edition. 52

Slotine, J. and Li, W. (1991). *Applied Nonlinear Control.* Prentice Hall, New Jersey. 69, 80

Tanaka, T. and Hirose, S. (2008). Development of leg-wheel hybrid quadruped "airhopper" - design of powerful light-weight leg with wheel. In *IEEE/RSJ International Conference on Intelligent Robots and Systems (IROS)*, pages 3890–3895. 15

Thayer, W. (1958). Transfer functions for Moog servovalves – Moog technical bulletin #103. Technical report, Moog Inc. Controls Division, East Aurora, NY 14052. Rev. 1965. 60

Tsagarakis, N. G., Sardellitti, I., and Caldwell, D. G. (2011). A new variable stiffness actuator (compact-vsa): Design and modelling. In *IEEE/RSJ International Conference on Intelligent Robots and Systems (IROS)*, pages 378 –383. 18

Vanderborght, B. (2010). *Dynamic Stabilisation of the Biped Lucy Powered by Actuators with Controllable Stiffness.* Springer Tracts in Advanced Robotics. Springer. 123

Villani, L. and De Schutter, J. (2008). Force control. In Siciliano, B. and Khatib, O., editors, *Springer Handbook of Robotics*, pages 161–185. Springer Berlin Heidelberg. 17

Vukobratovic, M. and Borovac, B. (2004). Zero-moment point - thirty five years of its life. *International Journal of Humanoid Robotics*, 1(1):157–173. 15

Wang, W., Loh, R. N., and Gu, E. Y. (1998). Passive compliance versus active compliance in robot-based automated assembly systems. *Industrial Robot: An International Journal*, 25, Iss: 1:48–57. 58, 124

Weir, D., Colgate, J., and Peshkin, M. (2008). Measuring and increasing z-width with active electrical damping. In *Symposium on Haptic Interfaces for Virtual Environment and Teleoperator Systems*, pages 169 –175. 92

Westervelt, E., Grizzle, J., Chevallereau, C., and Choi, J. (2007). *Feedback Control of Dynamic Bipedal Robot Locomotion*. CRC Press. 15

Whitney, D. (1987). Historical perspective and state of the art in robot force control. *International Journal of Robotics Research*, 6(1):3–14. 16

Whitney, D. E. (1985). Historical perspective and state of the art in robot force control. In *IEEE International Conference on Robotics and Automation (ICRA)*, volume 2, pages 262 – 268. 16, 17, 18, 21, 57

Xuan Bo Tran, N. H. and Yanada., H. (2012). Modeling of dynamic friction behaviors of hydraulic cylinders. *Elsevier-Mechatronics*, 22:65–75. 38

Yang, Y., Semini, C., Guglielmino, E., Tsagarakis, N., and Caldwell, D. (2009). Water vs. oil hydraulic actuation for a robot leg. In *International Conference on Mechatronics and Automation (ICMA)*, pages 1940 –1946. 24

Yao, B., Bu, F., Reedy, J., and Chiu, G.-C. (2000). Adaptive robust motion control of single-rod hydraulic actuators: theory and experiments. *IEEE/ASME Transactions on Mechatronics*, 5(1):79 –91. 20

Zhang, Z. and Kimura, H. (2009). Rush: a simple and autonomous quadruped running robot. *Proc. IMechE , Part I: J. Systems and Control Engineering*, 223:323–336. 15

Zhao, J. (2003). *Development of EFT for Nonlinear SDOF Systems*. PhD thesis, University of Minnesota. 19

Declaration

I herewith declare that I have produced this thesis without the prohibited assistance of third parties and without making use of aids other than those specified; notions taken over directly or indirectly from other sources have been identified as such. This thesis has not previously been presented in identical or similar form to any other Italian or foreign examination board.

The thesis work was conducted from January 2010 to February 2013 under the supervision of Prof. Jonas Buchli, Dr. Claudio Semini, and Prof. Darwin G. Caldwell at the Istituto Italiano di Tecnologia.

Genoa, 20th of February 2013.